



Master Thesis

Master's degree in Energy and Nuclear Engineering

# **Glass-sealings for reversible solid oxide cells: Thermal, electrical and mechanical characterization**

**Candidate:**

Luigi Feline, 235044

**Supervisors:**

Prof. Federico Smeacetto

Prof. Massimo Santarelli

Prof. Monica Ferraris

# Contents

<b>Abstract</b> .....	2
<b>Introduction</b> .....	4
<b>1. Reversible solid oxide cells</b> .....	9
1.1. Main principles.....	9
1.2. Fundamental of electrochemistry applied to energy processes .....	16
1.3. Electrolyte materials .....	21
1.4. Fuel electrode materials.....	25
1.5. Air/oxygen electrode materials.....	28
1.6. Interconnector materials .....	30
1.7. Green Industrial Hydrogen .....	33
<b>2. Sealing technologies for solid oxide cells</b> .....	35
2.1. Metallic compressive seals .....	37
2.2. Mica-based compressive seals.....	38
2.3. Metallic brazes.....	41
2.4. Glass and glass-ceramic sealants .....	42
<b>3. Thermal characterization of glass-ceramic sealants</b> .....	59
3.1. Sr-based systems .....	62
3.2. Ba-based systems.....	67
<b>4. Electrical characterization of glass-ceramic sealants and post mortem analysis</b> .....	78
4.1. Sr-based systems .....	81
4.2. Ba-based systems.....	87
4.3. Summary of the results and discussions .....	100
<b>5. Mechanical tests on glass-ceramic sealants</b> .....	102
<b>Conclusions and future perspectives</b> .....	114
<b>Bibliography and reference</b> .....	116

## Abstract

An innovative approach in the field of energy production and storage is based on reversible Solid Oxide Cell (rSOC) technology. It represents a reliable, clean, versatile and efficient way to produce electric energy thanks to re-dox reactions between a fuel and an oxidant (Solid Oxide Fuel Cells mode, SOFC). On the other hand, it is possible to use this technology in electrolysis mode in order to produce fuels with high efficiency (i.e. H<sub>2</sub>, syngas) which can be stored. Due to the severe operating conditions required by rSOC technology the selection of the most suitable materials is crucial.

In rSOC stack the use of a sealant is needed in order to avoid gas mixing and consequent efficiency decreasing or device failure. The sealants must possess high gas tightness, thermo-chemical and thermo-mechanical compatibility with metallic and ceramic materials, as well as stability in the relevant operating conditions (850 °C, applied voltage and dual atmosphere) for thousands of hours.

Glass-ceramic materials represent the most suitable solution as sealants for rSOCs. The present work is focused on the design, production, characterization and testing of novel glass-ceramic systems. Six different parent glass compositions were considered, both BaO and SrO containing as main modifier oxides.

Most research on glass-based sealants has focused on partially crystallizing glasses from the system BaO-Al<sub>2</sub>O<sub>3</sub>-SiO<sub>2</sub>. These systems contain sanbornite (BaSi<sub>2</sub>O<sub>5</sub>) as main crystalline phase with a CTE compatible with both metallic and ceramic substrates. Anyway, barium content must be limited, in order to minimize the possibility of reaction with the Cr from the metallic interconnects, giving rise to BaCrO<sub>4</sub> (with a CTE of 22 · 10<sup>-6</sup> K<sup>-1</sup>). Glasses based on the SrO-Al<sub>2</sub>O<sub>3</sub>-SiO<sub>2</sub> system are also interesting, since the formation of SrSiO<sub>3</sub> with high CTE can be considered as a valid alternative to Ba-containing systems.

As produced glasses were characterized by Differential Thermal Analysis (DTA) and heating stage microscopy (HSM) in order to assess their sinter-crystallization behaviour and tailor the most suitable joining thermal treatment. The glass-ceramic sealants obtained from the joining process were studied by Dilatometry (DIL), X-Ray diffraction (XRD) and tested in contact with Crofer22APU as the metallic interconnect material. Joined samples Crofer22APU/sealant/Crofer22APU were produced and characterized by means of SEM and EDS. Furthermore, these sealants were tested simulating the real operating conditions, i.e. at 850 °C in dual atmosphere and with the application of 1.6 V for long periods (300-1000 hours). The electrical resistivity was monitored during the test. Post-mortem morphological and chemical analyses were carried out in order to investigate possible detrimental interaction between the glass-ceramics and Crofer22APU due to the severe environmental conditions of the test.

Two aluminoborosilicate CaO-containing compositions were initially designed and tested: HJ14 (Sr-containing) and HJ11 (Ba-containing). The parent glass compositions led to the formation of SrSiO<sub>3</sub> and BaSi<sub>2</sub>O<sub>5</sub> after the thermal treatments as main crystalline phases respectively in HJ14 and HJ11. CTE of the glass-ceramics lay in the range required for SOCs applications, thus allowing the systems to have an excellent compatibility with the Crofer22APU. Nevertheless, both the compositions showed a “refractory nature”

which may not be desired for these applications, especially when joined areas are subjected to thermal cycles. For a second series of systems, three new compositions were designed: GS7 (Sr-based), HJ26 (Ba-based) and HJ27 (Ba-based). The new compositions were obtained keeping the same  $\text{SiO}_2/\text{SrO}$  and  $\text{SiO}_2/\text{BaO}$  ratio of HJ14 and HJ11 respectively, adding  $\text{Al}_2\text{O}_3$  and  $\text{G}_2\text{O}_3$  to delay the crystallization process, thus obtaining a higher content of residual amorphous phase at the end of the thermal treatments. Nevertheless, the three systems failed the aging tests due to low CTE values. These results may be explained by the fact that CTE decreased and this was likely due to the formation of celsian phase, generated during the thermal treatments and in presence of the Al. The Ba-based systems were further developed with a fourth composition labelled as HJ28, designed with a new  $\text{SiO}_2/\text{BaO}$  ratio and partially substituting the  $\text{Al}_2\text{O}_3$  with  $\text{Y}_2\text{O}_3$ . HJ28 glass-ceramic showed a desired amount of amorphous nature. The most promising composition between the six analysed was the HJ11, which was consequently chosen to be subjected to torsion tests for the evaluation of the maximum shear strength. The torsion tests were performed at both room and high temperature on hourglass shaped samples joined with HJ11 glass-ceramic.

# Introduction

The world primary energy consumption is continuously growing in the years, as reported *Figure 1* and *Figure 2*: in 2016 a further increment of 1% has been estimated, however below the annual average of 1.8% forecast for the next 10 years [2]. The energy consumption trend is following the world economy growth (3.4% p.a. on average [3]), which is dominated by the contributions of the two main emerging economies: India and China.

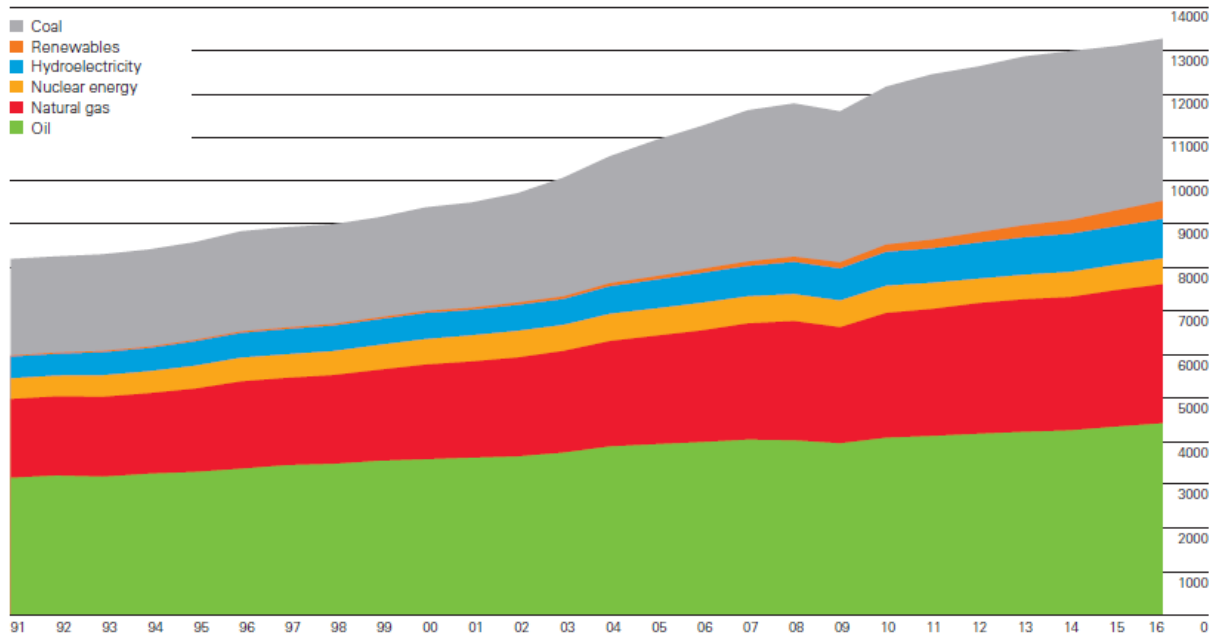


Figure 1: World primary energy consumption in million tonnes oil equivalent (vertical axis) [2].

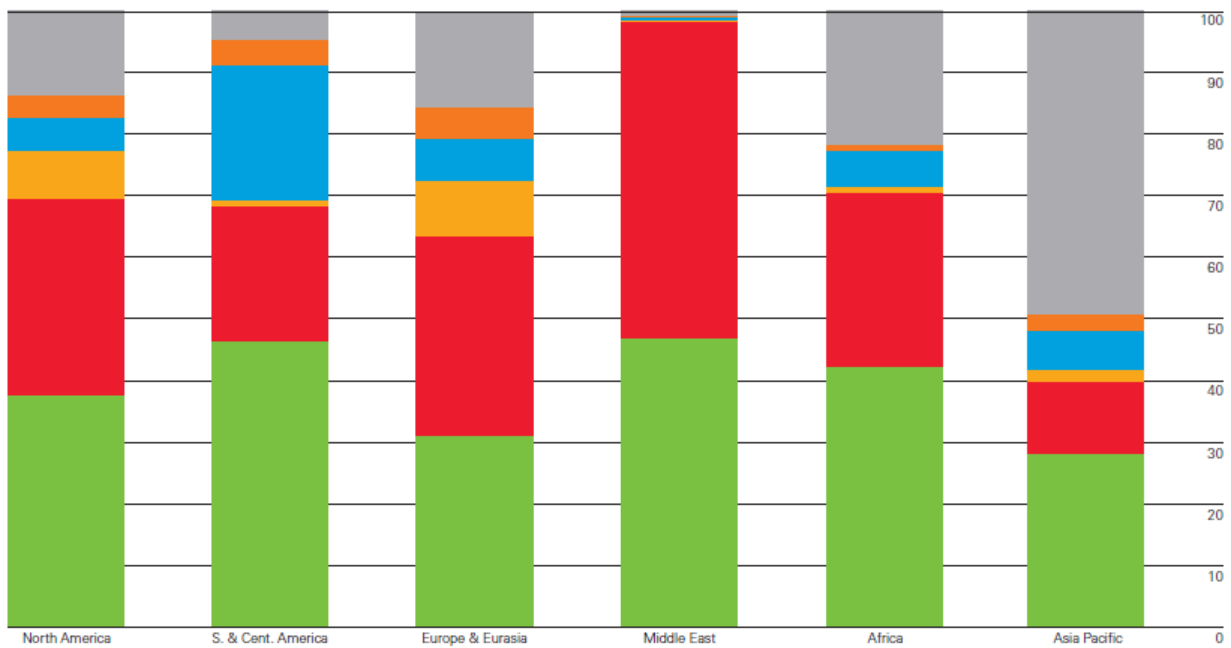


Figure 2: Regional primary energy consumption in 2016 in million tonnes oil equivalent (vertical axis) [2].

In the new century we are observing a gradual transition in the mix of primary energy sources. Oil shows the smallest rate of increment (0.7% p.a.), while coal, renewable sources and natural gas have promising growth trends. Renewable sources use is rapidly increasing (7.1 % p.a. [3]), and in the next future a coverage of the 10% of the total primary energy should be expected by these sources. Nowadays, oil, gas and coal are still the most used energy sources in the world, satisfying almost the 85% of the total primary energy demand.

Industry and power generation represent the highest demand of primary energy; the second one showed the highest increasing rate in energy demand (from 42% in 2015 to 47% in 2035 [3]), due to the increment in the need of electricity, as explained in *Figure 3*.

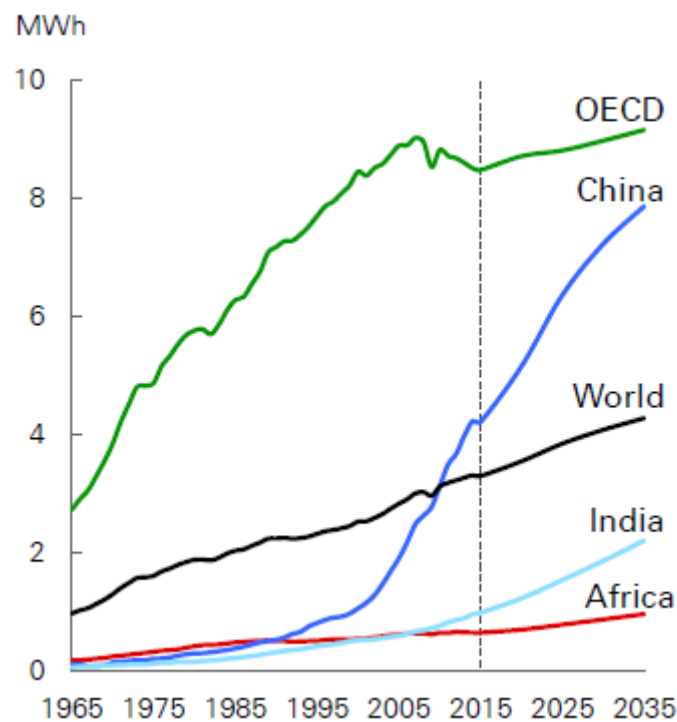


Figure 3: Electricity consumption per capita [3].

In the field of the power generation, the energy production plants fed by fossil fuels and biomass represent ones of the biggest air pollutants and greenhouse gases sources in the world.

The air pollution involved in the energy production is strictly related to the degree of economic development in a country. Europe is characterized by a great level of industrialization, which means a large use of fossil fuels in power plants and consequently high level of sulphur oxides emission as primary pollutants; on the other hand, less developed economies use mainly solid biomass as fuel, emitting mainly particulate matter.

The air pollutants are damaging substances produced by the combustion of fossil fuels and biomass, and they represent a hazard for the public health and for the environment. The most remarkable air pollutants are:

- Sulphur oxides (SO<sub>x</sub>), produced by the combustion of sulphur-containing fuels, such as many fossil fuels;
- Nitrogen oxides (NO<sub>x</sub>), produced by high-temperature combustion processes;
- Particulate matter (PM), solid/liquid organic and inorganic substances classified on the basis of their size: coarse particles (diameter between 2.5 and 10 μm) and fine particles (diameter smaller than 2.5 μm). The smaller the diameter is, the higher the health impact will be;
- Carbon monoxide (CO), a toxic gas produced by incomplete combustion processes;
- Volatile Organic Compounds (VOC), produced by the evaporation/sublimation of chemicals, fuels or solvents in the air;
- Ammonia (NH<sub>3</sub>), produced in agriculture and waste management activities;
- Ground-level ozone (O<sub>3</sub>), generated by the reaction between NO<sub>x</sub> and VOCs in the presence of sunlight;
- Heavy metals, such as lead and mercury;

The main pollutants emitted in the atmosphere from combustion processes involved in the energy production are SO<sub>2</sub>, NO<sub>x</sub> and PM.

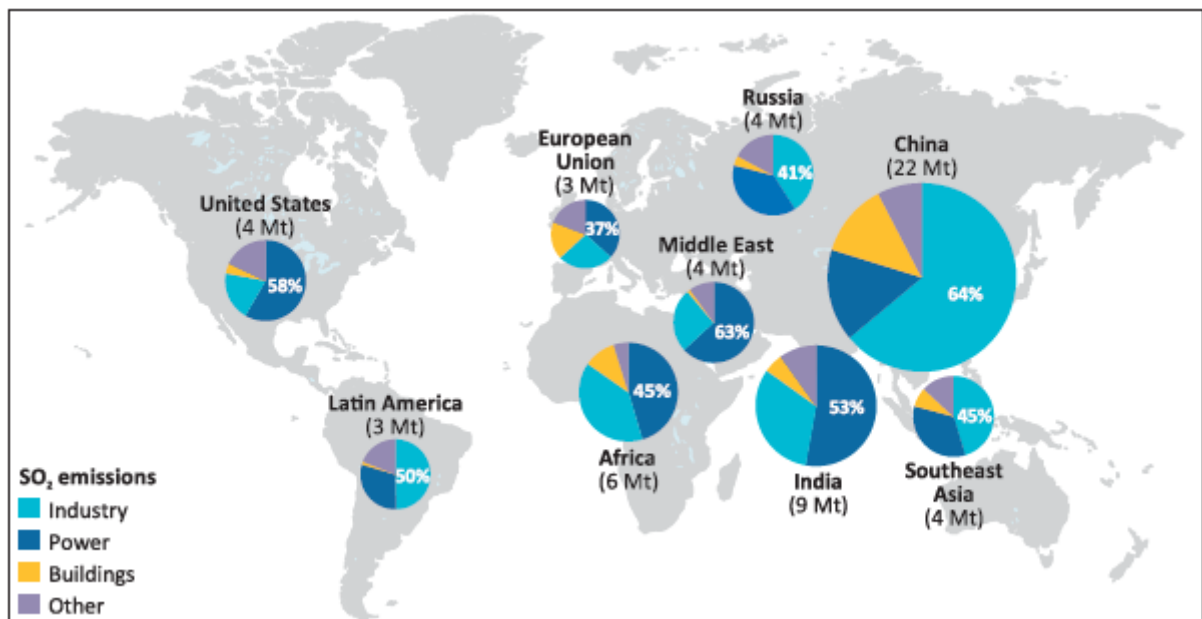


Figure 4: SO<sub>2</sub> emissions per region, 2015 [1].

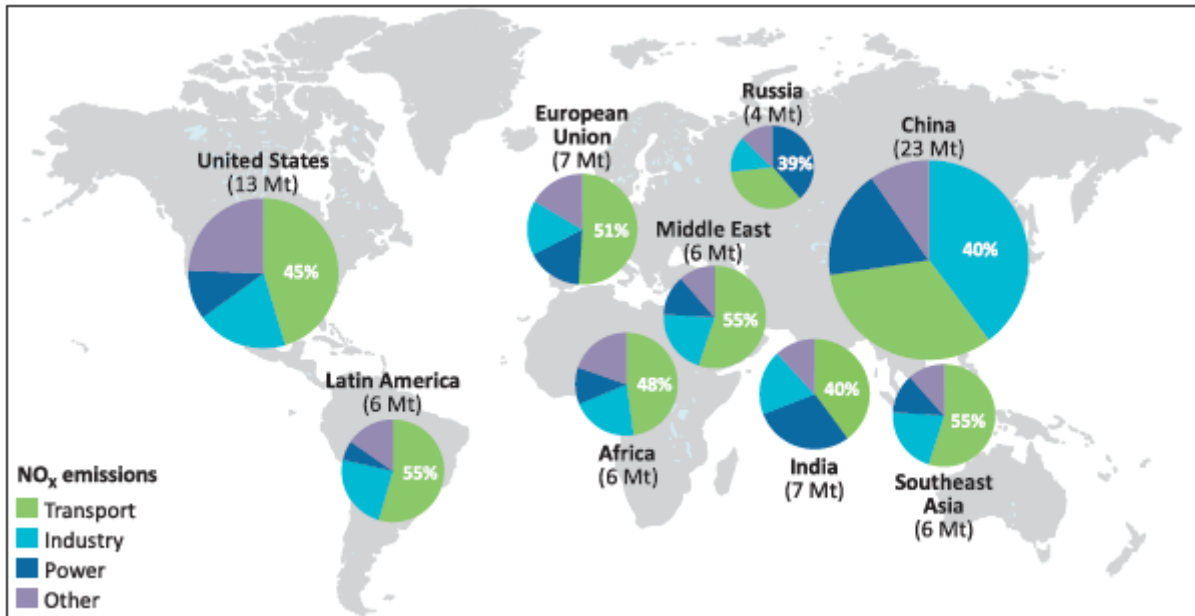


Figure 5: NO<sub>x</sub> emissions per region, 2015 [1].

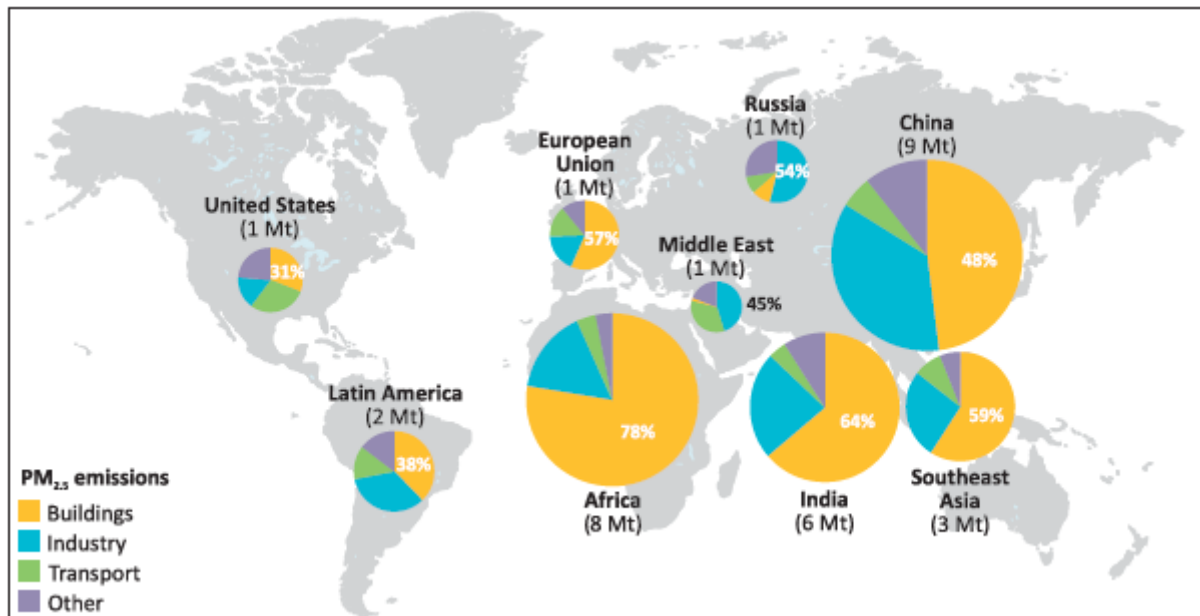


Figure 6: PM<sub>2.5</sub> emissions per region, 2015 [1].

It has been estimated [1] that 80 million tonnes of SO<sub>2</sub> were emitted in the 2015, mainly due to industries and power plants activities, with a considerable amount produced in China (Figure 4). In the same year, about 107 million tonnes of NO<sub>x</sub> [1] were emitted in the atmosphere, whose production was especially related to the transport sector (Figure 5). The last pollutant analysed for the 2015 was the PM<sub>2.5</sub>, emitted mainly in the residential sector (Figure 6).

After the industrial revolution, the concentration of the CO<sub>2</sub> in the air dramatically increased from 280 ppm in the pre-industrial era to over 400 ppm in the 2018 due to some human activities (i.e. fossil fuels combustion and deforestation). The consequence is the growth of the greenhouse effect which implies the progressive global warming and climate changes.

The energy sector is responsible for the 68% of the overall CO<sub>2</sub> emissions [4], due to a large use of fossil fuels for its energy needs. The highest global CO<sub>2</sub> emissions are due to the use of coal as energy source (45% in the 2015 [4]), which is the fuel with the highest carbon content. Nowadays, coal is the most used fuel in China, and this is the reason why this region is the one with the highest CO<sub>2</sub> emissions in the world (*Figure 7*).

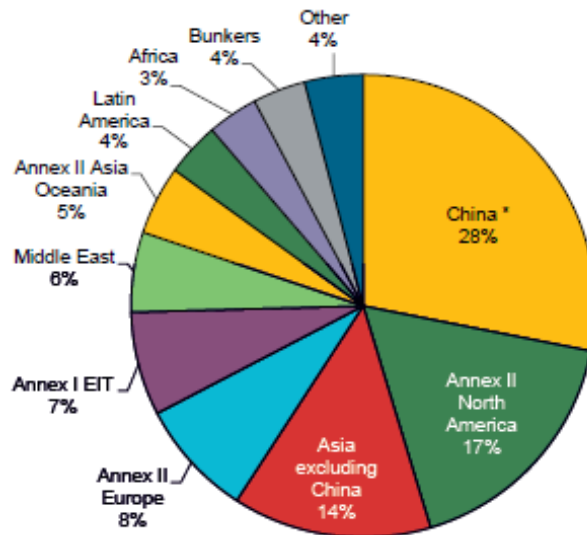


Figure 7: CO<sub>2</sub> percentage of emission per region, 2015[4].

In December 2015, 195 countries signed “The Paris Agreement”, aiming to reduce the greenhouse gases emissions in order to keep the global warming below 2 °C with respect to pre-industrial values.

In order to contrast air pollution and greenhouse effects related to the energy production, a new way to produce energy, based on a larger and more efficient utilization of clean sources and processes is needed. Fuel cells technology (treated in the next paragraphs) represents a promising approach to the problem. In this field, the selection of the most suitable materials and components is crucial.

# 1. Reversible solid oxide cells

## 1.1. Main principles

A reversible solid oxide cell is a high temperature electrochemical device able to work both as fuel cell and as an electrolyzer. The fuel cell mode (SOFC) is a promising solution in the field of the thermal and electric energy production, being able to directly convert chemical energy into electricity through a spontaneous redox reaction between a fuel and an oxidant. The absence of any intermediate energy conversions, which characterizes the most common energy production processes, makes this technology more efficient and with lower greenhouse gases and pollutants emissions (*Figure 1.1*). On the contrary, in the reverse configuration (SOEC) electricity is used to convert  $H_2O$ ,  $CO_2$  or both into  $O_2$  and  $H_2$  or syngas (a gaseous mixture of  $H_2$  and  $CO$ ) with efficiencies near the 100% in specific working conditions.

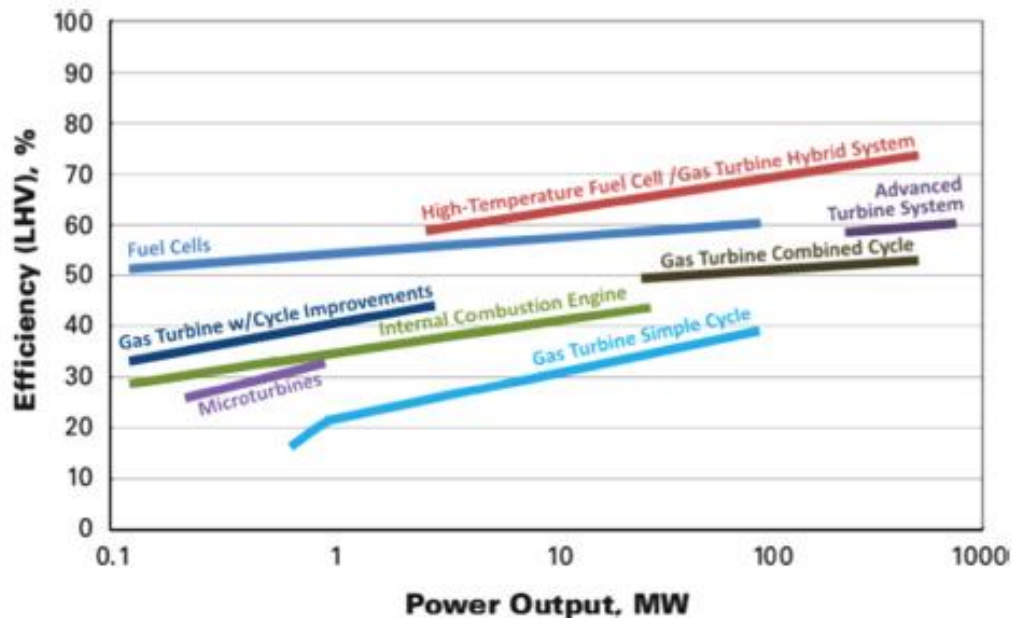


Figure 1.1: Efficiencies comparison between different energy conversion devices [5].

The solid oxide cells belong to the family of the medium-high temperature devices, with working temperatures ranging from  $500^{\circ}C$  up to  $1000^{\circ}C$ , depending on the applications and on the adopted materials. The high operating temperatures allow high reactions efficiency at the electrodes even without the utilization of precious catalysts; furthermore, the high temperatures promote a good ionic conduction through the electrolyte layer and a considerable fuel flexibility. Nevertheless, high operating temperatures require an accurate choice of the materials involved in the components and auxiliaries; moreover, they can lead to elevate thermo-mechanical stresses when the cell is subjected to several thermal cycles. All the main advantages and disadvantages of high operating temperatures devices are listed in *Table 1.1*. The main challenge for this technology is the identification of the best set of materials for all the stack components, which have to withstand to high thermo-mechanical stresses and, at the same time, ensure good performances.

Table 1.1: Advantages and disadvantages of high-temperatures SOFC/SOEC devices.

<i>Technology</i>	<i>Advantages</i>	<i>Disadvantages</i>
<i>High temperatures device</i>	<ul style="list-style-type: none"> <li>• Very good kinetic of the reactions</li> <li>• High ionic conductivity</li> <li>• Not precious catalysts involved</li> <li>• Fuel flexibility</li> <li>• Availability of heat at high temperature, so possibility to generate hybrid configuration</li> </ul>	<ul style="list-style-type: none"> <li>• Materials for cells and auxiliaries are usually expensive and complex due to the high working temperatures</li> <li>• Switch on very slow (5-6 hours)</li> <li>• Important thermal cycling impact</li> </ul>

A single reversible solid oxide cell (rSOC) is composed by:

- Fuel electrode (anode), where the fuel is oxidized (SOFC configuration) or reduced (SOEC configuration);
- Air/oxygen electrode (cathode), where the oxygen is reduced (SOFC configuration) or oxidized (SOEC configuration);
- Electrolyte, a thin dense layer between the electrodes able to conduct  $O^{2-}$  ions from the fuel electrode to the oxygen electrode (SOEC) or vice versa (SOFC), guarantying simultaneously the physical separation between the reactants;

The oxidation/ reduction reactions occurring at the electrodes in both the operating modes (SOFC/SOEC) are explained in *Figure 1.2* and *Table 1.2*.

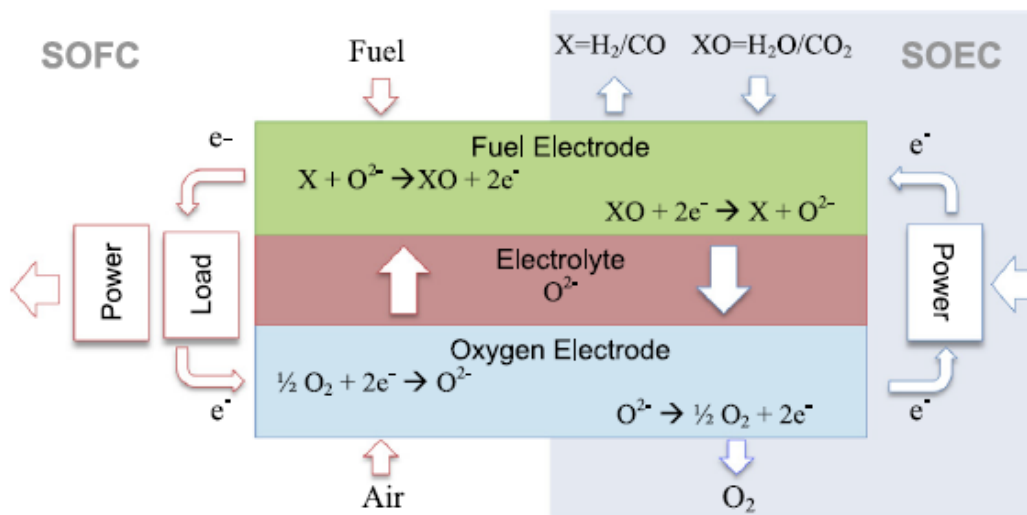


Figure 1.2: Schematic representation of the reactions and transport mechanisms involved in a rSOC unit during both SOFC and SOEC modes. [22]

Table 1.2: Reactions in SOFC/SOEC electrodes and global redox reaction for different fuels [22].

Electrode	SOFC	SOEC
Fuel electrode	$H_2 + O^{2-} \rightarrow H_2O$ $CO + O^{2-} \rightarrow CO_2 + 2e^-$	$H_2O + 2e^- \rightarrow H_2 + O^{2-}$ $CO_2 + 2e^{2-} \rightarrow CO + O^{2-}$
Air/oxygen electrode	$\frac{1}{2}O_2 \rightarrow O^{2-} + 2e^-$	$O^{2-} \rightarrow \frac{1}{2}O_2 + 2e^-$
Global redox reaction	$\frac{1}{2}O_2 + H_2 \rightarrow H_2O$ $\frac{1}{2}O_2 + CO \rightarrow CO_2$	$H_2O \rightarrow \frac{1}{2}O_2 + H_2$ $CO_2 \rightarrow \frac{1}{2}O_2 + CO$

The electrodes should possess the following characteristic:

- high porosity, to ensure the reactants diffusion inside;
- high ionic and electronic conductivity (MIEC, Mixed Ionic Electronic Conductivity);
- high reactivity, namely both specific reaction surface and catalytic activity, to allow the reactions to occur.

On the other hand, the electrolyte should be:

- as much dense as possible, to avoid mixing of reactants;
- electronic insulator, to avoid short circuit and current shunting;
- ionic conductor, to ensure the chemical link between the reactants.

A single fuel cell can produce a voltage of 0.7 V [6]. To increase the overall voltage, several cells need to be connected in series in the so-called *stack configuration*, such as in *Figure 1.3*. In this structure, between the electrodes of two series-connected cells, a metallic component known as interconnect or bipolar plate is placed, in order to ensure the electronic connection between two adjacent cells and the physical separation between the reactants. Often, the interconnects are designed with channels on the surface, thus allowing an optimal distribution and flow of gasses.

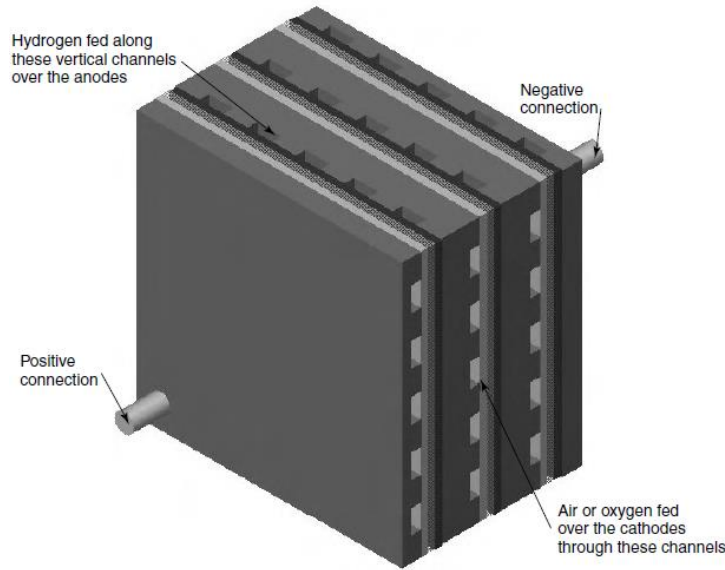


Figure 1.3: Scheme of a stack made of three series-connected cells. Between two cells it's possible to identify the interconnects; the overall structure is closed between two end plates for the connection with the external circuit [6].

The amount of cathodic air needed in the cell depends on the fuel employed, and it is always slightly larger than the stoichiometric one; the ratio of the stoichiometric air ( $G_{air,s}$ ) to the air actually introduced in the cell ( $G_{air}$ ) is called *air utilization (AU)* [5]:

$$AU = \frac{G_{air,s}}{G_{air}} \quad \text{Eq.1.1}$$

The air in excess is generally used to cool-down the system. When the cell is fed by pure hydrogen, considerable amount of air is needed (AU lower than 0.2), because the exciting air is the only mean for controlling the temperature; on the contrary, the methane-fed cells are autothermal systems where the cooling is ensured mainly by the steam reforming reaction. In this case lower value of excess air is introduced (AU higher than 0.15) [5]. In these last family of cells, the methane can be directly oxidized at the anode in the SOFC configuration, following the overall reaction [6]:



The overall reaction (Eq. 1.2) however is the result of the oxidation of hydrogen (Figure 1.4) and of carbon monoxide [6]:



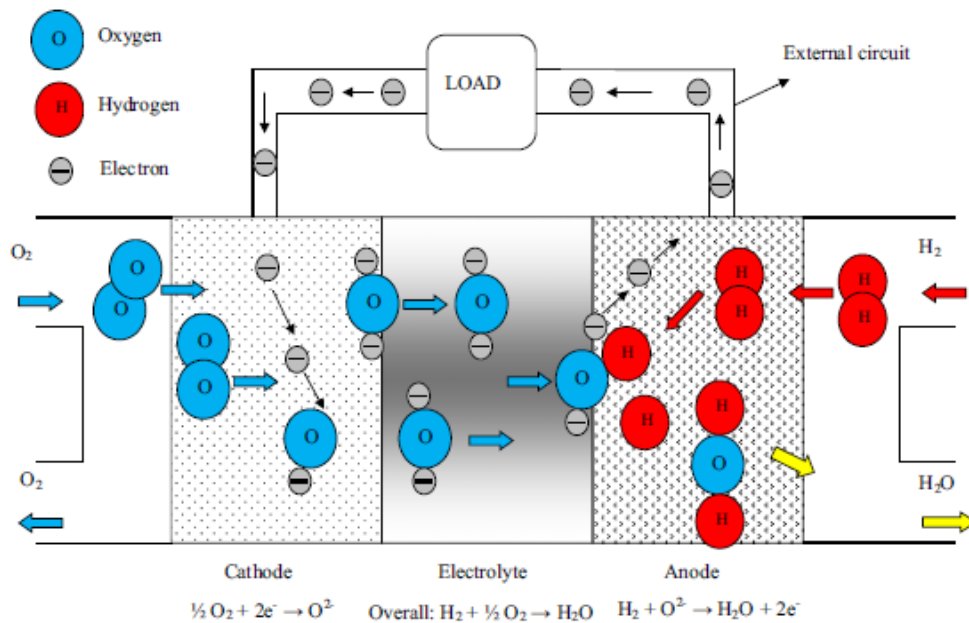


Figure 1.4: schematic representation of a SOFC structure and operating principle [9]

$H_2$  and  $CO$  from *Eq. 1.3.1* and *Eq. 1.3.2* are the products of the methane steam reforming, an endothermic reaction occurring completely at the anode or partly at the anode and partly into an external reformer [5]:



The thermal energy needed for the steam reforming reaction is directly provided by the cell, which is an exothermic system; this smart solution allows the autothermal control of the whole system. When an external reformer is installed (*Figure 1.5*), the heat needed can be provided by the hot gases coming from the anode outlet, or by a burner fed by the exhausts of both the electrodes ( $CH_4$ ,  $CO$ ,  $H_2$ ,  $O_2$ ). Steam represents one of the main products of a cell (together with slight amount of  $CH_4$ ,  $H_2$  and remaining  $CO$ ), and it can be recirculated inside the system for new reforming and oxidation reactions [8].

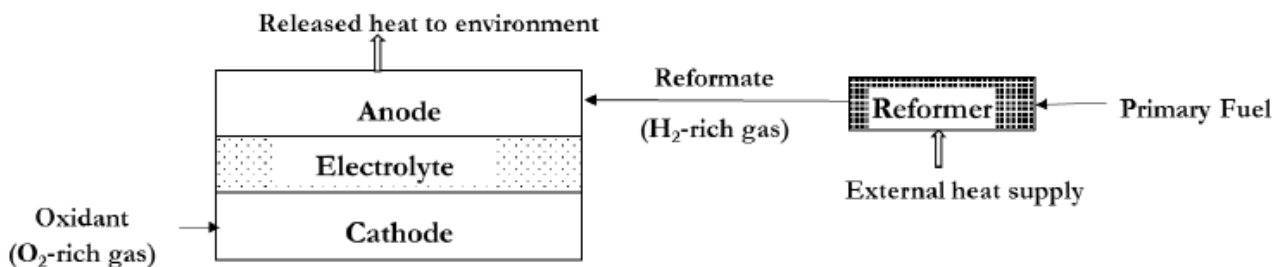


Figure 1.5: SOFC with an external reforming [8]

The main problem related to the use of methane (or other hydrocarbons) is represented by the carbon deposition, a degradation phenomenon which can lead to the failure of the entire system. The carbon is produced by a cracking reaction, described as follows in the case of methane [9]:



This reaction in *Eq. 1.5* can occur at high temperatures and it is enhanced by the presence of Nickel, which in general is present in the anode material. The produced carbon can deposit on the electrodes, obstructing their pores and thus hindering the diffusion of the reactants molecules. The  $O^{2-}$  ions reaching the TPB are not able to oxidize new fuel molecules, so they re-oxidize the Nickel in the anode structure leading to the production of NiO. The consequence is a strong volume increment which causes high mechanical stresses between the anode and the electrolyte, leading to possible cell failure.

A common way to classify the rSOCs is based on to the element of the cell that acts as support, as summarized in *Figure 1.6*:

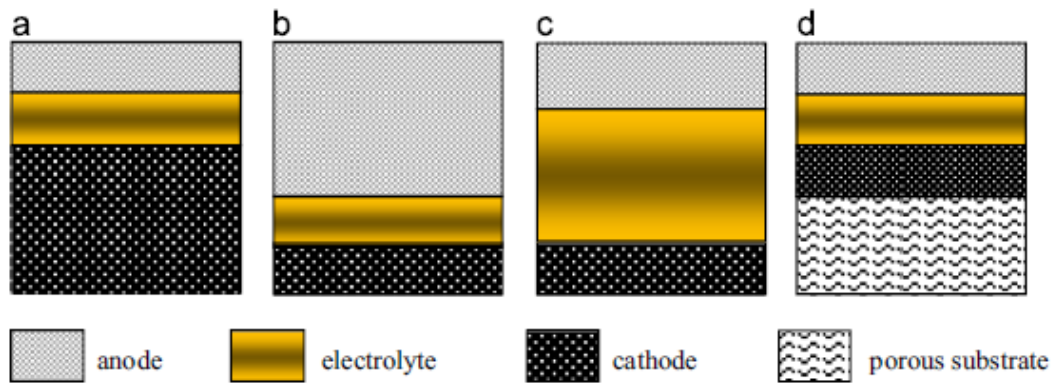


Figure 1.6: rSOC configurations: cathode supported (a), anode supported (b), electrolyte supported (c) and porous substrate (d) [9].

The electrode supported cells (*Figure 1.6 a* and *b*) ensure the best performances thanks to the reduced thickness of the electrolyte, which represents the resistive layer of the system. On the contrary, the electrolyte supported cells (*Figure 1.6 c*) have superior mechanical resistance. The last solution is the most complex configuration, with the cell entirely supported by a porous substrate (*Figure 1.6 d*) which could be the metallic interconnect of the stack [9].

A second way to group the cells is following their geometry. Nowadays two main configurations are available: tubular cell and planar cell, as shown in *Figure 1.7*.

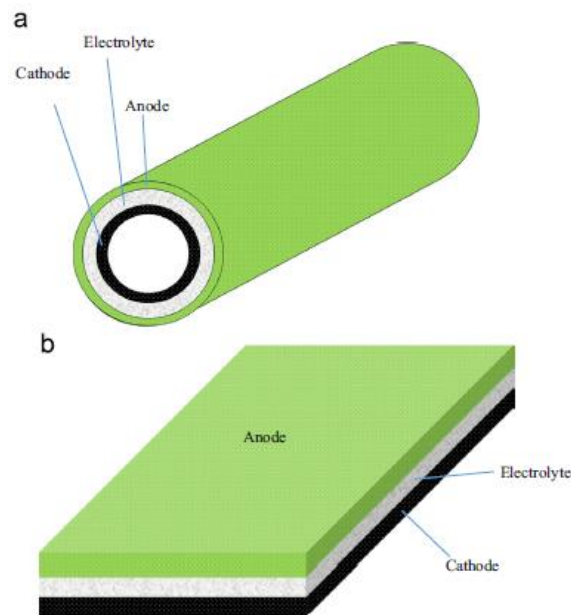


Figure 1.7: rSOC possible geometries: tubular cell (a) and planar cell (b) [9].

The planar cell (*Figure 1.7, b*) is easier to produce with respect to the tubular one (*Figure 1.7, a*), and it's characterized also by higher power density [9].

Nowadays, the most promising configuration is the planar anode supported cell. The research is focusing about best materials to be used as anode, cathode, electrolyte and interconnect according to their functions and characteristics, reported in *Figure 1.8* [10].

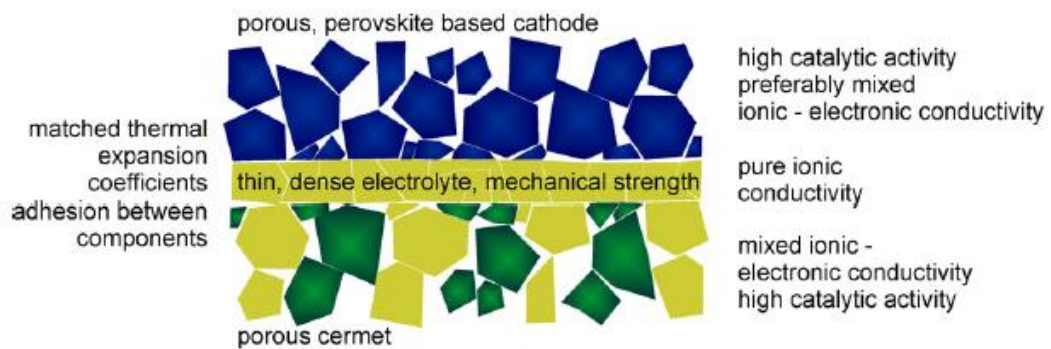


Figure 1.8: rSOC main components, micro structure and functions [10]

## 1.2. Fundamentals of electrochemistry applied to energy processes

The spontaneous redox reaction occurring inside a fuel cell is characterized by a variation of the Gibbs free energy lower than zero [6]:

$$\Delta\bar{g} = \bar{g}_{products} - \bar{g}_{reactants} < 0 \rightarrow W_{el} > 0 \quad \text{Eq. 1.6}$$

A reduction of the Gibbs free energy for a generic reaction (*Eq. 1.6*) means that energy is delivered; for a fuel cell in the specific, the redox reaction converts the chemical energy of the reactants in electric power, defined as [6]:

$$W_{el} = I \cdot V \quad [W] \quad \text{Eq. 1.7}$$

where  $I$  [A] is the current and  $V$  [V] is the voltage.

The current ( $I$ ) can be evaluated starting from the *Faraday's Law* [6]:

$$\dot{n}_i = \frac{I}{z_i \cdot F} \rightarrow I = \dot{n}_i \cdot z_i \cdot F \quad [A] \quad \text{Eq. 1.8}$$

- $\dot{n}_i$ : molar flow rate of the chemical species  $i$  [mol/s];
- $z_i$ : charge number of the chemical species  $i$ , defined as the number of electrons exchanged by the species in the reaction;
- $F$ : Faraday's constant, equals to 96487 [C/mol];

The charge number depends on the chemical species involved; referring to the most common species used as reactants for SOFCs, it is equal to 1 for the hydrogen, 2 for the oxygen and  $4x+y-2z$  for a generic hydrocarbon in the form  $C_xH_yO_z$  [6].

In the ideal condition of open circuit, namely when the external circuit is opened and there are not any losses in the device, it is possible to define the *Open Circuit Voltage* (OCV) as the voltage gradient occurring in the cell due to the separation of the charge in reversible conditions of equilibrium [6]:

$$OCV = -\frac{\Delta\bar{g}}{z_R \cdot F} \quad [V] \quad \text{Eq. 1.9}$$

- $\Delta\bar{g} = \bar{g}_{products} - \bar{g}_{reactants}$ : Gibbs free energy variation of the reaction [kJ/mol], given at a certain value of T and P (thermodynamic state of the system);
- $F$ : Faraday's constant;
- $z_R$ : charge number of the fuel;

The OCV is a function of the thermodynamic state (P, T) of the system. To underline this dependence, *Eq. 1.9* can be arranged in the following form under the hypothesis of ideal gas [6]:

$$OCV = -\frac{\Delta\bar{g}_0(T, P_0)}{z_R \cdot F} + \frac{R \cdot T}{z_R \cdot F} \cdot \ln \frac{\prod_i^R \left(\frac{P_i}{P_0}\right)^{\nu_i}}{\prod_i^P \left(\frac{P_i}{P_0}\right)^{\nu_i}} \quad \text{Eq. 1.10}$$

For a cell fed by Hydrogen operating at 200 °C, the OCV is about 1.14 V [6].

The *Nerst law* (*Eq. 1.10*) provides the theoretical value of the OCV. When the circuit is closed, the current starts to flow inside, and the voltage measured decreases because the cell is no longer in reversible conditions of equilibrium.

The voltage drops of the *polarization curve* summarized in *Figure 1.9* are caused by the transport phenomena, which depend on the thermophysical properties of the system. Four main transport phenomena are involved, each predominant in each area of the curve:

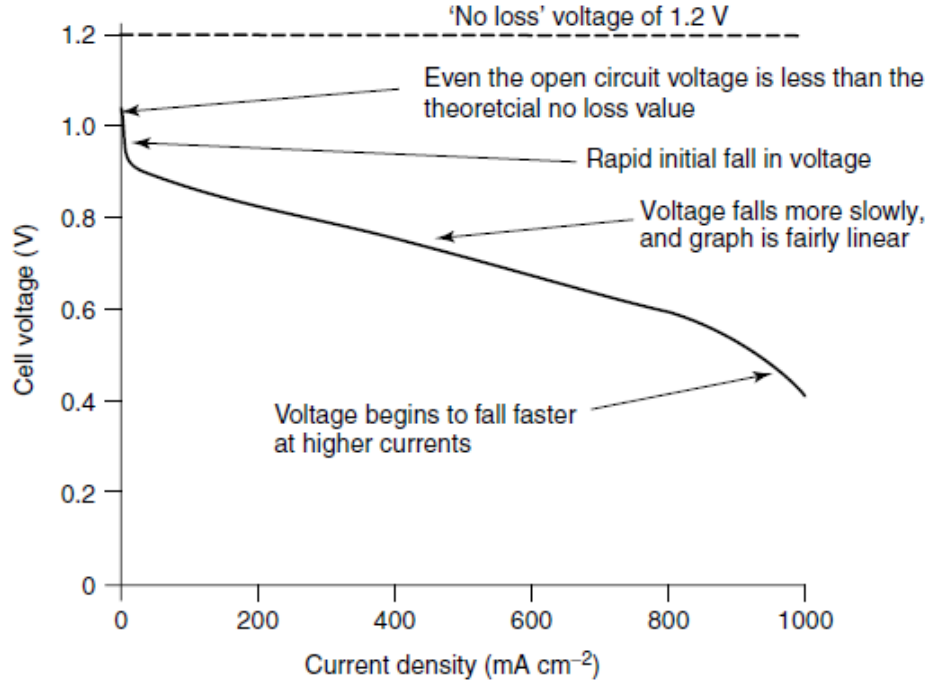


Figure 1.9: Polarization curve of a cell fed by hydrogen below 100 °C [6].

- *Crossover*: a very slight molecular diffusion of reactants from the electrodes through the electrolyte (especially in case of not completely densified electrolyte) [6]. The consequence is a reduction of the reactants concentration at the electrodes, with a small deviation of the real OCV from the theoretical one provided by the *Nerst Law* (Eq. 1.9 and Eq. 1.10);
- Charge transfer from the electrode to the electrolyte and vice-versa, related to the kinetic behaviour of the reactions occurring at the electrodes. The associated drop of voltage is called *activation overvoltage* (Eq. 1.11), and represents the amount of OCV spent to overcome the activation energy of the reactions [6]:

$$\eta_{act} = \frac{R \cdot T}{\beta \cdot n_{RDS} \cdot F} \sinh^{-1} \left( \frac{i}{2i_0} \right) \quad [V] \quad \text{Eq.1.11}$$

where  $\beta$  is the symmetry factor,  $n_{RDS}$  is the number of electrons exchanged in the rate determine step of the complete mechanism (namely the slowest step) and  $i_0$  is the current density in the ideal condition of equilibrium. To reduce the activation overvoltage, it is necessary to use efficient catalysts or to increase the operating temperature, partial pressure or reactants concentration;

- Charge migration or conduction, approximated to a region having linear behaviour in the polarization curve. The associated drop of voltage is called *ohmic overvoltage* (Eq. 1.12), and it can be approximated as the amount of OCV used to drive the ions migration through the electrolyte, which is the thickest layer of the cell [6]:

$$\eta_{ohm} = \rho_{ely} \cdot L_{ely} \cdot i \quad [V] \quad \text{Eq.1.12}$$

where  $\rho_{ely}$  is the electrolyte resistivity [ $\Omega/m$ ] and  $L_{ely}$  is the electrolyte thickness [m]. The ohmic overvoltage is directly proportional to the electrolyte resistivity and thickness, so it can be reduced using materials with high ionic conductivity or reducing as much as possible the electrolyte thickness;

- Mass transfer, related to the diffusion of reactants through the electrodes pores until the electrolyte interface, where the catalyst for the reaction is located. This process is slower than the charge transfer, especially at high current values, so it is a limiting mechanism. Molecules not reacted yet are not fast enough to continuously substitute those already reacted. The consequent limited concentration of reactants in the point of reaction leads to a drop of the voltage (*mass transport or concentration losses*, Eq. 1.13) according to the *Nerst law* (Eq. 1.9 and Eq. 1.10) [6]:

$$\eta_{dif} = \left| \frac{R \cdot T}{z \cdot F} \ln \left( 1 - \frac{i}{i_L} \right) \right| \quad [V] \quad \text{Eq.1.13}$$

The quantity  $i_L$  is the limiting current density of the electrode [ $A/m^2$ ], defined as [6]:

$$i_L = z_i \cdot F \cdot D^{eff} \cdot \frac{C_{i,b}}{\delta} \quad \left[ \frac{A}{m^2} \right] \quad \text{Eq. 1.14}$$

where  $C_{i,b}$  is the concentration of the chemical species  $i$  at the bulk,  $D^{eff}$  is the effective coefficient of diffusion, function of the porosity and tortuosity of the electrode, and  $\delta$  is the electrode thickness.

Considering all the irreversible processes caused by the transport phenomena, the voltage of the cell during the operational phase can be expressed as a function of the current density, obtaining the polarization curve of a cell (*Figure 1.9*) [6]:

$$V_c(I) = OCV - (\eta_{act} + \eta_{ohm} + \eta_{dif}) \quad [V] \quad \text{Eq. 1.15}$$

As said before, a single cell produces a voltage value which is not suitable for practical application. In a stack, where the cells are connected in series, the overall output power is increased, depending on the number of series-connected cells ( $n_c$ ) [5]:

$$W_{el} = V_c \cdot I \cdot n_c \quad [W] \quad \text{Eq. 1.16}$$

The efficiency (*Eq. 1.17*) is defined as the gain ( $W_{el}$ ) over the expenditure (chemical energy content of the fuel) and it's direct proportional to the voltage of a single cell [6]:

$$\eta = \frac{W_{el}}{G_f \cdot LHV_f} = const \cdot V_c \quad \text{Eq. 1.17}$$

where  $LHV_f$  is the low heating value of the fuel [kJ/kg] and  $G_f$  is the fuel flow rate, obtained by the Farady's law expressed in the *Eq. 1.8* [6]:

$$G_f = \frac{I \cdot n_c \cdot \bar{M}_f \cdot \lambda_f}{z_f \cdot F} \quad \left[ \frac{kg}{s} \right] \quad \text{Eq. 1.18}$$

with  $\bar{M}_f$  molecular weight of the fuel [kg/kmol] and  $\lambda_f$  fuel utilization coefficient, defined as the ratio of the mass of fuel reacted in the cell to the total mass of fuel entering the cell.

The last important quantity that can be evaluated for a fuel cell is the heat flux generated during the operational phase and released to the external environment (*Eq. 1.21*); it is a function of two terms: the reaction heat (*Eq. 1.19*), related to the molar entropy variation of the reaction ( $\Delta \bar{s}$ , smaller than zero) and the irreversibility heat (*Eq. 1.20*), related to the transport phenomena [5]:

$$\phi = \phi_{REACTION} + \phi_{IRREVERSIBILITY}$$

$$\phi_{REACTION} = -\frac{\Delta \bar{s} \cdot T}{z_f \cdot F} \cdot I \quad [W] \quad \text{Eq. 1.19}$$

$$\phi_{IRREVERSIBILITY} = (\eta_{act} + \eta_{ohm} + \eta_{dif}) \cdot I \quad [W] \quad \text{Eq. 1.20}$$

$$\phi = I \cdot \left( -\frac{\Delta \bar{h}}{z_f \cdot F} - V_c \right) \quad [W] \quad \text{Eq. 1.21}$$

In the electrolytic configuration a non-spontaneous redox reaction occurs, so an energy consumption is required [22]:

$$\Delta \bar{g} = \bar{g}_{products} - \bar{g}_{reactants} > 0 \rightarrow W_{el} < 0 \quad \text{Eq. 1.22}$$

The main parameters for an electrolytic cell are evaluated with the equations already described for a fuel cell in the previous lines; the most important difference is the definition of the voltage as a function of the current density (*Eq. 1.23*) [7] and the respectively polarization curve (*Figure 1.10*):

$$V_c(i) = OCV - (\eta_{act} + \eta_{ohm} + \eta_{dif}) \quad [V] \quad \text{Eq. 1.23}$$

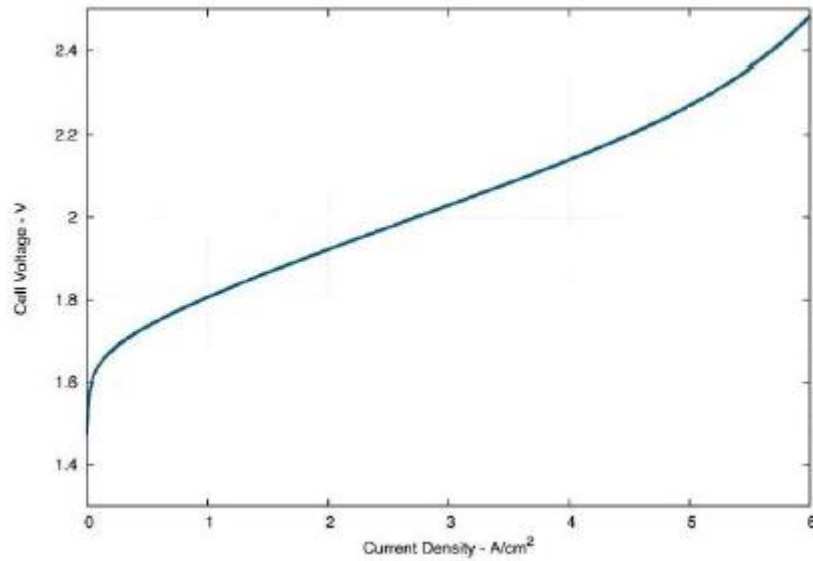


Figure 1.10: Polarization curve for an electrolytic cell [7].

During the operational phase, the transport phenomena causes an increment in the voltage absorbed by the cell, obtaining an opposite behaviour with respect to the fuel cells.

In a SOEC the gain is the production of what was referred to as fuel in the SOFC mode, as a consequence of energy consumption [22]:

$$\eta = \frac{G_f \cdot LHV_f}{W_{el}} \quad \text{Eq. 1.24}$$

In reverse condition, the reaction heat is absorbed from the external environment (negative contribution), being the molar entropy variation of the reaction a positive quantity; on the contrary, the heat generated from the irreversibilities is still a positive contribution, such as in the fuel cell configuration, so it's delivered to the external environment. So, the overall heat exchanged with the external environment in the electrolytic configuration is equal to [22]:

$$\phi = I \cdot \left( \frac{\Delta \bar{h}}{z_f \cdot F} - Vc \right) \quad [W] \quad \text{Eq. 1.25}$$

and it can be absorbed (endothermic configuration,  $\frac{\Delta \bar{h}}{z_f \cdot F} > Vc$ ) or leaved (exothermic configuration,  $\frac{\Delta \bar{h}}{z_f \cdot F} < Vc$ ). When the overall heat is exactly equals to zero, the cell is working in adiabatic condition; this interesting situation is the so-called *thermoneutral point* and represents the best working condition for an electrolytic cell, during which an efficiency of 100% is reached. The respectively voltage value generated in these conditions is defined as [22]:

$$V_c = \frac{\Delta \bar{h}}{z_f \cdot F} \quad [V] \quad \text{Eq. 1.26}$$

### 1.3. Electrolyte materials

The electrolyte is a dense layer that has to ensure the physical separation between the reactants, avoiding their diffusion and mixing; at the same times, it should have a high ionic conductivity at high temperatures (0.1 S/cm [12]). On the other hand, the electronic conductivity of the electrolyte material should be as low as possible, otherwise the electrons would be subtracted from the external circuit, resulting in a current shunting. The electrolyte is placed in between the anode and the cathode, so its chemical stability at high temperature in dual atmosphere (both oxidizing and reducing) is crucial together with a good adhesion with the electrodes. As last requirement, the mismatch between the coefficient of thermal expansion (CTE) of the electrolytic material and that of the components with which it is in contact should be minimized, in order to avoid possible thermo-mechanical stresses in the system.

In the solid ceramic oxide electrolyte, adopted for SOEC/SOFC, the  $O^{2-}$  ions are conducted by means of ion hopping mechanism through the oxygen vacancies in the structure, which is a thermally activated process. Nowadays, the electrolytes available can be distinguished in two families, according to their structure (*Figure 1.11*) [11]:

- Fluorite structure (*Figure 1.11 a*): in which cations are organized in a cubic face-centred structure and anions occupy the tetrahedral sites.
- perovskite structure materials (*Figure 1.11 b*): expressed by the generic formula  $ABO_3$ , where A represents the vertices of the cube, B the centre of the cubic structure (octahedral) and O the centre of each face of the cube;

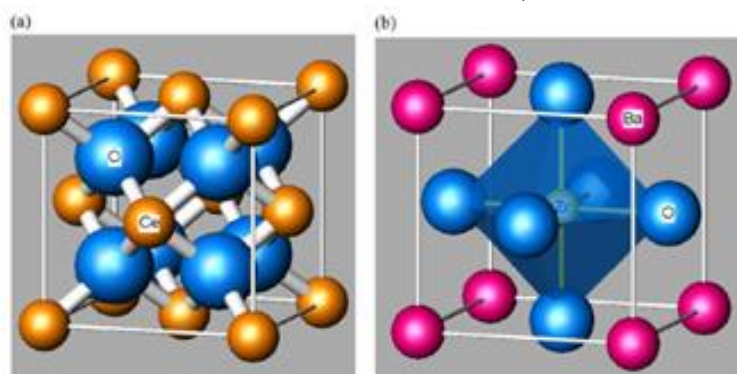


Figure 1.11: Cubic fluorite structure (a) and perovskite structure (b) [11].

The first electrolyte material adopted and still the most common is YSZ (Yttria-stabilized Zirconia), in which the cubic form of the zirconia is fully stabilized by the addition of Yttria (2-10 %mol [12]). Pure  $ZrO_2$  shows polymorphism: it has a monoclinic structure at room temperature, which transforms into tetragonal over  $1170^\circ\text{C}$  and into cubic fluorite over  $2370^\circ\text{C}$  [10]. The doping with  $Y_2O_3$  allows the cubic fluorite structure stabilization up to the room temperature and, moreover, introduces oxygen vacancies in the structure [10]. This compound ensures an optimal chemical resistance in dual atmosphere and suitable mechanical properties, especially useful in the electrolyte supported cells. However, the ionic conductivity is acceptable only for working temperatures higher than  $600\text{-}700^\circ\text{C}$ . Instead of Yttria, the doping can be also performed using  $Sc^{3+}$  or  $Ca^{2+}$  ions. Of great interest is the  $Sc_2O_3\text{-}ZrO_2$  (ScSZ), whose ionic conductivity value at  $800^\circ\text{C}$  is 0.15 S/cm, similar to the ionic conductivity of the 8YSZ at  $1000^\circ\text{C}$  [10].

An alternative solution to zirconia-based electrolytes are the CeO<sub>2</sub>-based (i.e. gadolinia doped ceria GDC or samaria doped ceria SDC [12]), which have a stable fluorite structure at room temperature (*Figure 1.12*). The doping, performing mainly through Y<sub>2</sub>O<sub>3</sub> molecules, is still needed to introduce oxygen vacancies in the structure. The main issue related to the use of CeO<sub>2</sub>-based electrolytes is represented by the increment of the electronic conductivity in the reducing atmosphere. A possible solution may be the deposition of protective coating, e.g. BaCe<sub>1-x</sub>Sm<sub>x</sub>O<sub>3-δ</sub>, or by introducing in the CeO<sub>2</sub> structure different dopants [22].

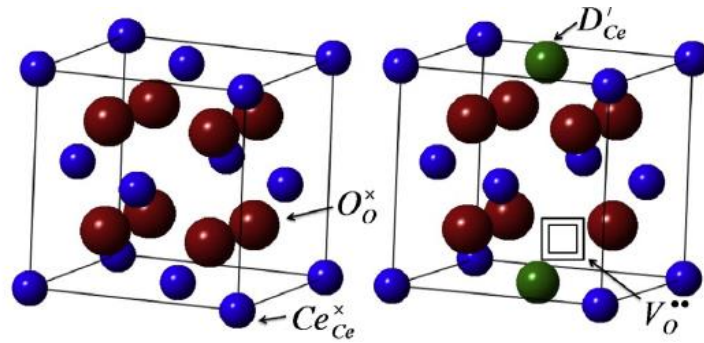


Figure 1.12: Cubic fluorite structure of ceria (left) and oxygen vacancy in the doped ceria system (right) [12].

Among the fluorite-like electrolytes, the  $\delta$  phase of the Bi<sub>2</sub>O<sub>3</sub> may represent the best solution in terms of ionic conductivity, as shown in *Figure 1.13*. Unfortunately, this phase is stable only in a very narrow temperature range (729-825 °C), and the pure form undergoes to reduction in presence of non-oxygen atmospheres [10].

Some electrolyte materials investigated have a superstructure of fluorite structure named pyrochlore, in the general form A<sub>2</sub><sup>3+</sup>B<sub>2</sub><sup>4+</sup>O<sub>7</sub>, where the cations A and B are ordered and one eighth of the anions are absent, to create the oxygen vacancies. The most common pyrochlore used as possible electrolyte is the Gd<sub>2</sub>Zr<sub>2</sub>O<sub>7</sub>, obtaining partially or totally substituting the Ti in Gd<sub>2</sub>Ti<sub>2</sub>O<sub>7</sub> with Zr [12].

The LaGaO<sub>3</sub> (LG) is used as electrolyte with a perovskite structure, ensuring ionic conductivity considerable higher than the YSZ, especially after the doping. The most promising doped form is the LSGM (La<sub>0.9</sub>Sr<sub>0.1</sub>Ga<sub>0.8</sub>Mg<sub>0.2</sub>O<sub>3</sub>). However, it demonstrated an insufficient chemical stability at high temperature in dual atmosphere, which leads to the formation of nickel-LaNiO<sub>3</sub> at the anode interface and to the decomposition of the LaGaO<sub>3</sub> into the volatile Ga<sub>2</sub>O<sub>3</sub> in the reducing atmosphere [10].

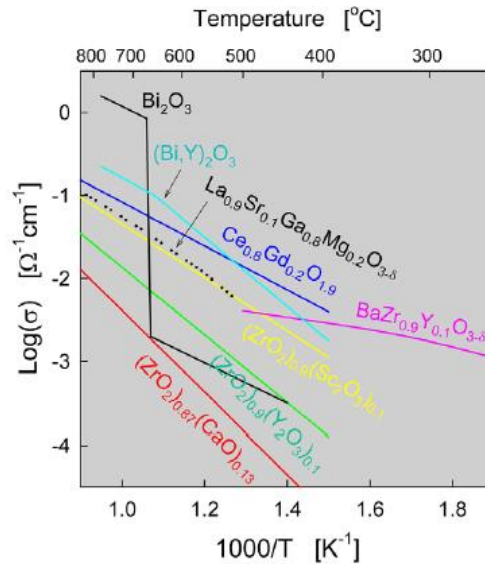


Figure 1.13: Ionic conductivity of some oxide electrolytes as a function of the temperature [11]

Table 1.3.1 and table 1.3.2 summarize the state of art in the materials for electrolytes.

Table 1.3.1: Ionic conductivity, operating temperature and CTE of some of the most diffused electrolytes [12].

Material	Conductivity (S/cm)	Operating temperature (°C)	Thermal expansion coefficient $1 \times 10^{-6}/(K)$
<i>Zirconia based electrolytes</i>			
8 mol.% Y <sub>2</sub> O <sub>3</sub> -ZrO <sub>2</sub>	0.13	1000	-
10.5 mol.% Y <sub>2</sub> O <sub>3</sub> -ZrO <sub>2</sub>	0.034	800	-
10 mol.% Y <sub>2</sub> O <sub>3</sub> -ZrO <sub>2</sub>	$4.52 \times 10^{-6}$	400	10.6
9.5 mol.% Y <sub>2</sub> O <sub>3</sub> -ZrO <sub>2</sub>	0.057	900	-
6 mol.% Sc <sub>2</sub> O <sub>3</sub> -ZrO <sub>2</sub>	0.18	1000	-
9-11 mol.% Sc <sub>2</sub> O <sub>3</sub> -ZrO <sub>2</sub>	0.28-0.34	1000	10.4, 10.9 (8, 10 mol.% Sc <sub>2</sub> O <sub>3</sub> )
<i>Ceria based electrolytes</i>			
Ce <sub>0.85</sub> Gd <sub>0.15</sub> O <sub>2-δ</sub>	$4.07 \times 10^{-2}$	700	-
Ce <sub>0.8</sub> Sm <sub>0.2</sub> O <sub>1.9</sub>	$5 \times 10^{-3}$	600	-
<sup>1</sup> Ce <sub>0.9</sub> Gd <sub>0.1</sub> O <sub>2-δ</sub>			<sup>1</sup> 12.4
<sup>2</sup> Ce <sub>0.8</sub> Gd <sub>0.2</sub> O <sub>2-δ</sub>			<sup>1</sup> 11.8 (27-827 °C) <sup>2</sup> 12.5 (50-1000 °C)
Ce <sub>0.75</sub> Gd <sub>0.25</sub> O <sub>1.875</sub>	$1.01 \times 10^{-2}$	600	-
Ce <sub>0.8</sub> Sm <sub>0.2</sub> O <sub>1.9</sub>	$8.8 \times 10^{-2}$	800	-
Ce <sub>0.83</sub> Sm <sub>0.17</sub> O <sub>1.915</sub>	$5.7 \times 10^{-3}$	600	8.6
Ce <sub>0.8</sub> Y <sub>0.2</sub> O <sub>1.9</sub>	$3.4 \times 10^{-2}$	700	-
Ca, Na doped CeO <sub>2</sub>	$10^{-2}$ - $10^{-1}$	~600	-
Zr <sub>0.75</sub> Ce <sub>0.08</sub> Nd <sub>0.17</sub> O <sub>1.9</sub> )	$3 \times 10^{-4}$	~600	-
Ce <sub>0.8</sub> ) Sm <sub>0.1</sub> Nd <sub>0.1</sub> O <sub>1.9</sub> )	0.012	500	-
<i>LaGaO<sub>3</sub>- and LaAlO<sub>3</sub>-based electrolytes</i>			
La <sub>0.9</sub> Sr <sub>0.1</sub> Ga <sub>0.8</sub> Mg <sub>0.2</sub> O <sub>3-δ</sub>	10.2	800	10.4 (27-800 °C)
La <sub>0.9</sub> Sr <sub>0.1</sub> Ga <sub>0.8</sub> Mg <sub>0.2</sub> O <sub>3-δ</sub> -2 wt.% Al <sub>2</sub> O <sub>3</sub>	8.8	800	11.9 (27-1200 °C) 10.6 (27-800 °C)
La <sub>0.8</sub> Sr <sub>0.2</sub> Ga <sub>0.8</sub> Mg <sub>0.2</sub> O <sub>3-δ</sub>	0.45-0.025	300-800	12.4 (27-1200 °C)

Table 1.3.2: Ionic conductivity, operating temperature and CTE of some of the most diffused electrolytes [12]

$\text{La}_{0.90}\text{Sr}_{0.10}\text{Ga}_{0.76}\text{Mg}_{0.19}\text{Co}_{0.05}\text{O}_{3-\delta}$	~0.30–0.39	100–1000	12.7 (27–1200 °C)
$\text{La}_{0.90}\text{Sr}_{0.10}\text{Ga}_{0.76}\text{Mg}_{0.19}\text{Fe}_{0.05}\text{O}_{3-\delta}$	~0.44–0.39	100–1000	11.6 (27–1200 °C)
$\text{La}_{0.90}\text{Sr}_{0.10}\text{Ga}_{0.45}\text{Al}_{0.45}\text{Mg}_{0.10}\text{O}_{3-\delta}$	~0.25	500	10.9 (27–950 °C)
$\text{La}_{0.9}\text{Sr}_{0.1}\text{Al}_{0.9}\text{Mg}_{0.1}\text{O}_{3-\delta}$	0.7	300–1000	11.2 (27–950 °C)
$\text{La}_{0.9}\text{Sr}_{0.1}\text{ScO}_{3-\delta}$	4.6	300–1000	–
$\text{LaSc}_{0.9}\text{Mg}_{0.1}\text{O}_{3-\delta}$	2	1000	–
$\text{La}_{0.9}\text{Sr}_{0.1}\text{Sc}_{0.9}\text{Mg}_{0.1}\text{O}_{3-\delta}$	1.9	200–1000	–
$\text{La}_{0.9}\text{Sr}_{0.1}\text{InO}_{3-\delta}$	2.3	300–1000	–
<i>Electrolytes with pyrochlore and apatite structure</i>			
$\text{Gd}_2\text{Ti}_2\text{O}_{7+\delta}$	0.44	1000	10.8 (50–1000 °C)
$\text{Gd}_{1.86}\text{Ca}_{0.14}\text{Ti}_2\text{O}_{7-\delta}$	10.44	500–820	10.4 (127–1000 °C)
$\text{La}_{9.83}\text{Si}_{4.9}\text{AlFe}_{0.5}\text{O}_{26-\delta}$	0.46	1000	8.9 (100–1000 °C)
$\text{La}_7\text{Sr}_3\text{Si}_6\text{O}_{24}$	0.51	1000	9.1 (100–1000 °C)
<i>La<sub>2</sub>Mo<sub>2</sub>O<sub>9</sub>- and Bi<sub>2</sub>O<sub>3</sub>-based electrolytes</i>			
$\text{La}_{1.7}\text{Bi}_{0.3}\text{Mo}_2\text{O}_9$	1.4	1000	14.8 (100–350 °C)
$\text{La}_2\text{Mo}_{1.7}\text{W}_{0.3}\text{O}_9$	1.39	1000	16.0 (350–800 °C) 14.4 (100–350 °C)
$\text{Bi}_2\text{V}_{0.9}\text{Cu}_{0.1}\text{O}_{5.5-\delta}$	14.1–10.6	100–750	19.8 (350–800 °C) 15.3 (27–457 °C)
$(\text{Bi}_{0.95}\text{Zr}_{0.05})_{0.85}\text{Y}_{0.15}\text{O}_{1.5+\delta}$	19.2–26.9	250–800	18.0 (457–757 °C) 13.8 (47–437 °C) 16.6 (437–847 °C)

#### 1.4. Fuel electrode materials

In the fuel cell configuration, the fuel electrode represents the negative pole, so where the fuel oxidation reaction occurs; in the reverse condition (SOEC), the fuel electrode acts as positive pole, so where the fuel is formed as product of electrochemical reactions.

The anodic material should be as porous as possible, to let the fuel diffuse inside it and reach the TPBs (triple-phase boundaries, *Figure 1.14*). The TPBs are the surfaces where the oxidation or reduction reactions take place, and they owe their name to three phases coexisting together in this region:

- Electronic phase, represented by a metal that can act also as catalyst for the oxidation or reduction reaction (anode material);
- Ionic phase, the ceramic region where the  $O^{2-}$  are conducted (electrolyte material);
- Fuel phase, which diffuses inside the electrode pores;

The efficiency of the device is strictly related to the presence of TPBs: the higher is their extent the higher will be the efficiency. From this component it is also expected a good chemical stability, especially at high temperature, and a considerable low CTE mismatch with the adjacent components.

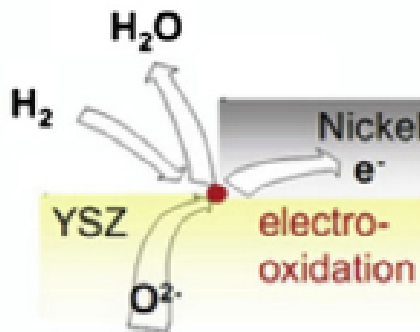


Figure 1.14: Modelling of TPB in the anode structure [12].

The state of art suggests the so-called “cermet” (metal-ceramic mixture) as suitable solution for SOFC/SOEC applications. In the cermet structure the metal ensures the electrical conductivity while the ceramic matrix ensures the ionic conductivity (overall conductivity  $> 100 \text{ Scm}^{-1}$  [22]). Previously adopted solutions are represented by graphite, iron oxide or transition metals, characterized by unacceptable CTEs mismatch with the adjacent components and susceptible to corrosion.

The most common cermet is the Ni/YSZ, a porous material that ensures the best performances in terms of mixed ionic and electronic conductivity (MIEC), making also available a great amount of TPBs that allows the fuel oxidation/reduction in all the anode volume. The  $O^{2-}$  ions cross the anode through the oxygen vacancies in the YSZ lattice, with the ion hopping mechanism already introduced for the YSZ electrolyte. The nickel enhances the electronic conduction in the anode, estimated between  $10^2$  and  $10^4 \text{ S/cm}$  at  $1000^\circ\text{C}$  [12]. Furthermore, the Ni acts as catalyst for the  $H_2$  oxidation, explained by three different kinetics models:

- $H_2$  adsorbed by the Ni, where the  $H^+$  ions are produced; then the ions migrate to the Ni bulk and to the YSZ bulk or to surfaces where the water is produced (*Figure 1.15 a*);
- The  $O^{2-}$  or  $OH^-$  migrate from the SZ to the Ni through their respective surfaces, with the water produced at the Ni surfaces (*Figure 1.15 b*);
- The water is produced at the SZ surfaces, with the electrons that migrate to the Ni through the surfaces or through the SZ bulk (*Figure 1.15 c*);

This cermet is produced starting from a mixture of NiO, ZrO<sub>2</sub> and Y<sub>2</sub>O<sub>3</sub> powders, obtaining the NiO/YSZ after their sintering. NiO is then reduced to metallic Ni. This may be done during the first heating up of the SOCs stack with reducing atmospheres.

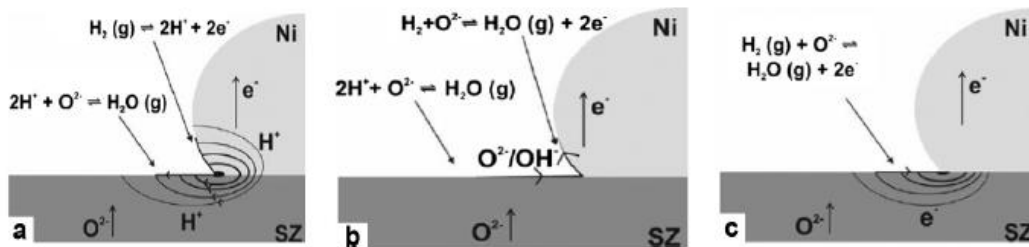


Figure 1.15: three different electrode kinetics models for the hydrogen oxidation [12].

The most common degradation phenomena which affect the anode, schematized in *Figure 1.16*, can be:

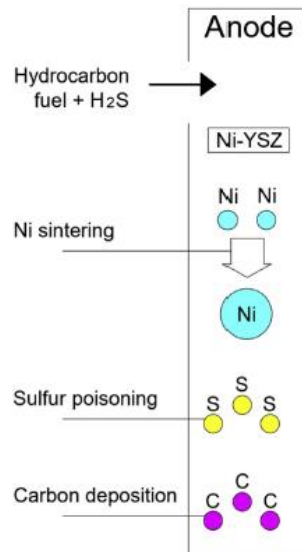


Figure 1.16: possible degradation phenomena occurring at Ni-YSZ anode [17]

- Sulphur poisoning: occurring when impure hydrocarbons or hydrogen are used as fuels. This effect can be hindered by adding BZXYb (BaZr<sub>0.1</sub>Ce<sub>0.7</sub>Y<sub>0.1</sub>Yb<sub>0.1</sub>O<sub>3-δ</sub>) into the starting anode materials [17];
- Activation of the hydrocarbons cracking reaction (*Eq. 1.5*), favoured by the presence of the nickel in the structure and by the high temperatures. The consequence of the hydrocarbons cracking is the production of carbon that can deposit on the electrodes, obstructing their pores and thus hindering the diffusion of the reactants molecules.

Some tests have shown that the addition of silver to the anode materials (0.20% w.t. [17]) minimizes the effects of the carbon deposition in the energy performances of the cell [17];

- Nickel sintering, activated at high operating temperatures and enhanced by the presence of an electric current. The sintering may lead to microstructure modifications and reduce the porosity [12];

The use of Ni-YSZ make the performance of the sealant even more important. Indeed, even a small leakage in the sealant can lead to the re-oxidation of the metallic Ni to NiO with consequent sudden volume expansion which can lead to the failure of the entire cell.

In alternative anodic materials the nickel is substituted with Cu in the Cu/CeO<sub>2</sub> cermet. Copper is still a good catalyst for the electrode reactions, but it avoids the problems of carbon deposition characteristic of the Ni; furthermore, the CeO<sub>2</sub> enhances the hydrogen production from 1.4 cm<sup>3</sup>/min of the 60Ni/40YSZ up to 1.8 cm<sup>3</sup>/s [22]. In the ceria-based anodic materials, the electronic conduction is ensured by the presence of the Cu (Cu/CeO<sub>2</sub>, Cu/CeO<sub>2</sub>/YSZ), which replaces the Ni. In other application, Zr is added to the CeO to further enhance the catalytic activity and to improve the thermal stability. Unfortunately, the absence of the Nickel in these materials leads to low oxidation efficiency, which has been found unsatisfactory for several applications [12].

Nowadays the research is also focusing on the perovskite structured material, such as La<sub>1-x</sub>Sr<sub>x</sub>CrO<sub>3</sub> due to the optimal performance as MIEC and acceptable chemical stability. Transport and catalytic properties of these materials can be tailored by modifying the composition, expressed in the form La<sub>1-x</sub>Sr<sub>x</sub>Cr<sub>1-y</sub>M<sub>y</sub>O<sub>3-δ</sub> (M= Mn, Fe, Co or Ni) [22].

Table 1.4 summarizes the state of art in the anodic materials.

Table 1.4: Vol% composition of the most diffused anodic materials [12]

Material	Composition (vol%)
Ni-YSZ	80Ni:20YSZ
Ni-CeO <sub>2</sub> -ZrO <sub>2</sub>	Mixed oxides
Ni/YSZ	40Ni:60YSZ
LSCM-YSZ-Pd/CYZ	Nitrates reaction in acid
Ni/YSZ	-
Ni/YSZ	60Ni:40YSZ-40Ni:60YSZ
CeO <sub>2</sub>	30% CeO <sub>2</sub> +Co(NO <sub>3</sub> ) <sub>2</sub> and Ce(NO <sub>3</sub> ) <sub>3</sub>
Cu/YSZ	60Cu-40YSZ-40Cu-60YSZ
Ni/YSZ	-
Ni/YSZ	-
Ni-GDC	-
Ni/BCZY	65Ni:35BCZY
Ni/YSZ	60Ni:40YSZ
La <sub>0.98</sub> Mg <sub>0.02</sub> NbO <sub>4</sub>	Molten salts
Ni/YSZ	60Ni:40YSZ
SFMO <sup>a</sup>	-
Ni/ScSZ	-
CeO <sub>2</sub> /Pd	Oxides and Nitrates
LSCM	Oxides as Precursors
LST	Oxides as Precursors
LSCrF	Metal Nitrates
LCaCrF	Metal Nitrates

## 1.5. Air/oxygen electrode materials

The oxygen electrode represents the positive pole of a fuel cell, where the oxygen reduction reaction occurs; on the contrary, it represents the negative pole in the electrolytic configuration. The cathode features and requirements are similar to the those introduced about the fuel electrode, so a considerable electrical conductivity, catalytic activity and compatibility with other materials are expected.

One of the first cathode material adopted is  $\text{La}_{1-x}\text{Sr}_x\text{MnO}_3$  (LSM). The high operating temperatures guarantee an optimal electronic conduction through the material, allowed by the presence of rhombohedral or tetragonal lattice distortion [10]; furthermore, the CTE mismatch of the LSM with the YSZ electrolyte is almost negligible.

The mechanism of the oxygen reduction process can be considered as resulting from the sum of three consequential phenomena [10]:

- 1- Adsorption of the oxygen on the surface of the porous cathodic material;
- 2- Diffusion of the adsorbed oxygen towards the TPB;
- 3- Reduction of the adsorbed oxygen;

The oxygen reduction process for a pure electrons conductor material is limited in reduced portion of the TPB, namely the interface between the cathode and the electrolyte, as represented on *Figure 1.17 a*. To enhance the reduction mechanism, new perovskite-based materials (*Figure 1.18*), with a disordered structure and a chemical composition that allow also the ionic conduction, obtaining the so-called MIEC materials. Because of the adoption of this new class of materials, the adsorption or reduction of the oxygen can occur in the entire volume of the cathode, being the  $\text{O}_2$  able to diffuse inside cathode through the oxygen vacancies in its lattice (*Figure 1.17 b*).

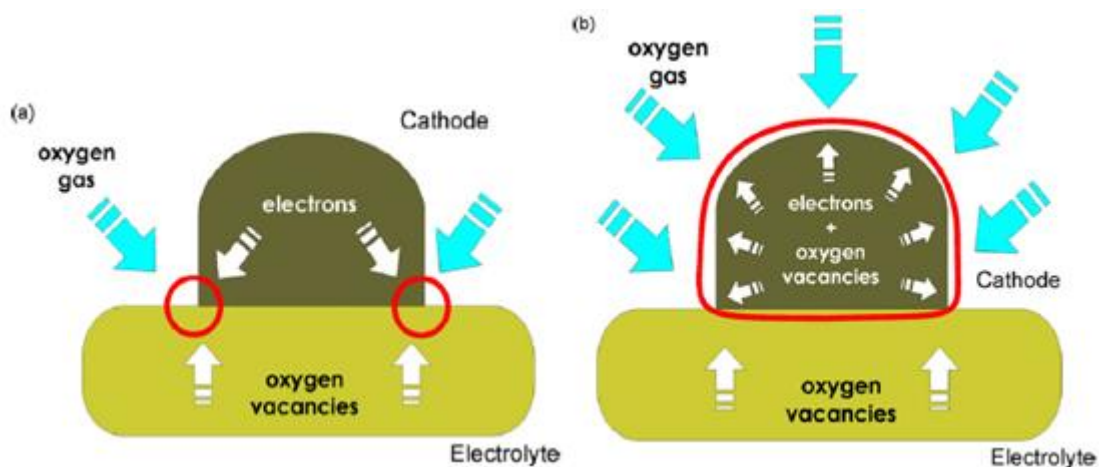


Figure 1.17: Reduction process for a pure electron conductor cathode material (a) and for a MIEC cathode material (b) [10].

Potential MIEC cathode materials are classified in two main groups [12]:

- $\text{Ln}_{1-x}\text{Sr}_x\text{Co}_{1-y}\text{Fe}_y\text{O}_{3-\delta}$ , where Ln refers to La, Sm, Nd, Gd or Dy;
- $\text{Ln}_{1-x}\text{A}_x\text{M}_{1-y}\text{Mn}_y\text{O}_{3-\delta}$ , where Ln refers to La, Nd or Pr, A refers to Ca or Sr and M refers to the 3d metals except for Mn;

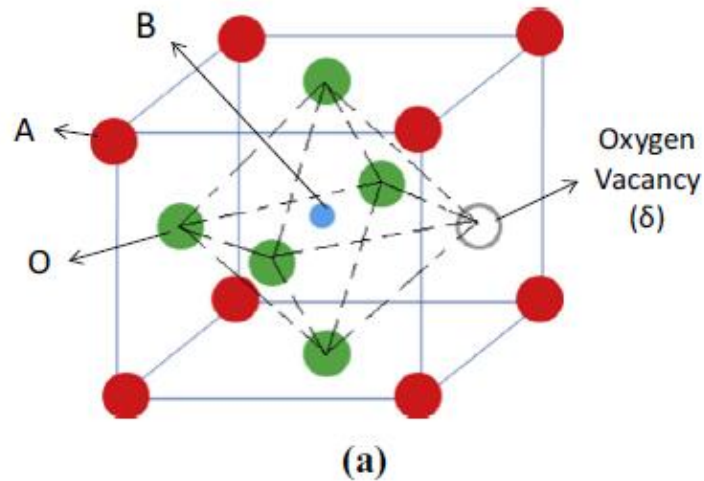


Figure 1.18: Perovskite structure ( $ABO_3$ ) and  $\delta$  oxygen vacancies [12].

The LSCFs (strontium-based materials doped with  $LaCoO_{3-\delta}$ ) is the most used compounds belonging to the first group. It shows good ionic-electronic conductivity values ( $650 \text{ S cm}^{-1}$  at  $800^\circ\text{C}$ ), but a too high CTE mismatch with the main electrolyte materials. A CTE close to the other components has been found for the  $Ln_{1-x}Sr_xFeO_{3-\delta}$ , which unfortunately has an insufficient conductivity value [10].

LSM-based electrode degradation can be related to different phenomena, depending on the operating condition of the cell; the degradation generally increases with the working temperature and with current density applied, but in a SOFC stack the degradation rate is considerable lower than that of the SOEC (0.5%/1000 h for 19000 h against 20% for 1000/2000 h respectively [22]). On the contrary, for LSCF-based electrodes the degradation rate difference between the two operational modes is reduced (0.6-1.4%/1000 h for a SOFC against 5.6%/1000 h for 4000 h for a SOEC [22]), because of a better behaviour on the SOEC configuration.

## 1.6. Interconnect materials

The interconnect represents the physical separation between the electrodes of two adjacent cells in a stack, providing also their electrical connection. For this, the electrical area specific resistance (ASR) of the material should be lower than  $0.1 \Omega \text{ cm}^2$  [12].

An optimal interconnect should be chemical stable in a dual atmosphere (both reducing and oxidizing) at high temperature. To avoid thermal-mechanical stresses, the CTE mismatch with the other components must be reduced as much as possible.

Ceramic materials for the realization of interconnects have been chosen as possible candidates due to their chemical stability in dual atmosphere and to their compatibility with the other cell components. Semiconductors oxides are preferable, having electric conductivity values acceptable at temperatures around  $800^\circ\text{C}$ , but insufficient at  $600^\circ\text{C}$ . The most used semiconductor ceramic material is the  $\text{LaCrO}_3$ ; it's a p-type semiconductor with an electrical conductivity of  $1 \text{ S/cm}$  at  $1000^\circ\text{C}$  [12]. It possesses also a good chemical stability and CTE compatibility with the other components. *Table 1.5* shows the electrical resistivity and the CTE of the most common ceramic interconnects.

Table 1.5: CTE and electrical conductivity several  $\text{LaCrO}_3$ -based materials. [12]

Ceramic based Interconnects	CTE ( $\times 10^{-6}/\text{K}$ )	Electrical conductivity (S/cm)
$\text{LaCrO}_3$	9.5	0.34 at $700^\circ\text{C}$ , 1 at $1000^\circ\text{C}$
$\text{LaCr}_{0.9}\text{Mg}_{0.1}\text{O}_3$	9.5	3 at $1000^\circ\text{C}$
$\text{La}_{0.9}\text{Sr}_{0.1}\text{CrO}_3$	10.7	11.2 at $1000^\circ\text{C}$
$\text{La}_{0.7}\text{Sr}_{0.3}\text{CrO}_3$	19	15 at $700^\circ\text{C}$
$\text{La}_{0.7}\text{Ca}_{0.3}\text{CrO}_3$	14.6	18 at $700^\circ\text{C}$
$\text{La}_{0.95}\text{Ca}_{0.05}\text{CrO}_3$	10.8	2.3 at $700^\circ\text{C}$
$\text{La}_{0.8}\text{Ca}_{0.2}\text{CrO}_3$		7.1 at $700^\circ\text{C}$ , 35 at $1000^\circ\text{C}$
$\text{LaCr}_{0.9}\text{Co}_{0.1}\text{O}_3$	13.1	-
$\text{LaCr}_{0.8}\text{Co}_{0.2}\text{O}_3$	14.6	-
$\text{LaCr}_{0.6}\text{Co}_{0.4}\text{O}_3$	18.7	-
$\text{LaCr}_{0.2}\text{Co}_{0.8}\text{O}_3$	20.9	-
$\text{La}_{0.7}\text{Ca}_{0.3}\text{Cr}_{0.5}\text{Co}_{0.5}\text{O}_3$	-	85 at $700^\circ\text{C}$
$\text{La}_{0.8}\text{Ca}_{0.2}\text{Cr}_{0.9}\text{Co}_{0.1}\text{O}_3$	11.1	-
$\text{La}_{0.8}\text{Ca}_{0.2}\text{Cr}_{0.8}\text{Fe}_{0.2}\text{O}_3$	-	9.2 at $700^\circ\text{C}$
$\text{La}_{0.8}\text{Ca}_{0.2}\text{Cr}_{0.8}\text{Ni}_{0.2}\text{O}_3$	-	18 at $700^\circ\text{C}$
$\text{La}_{0.7}\text{Sr}_{0.3}\text{Cr}_{0.5}\text{Co}_{0.5}\text{O}_3$	19	58 at $700^\circ\text{C}$
$\text{La}_{0.87}\text{Sr}_{0.1}\text{Cr}_{0.95}\text{Cu}_{0.05}\text{O}_3$	9.81	23.9 at $1000^\circ\text{C}$
$\text{La}_{0.9}\text{Sr}_{0.1}\text{Cr}_{0.95}\text{V}_{0.05}\text{O}_3$	9.87	9.7 at $1000^\circ\text{C}$
$\text{La}_{0.9}\text{Sr}_{0.1}\text{Cr}_{0.9}\text{Mg}_{0.05}\text{V}_{0.05}\text{O}_3$	9.64	15.2 at $1000^\circ\text{C}$
$\text{La}_{0.87}\text{Sr}_{0.1}\text{Cr}_{0.935}\text{Cu}_{0.05}\text{Co}_{0.015}\text{O}_3$	10.4	25.6 at $1000^\circ\text{C}$
$\text{La}_{0.85}\text{Sr}_{0.15}\text{Cr}_{0.935}\text{V}_{0.05}\text{Co}_{0.015}\text{O}_3$	10.5	22.9 at $1000^\circ\text{C}$
$\text{La}_{0.95}\text{Sr}_{0.05}\text{Cr}_{0.85}\text{Mg}_{0.1}\text{V}_{0.05}\text{O}_3$	9.22	12.9 at $1000^\circ\text{C}$
$\text{La}_{0.85}\text{Sr}_{0.15}\text{Cr}_{0.95}\text{V}_{0.05}\text{O}_3$	10	19.9 at $1000^\circ\text{C}$
$\text{La}_{0.85}\text{Sr}_{0.15}\text{Cr}_{0.98}\text{Cu}_{0.02}$	9.91	32.5 at $1000^\circ\text{C}$
$\text{LaCr}_{0.6}\text{Ni}_{0.4}\text{O}_3$	>11.8	26 at $700^\circ\text{C}$
$\text{LaCr}_{0.9}\text{Ni}_{0.1}\text{O}_3$	10.1	-
$\text{LaCr}_{0.8}\text{Ni}_{0.2}\text{O}_3$	11.2	-
$\text{LaCr}_{0.7}\text{Ni}_{0.3}\text{O}_3$	11.8	-
$\text{La}_{0.7}\text{Ca}_{0.3}\text{Cr}_{0.8}\text{Co}_{0.2}\text{O}_3$	>11.1	45 at $700^\circ\text{C}$
$\text{La}_{0.95}\text{Ca}_{0.05}\text{Cr}_{0.5}\text{Co}_{0.5}\text{O}_3$	-	63 at $700^\circ\text{C}$

To enhance the electronic conductivity, the  $\text{LaCrO}_3$  can be doped with Ca or Sr, which substitute La in the perovskite structure (*Figure 1.19 a and b*).

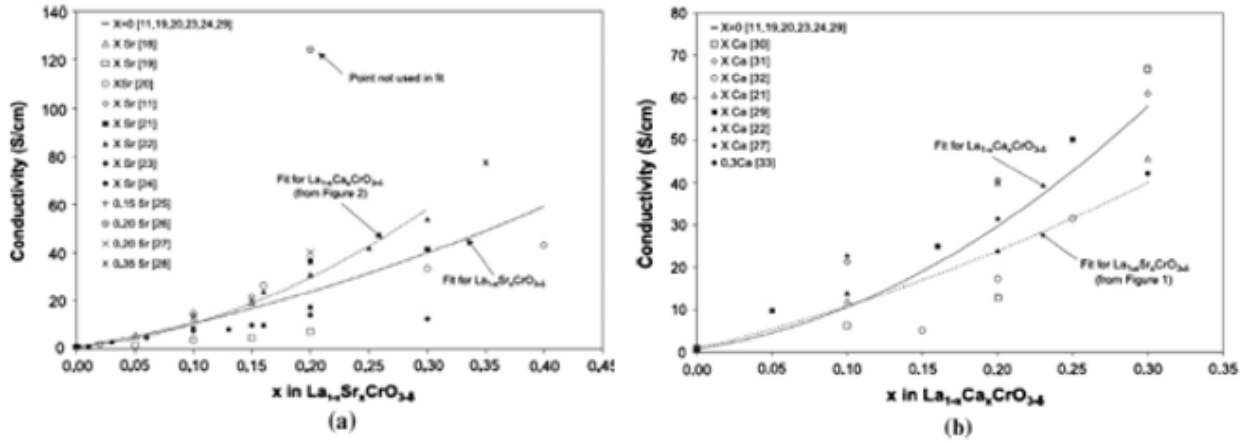
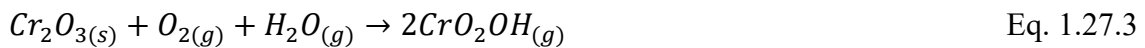


Figure 1.19: Electrical conductivity measured at 1000°C in air of  $\text{LaCrO}_3$  doped with Sr (a) and Ca (b) [12].

A second solution able to improve the electronic conductivity and to reduce the CTE mismatch is to dope  $\text{LaCrO}_3$  with Ni or Cu, which substitute the Cr cations in the structure. Both the doping solutions can be performed together, obtaining the best configuration.

Actually, the most promising solution under development is the utilization of metal interconnects. With the lowering of the operating temperature below 1000°C, the use of special metallic materials is permitted. This family of metal interconnect materials includes Fe-Cr based alloys, Cr-based alloys, Ni(Fe)-Cr based alloys and austenitic and ferritic stainless steel. Metallic alloys ensure the best performances in terms of electronic conductivity in comparison with their ceramic counterpart, but they are subjected to oxidation in air. Ferritic stainless steels interconnects contain Cr in their structure, a metal with a preferential oxidation at high temperature that leads to the formation of a protective layer of  $\text{Cr}_2\text{O}_3$ , able to reduce the oxidation processes and avoid corrosion. In addition, the  $\text{Cr}_2\text{O}_3$  is a semiconductor material so it does not lower the electronic resistivity so much in comparison with other alloys which are passivated with insulating layer. However, the overall electrical resistivity of the formed scale is much higher than the one of the steel itself, so an excessive increasing in the scale thickness would mean and increase in the electrical resistivity [12]. Nevertheless, Cr-containing ferritic stainless steel are the most diffused interconnect materials for rSOCs, but they are still under development to reduce the Cr volatilization, a process occurring at high temperatures and related to the formation of volatile Cr species. The main volatile chromates are  $\text{CrO}_3$ ,  $\text{CrO}_2\text{OH}$  and  $\text{CrO}_2(\text{OH})_2$ , produced by the following reactions [12]:



The volatile chromium species can be reduced at the cathode surface, forming  $\text{Cr}_2\text{O}_3$  which deposits on the TPB and fills the reaction sites as shown in *Figure 1.20*, with a considerable degradation of the cell.

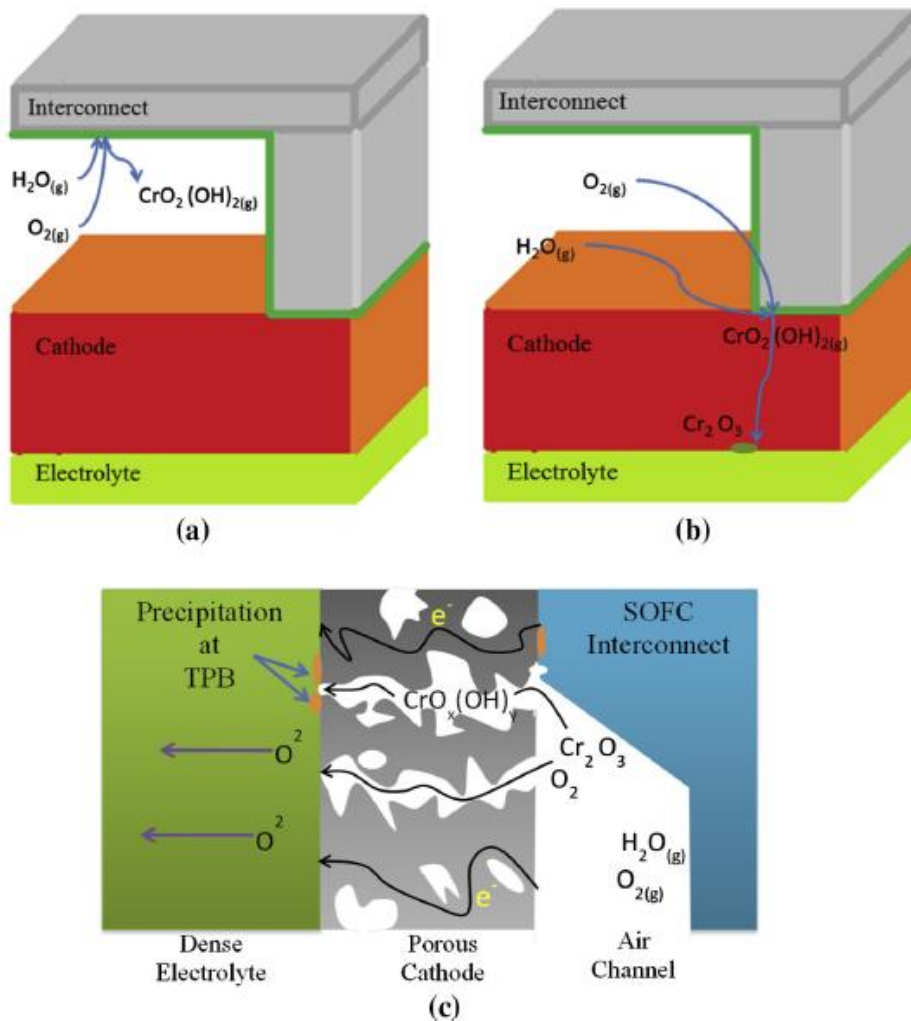


Figure 1.20: Schematic representation of the  $\text{CrO}_2(\text{OH})_2$  formation at the interconnector surface (a),  $\text{CrO}_2(\text{OH})_2$  formation at the interconnector surface and consequent reduction in  $\text{Cr}_2\text{O}_3$  and deposition on the TPB (b) and evaporation of Chromium species and deposition on the TPB (c). [12].

In the most diffused Cr-containing stainless steel alloys, the considerable amount of Cr (20-24%w.t. [12]) is a first solution against the interconnector degradation, thanks to the formation of a continuous layer of  $\text{Cr}_2\text{O}_3$ . However, as said, before an excessive growth of the scale can lead to an increase in the electrical resistance and to delamination phenomena between the steel and the scale with consequent corrosion development.

Several protective coatings have been proposed and tested to overcome the above-mentioned problems, considering that the identified materials have to be chemical compatible and stable with the other components, with high electronic conductivity and with low Cr and O diffusion. The most promising ones are  $(\text{Mn}, \text{Co})_3\text{O}_4$  spinels-based coatings [13]. These coatings were demonstrated to be able to reduce up to a factor of 10 the Cr oxidation rate, ensuring a longer life of the component. To reinforce more the oxidation resistance of the alloy, a further solution is the pre-oxidation of the component, a heat treatment performed in air.

## 1.7. Green Industrial Hydrogen

The GrInHy project (Green Industrial Hydrogen via reversible high temperatures electrolysis) represents one of the most promising and ambitious programs for the design, manufacturing and operation of reversible solid oxide cells. The rSOCs stacks are thought to flank plants with considerable productions of waste heat (such as steel and iron works plants, as represented in *Figure 1.21*), which can be exploited in form of steam in high efficiency electrolysis processes for the production of green hydrogen. The electricity requirements for the electrolytic redox reactions are satisfied by renewable energy sources, like photovoltaic plants or wind turbines. The green hydrogen is produced by SOCs electrolysis processes with efficiencies over 80%<sub>LHV</sub> (*Figure 1.22*), and it's stored for future utilizations such as:

- Alternative fuel for the combustion processes occurring inside the flanked plant, otherwise fed by fossil fuels, ensuring a considerable reduction of the CO emissions;
- Alternative fuel in the rSOCs power production mode with efficiency of 50%<sub>LHV</sub>, substituting the natural gas or the plants process gases in exceed;

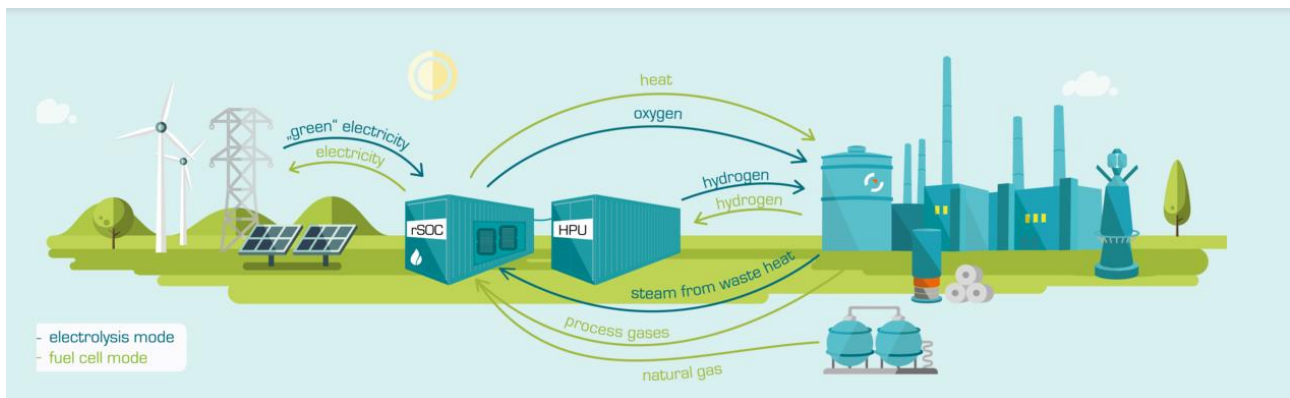


Figure 1.21: Schematic representation of the Green Industrial Hydrogen project

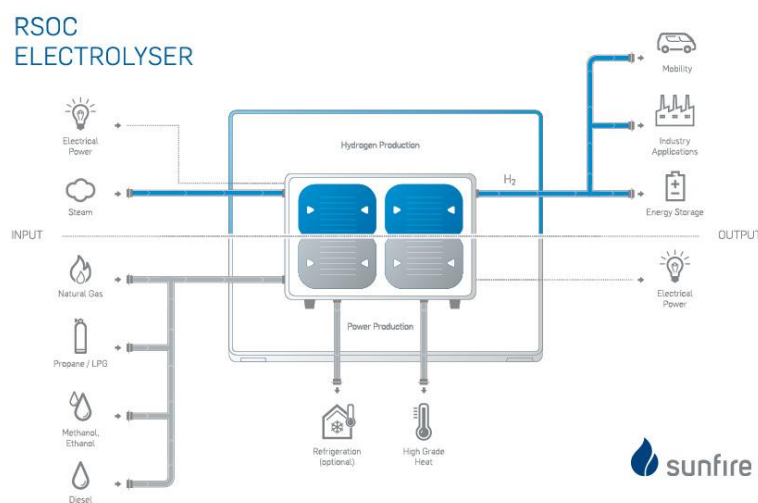


Figure 1.22: Schematic representation of a rSOC electrolyser.

The main specifications of the rSOCs modules are listed in *Table 1.6I*, *Table 1.7* and *Table 1.8*

Table 1.6: Overall specifications of the rSOC modules adopted in the GrInHy.

<b>Overall Specifications</b>	
<b>Model</b>	150/30 RSOC Generator
<b>RSOC Generator</b>	RSOC Module with max. 40 Nm <sup>3</sup> /h Hydrogen output and max. 30 kW <sub>AC</sub> power output
<b>Installation</b>	20' ISO container (RSOC module without auxiliary components)
<b>Model</b>	150/30 RSOC Generator

Table 1.7: Main specifications of the rSOC modules adopted in the GrInHy in hydrogen production mode.

<b>Hydrogen production</b>	
<b>Power Input (100%) (AC)</b>	150 kW <sub>AC</sub> ± 5 %
<b>Hydrogen production (100%)</b>	40 Nm <sup>3</sup> /h ± 5 %
<b>Electrical efficiency (based on lower heating value of hydrogen)</b>	>80 %
<b>Dynamics</b>	30...125 % hydrogen output (BoL)

Table 1.8: Main specifications of the rSOC modules adopted in the GrInHy in power production mode.

<b>Power production</b>	
<b>Power output (100%) (AC)</b>	NG/CH <sub>4</sub> operation: 25 kW <sub>AC</sub> ± 10 % Hydrogen operation: 30 kW <sub>AC</sub> ± 10 %
<b>Electrical efficiency (based on LHV)</b>	NG/CH <sub>4</sub> operation: <ul style="list-style-type: none"> <li>· 50 % ± 2 % points (full load)</li> <li>· 55 % ± 2 % points (part load)</li> </ul> Hydrogen operation: <ul style="list-style-type: none"> <li>· 47 % ± 2 % points (full load)</li> <li>· 53 % ± 2 % points (part load)</li> </ul> Other flammable gases possible
<b>Dynamics</b>	30...100 %

The research on rSOC technologies is conducted by Sunfire and The Boeing Company, which have realized systems with two identical submodules of 100 kW<sub>AC</sub> in SOEC mode, 20 kW<sub>AC</sub> in SOFC mode and 600 kWh of storage capacity

## 2. Sealing technologies for solid oxide cells

In the rSOCs planar stack configuration, a very important component is the sealant, whose main function is to avoid gas mixing with consequent efficiency decreasing and degradation phenomena development. Depending on the stack design, the sealant can be used to join different components, i.e. metallic interconnect to ceramic electrolyte (*Figure 2.1*) or metallic interconnect to metallic frame.

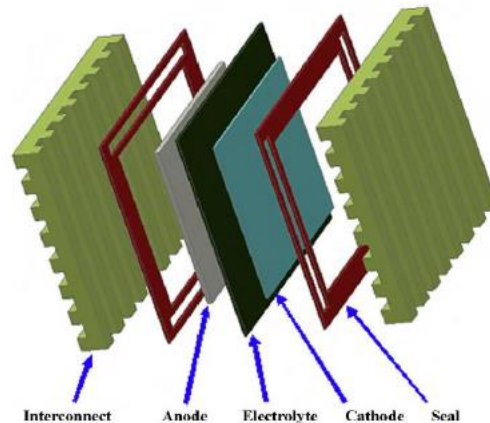


Figure 2.1: Reversible oxide cell main components.

Due to the severe operating environment typical for SOC applications, a good sealant needs to satisfy strict requirements, and for this the selection of the sealant material is crucial. To ensure the best stack performances and to make the technology as durable and strong as possible, a suitable sealant should possess the following features, also summarized in the *Table 2.1*:

- Gas hermeticity, to avoid leakages and the contact between the reactants;
- Optimal adhesion with the joined materials;
- High electrical resistivity, to guarantee the electrical insulation and avoid current shunting;
- Chemical stability in dual atmosphere (oxidizing at the anode and wet-reducing at the cathode) and chemical compatibility with other materials;
- It has to be able to work at high temperature (800-900°C) and to withstand to several thermal cycles;
- It has to be characterized by thermo-mechanical properties as closer as possible to the that of the other cell components, with a CTE (Coefficient of Thermal Expansion) around  $9-12 \cdot 10^{-6} \text{ K}^{-1}$ , to avoid excessive thermo-mechanical stresses;
- It has to be cheap, flexible and easy to produce;

Table 2.1: Properties and requirements of a SOFC/SOEC seal [18]

Properties	Requirements
Thermal properties	Thermal expansion coefficient at $9.5\text{--}12.0 \times 10^{-6} \text{ } ^\circ\text{C}^{-1}$ Thermally stable for $\sim 5000$ h for mobile applications and for $\sim 50,000$ h for stationary applications at $650\text{--}900^\circ\text{C}$ cell operating temperatures
Chemical properties	Resistant to vaporization and compositional change in stringent oxidizing and wet reducing atmospheres at $650\text{--}900^\circ\text{C}$ Limited or no reaction with other cell components
Mechanical properties	Withstand external static and dynamic forces during transportation and operation Resistant to thermal cycling failure during start-up and shut-down of cell stacks
Electrical properties	Electrical resistivity $\geq 10^4 \Omega \text{ cm}$ at operating temperature Electrical resistivity greater than $500 \Omega \text{ cm}$ between cells and stacks at nominal stack operating condition ( $0.7 \text{ V}$ at $500\text{--}700 \text{ mA/cm}^2$ )
Sealing ability	Sealing load $< 35 \text{ kPa}$ Withstand differential pressure up to $14\text{--}35 \text{ kPa}$ across a cell or stack Total fuel leakage $< 1\%$ for the duration of the cell life
Fabrication flexibility	Flexible design, low processing cost, and high reliability

Up to now two, different approaches have been considered for sealing technology in SOCs stacks (*Table 2.2*):

- *compressive seals* (metallic compressive seals and mica based compressive seals): the sealing material is compressed between the components to be sealed through the application of an external load, which ensures the bond and the gas hermeticity. The sealed surfaces are not chemically bonded to the sealant, so the issue of the CTEs mismatch between the components is overcome.
- *rigid seals* (glasses, glass-ceramics and metallic brazes): the sealing material is chemically bonded with the adjacent components, and for this reason the CTEs mismatch must be reduced as much as possible to avoid possible thermal-mechanical stresses;

Table 2.2: advantages and disadvantages of different SOFC/SOEC sealant families [18]

Seal type	Advantages	Disadvantages
Compressive seal	Easy replacement of seals in a malfunctioning cell stack Resistance to thermal cycling	Application of external load Complex design and high cost High gas leakage rate Unsuitable for mobile applications Poor stability Electrically conductive
Rigidly bonded seal	Hermetic sealing Tailorable performance by composition design High electrical resistivity Suitable for stationary and mobile applications Flexible in design and fabrication	Brittle at low temperatures Poor resistance to thermal cycling Chemical reaction with other cell components

## 2.1. Metallic compressive seals

Metals, due to their ductile nature, are flexible enough to deform under the application of external loads, so they represent one of the simpler compressive sealing technologies. On the other hand, it is important to take into account the elevated electronic conductivity of these materials and their considerable tendency to be oxidised in air/oxygen at high temperature.

The choice of the metal material to be adopted for rSOC applications is restricted to noble metals, namely platinum, gold or silver, which are able to withstand to the operating temperatures of the cells thanks to melting temperatures higher than 900°C. By an economic point of view, silver compressive seals represent the most reasonable solution.

Silver has a melting temperature of 961°C, and its utilization as sealant in SOFC/SOEC applications is strictly related to its compressive strength, that must belong to a certain critical range. In general, a strength lower than 2-3 times the other sealed materials is required, otherwise the compression required to achieve an effective sealing may be too high and lead to the failure of other stack components [14].

The exposition to both oxygen (cathode side) and hydrogen (anode side) in the fuel cell configuration has showed a problematic solubility of oxygen and hydrogen in silver, with the consequent production of water that leads a high degree of porosity and even to the failure of the seal [14].

C-shaped gasket compressive seals made of superalloys have displayed both optimal oxidation and high temperatures resistance [12]. The main issue with this solution is related with their deformability, lower than that of silver; for this reason, and to enhance also the gas tightness, the surfaces of the sealant can be coated by a more ductile metal (e.g. Cu or Ag) or combined by brazing with a rigid seal [14].

## 2.2. Mica-based compressive seals

A second main group of sealants in the field of the compressive seals are the mica-based materials, often adopted due to their high electrical resistivity. Mica is a mineral belonging to the family of the phyllosilicates materials, composed by parallel sheets of silicates which make the structure resistant to thermal stresses. In the SOFC/SOEC sealing applications, the mica crystals or particles are arranged in plate-like form, which when subjected to an external load are able to provide gas tightness.

The most used mica-based sealants are the muscovite (potassium aluminium silicate hydroxide fluoride  $\text{KAl}_2(\text{AlSi}_3\text{O}_{10})(\text{F},\text{OH})_2$ ), in the forms of crystals or paper, and the phlogopite (potassium magnesium aluminosilicate hydroxide  $\text{KMg}_3(\text{AlSi}_3\text{O}_{10})(\text{OH})_2$ ), in papers form. The main physical properties related to the above-mentioned elements are listed in *Table 2.3*:

Table 2.3: Physical properties of muscovite and phlogopite micas [15]

Property	Muscovite	Phlogopite
Color	Ruby/green	Amber/yellow
% Chemical water	4.5	3.0
Volume resistivity at 25°C ( $\Omega \text{ cm}$ )	$40 \times 10^{13}$ to $2 \times 10^{17}$	$1 \times 10^{12}$
Tensile strength (MPa)	170	105
Compressive strength (MPa)	190–220	No data
CTE perpendicular to cleavage plane ( $^{\circ}\text{C}^{-1}$ )	$9 \times 10^6$ to $36 \times 10^6$	$30 \times 10^6$ to $60 \times 10^6$
Thermal conductivity perpendicular to cleavage plane ( $\text{W m}^{-1} \text{ }^{\circ}\text{C}^{-1}$ )	0.52	0.43

A sealant made only of compressed mica (*Figure 2.2 a*) is not able to ensure a sufficient hermeticity, especially at the interfaces between the joined materials, where the gas-tightness is estimated to be few orders of magnitude higher than that of a glass-based seal ( $2.41 \times 10^{-4}$  sccm [12]). Therefore, a mica-based seal is typically enhanced by the addition of a compliant layer made of Cu, Ag or glass, as shown in *Figure 2.2b*. Mica and metal can be combined also placing the mica particles into the gaps in a corrugated metal seal (*Figure 2.2c*).

The last improvement suggested for this sealing technology is the addition of an infiltrate phase, such as the bismuth nitrate ( $\text{Bi}(\text{NO}_3)_3$ ), that fills the gaps and joins the mica particles, further enhancing the gas-tightness of the material (*Figure 2.2d*). These solutions are referred as hybrid-sealant.

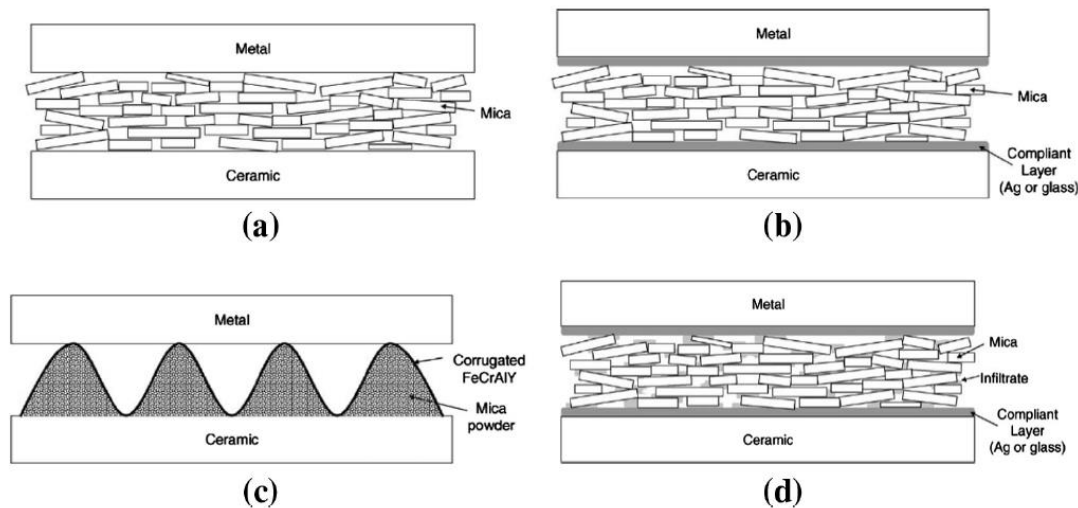


Figure 2.2: schematic representation of a compressive mica-based seal (a), hybrid mica-based seal obtained by adding a compliant layer at the interfaces (b), hybrid mica-based seal obtained by combining the mica powders with a corrugate metal seal (c), hybrid mica-based seal obtained by adding a compliant layer at the interfaces and an infiltrate phase (d) [12]

Figure 2.3 and Table 2.4 compares the leakage rates for different compressive mica-based sealants for different compressive load applied. The mica with the best behaviour is the muscovite arranged in cleaved crystals, a spite of the phlogopite paper and the muscovite paper. Higher thicknesses further enhance the gas-tightness, but the best improvement is represented by the glass compliant layers, which are more effective than that silver. Looking at long-term, the best hybrid configuration is obtained combining the phlogopite papers with an infiltrate phase of bismuth and with a compliant layer of glass at the interfaces, characterized by a leak rate decreasing with time. On the contrary, the leakages rates of muscovite cleaved crystals-based seals combined with silver tend to decrease with time in absence of an infiltrate phase. All the main leak rates values for different solutions are reported in the next figure [16].

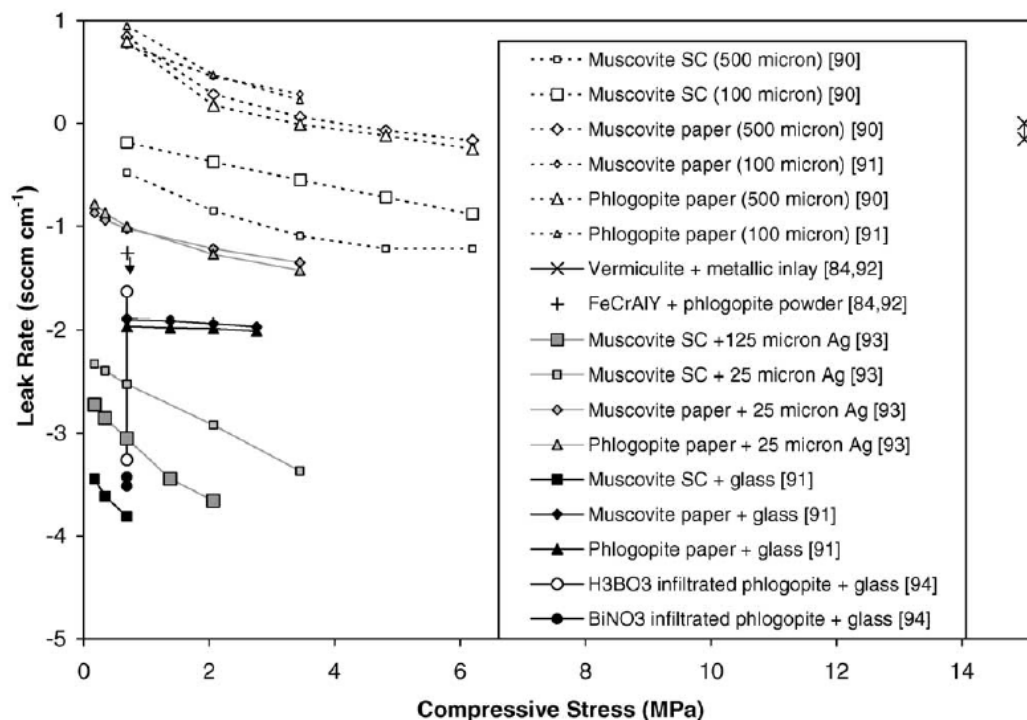


Figure 2.3: Leak rates of different mica-based technologies as a function of the compressive strength applied [14].

Table 2.4: leak rates of mica-based (plain) sealants and hybrid systems at 800°C at different compressive strength applied [16]

Compressive stress (psi)	Leak rate (sccm/cm)							
	Muscovite single crystal				Muscovite paper		Phlogopite paper	
	Plain <sup>2</sup>	Hybrid (glass) <sup>3</sup>	Hybrid (25 μm Ag)	Hybrid (125 μm Ag)	Plain	Hybrid (25 μm Ag)	Plain	Hybrid (25 μm Ag)
25		0.000359	0.0047	0.0019		0.134		0.164
50		0.000243	0.0040	0.0014		0.114		0.134
100	0.65	0.000155	0.0030	0.00089	5.77	0.094	8.85	0.098
200				0.00036				
300	0.42		0.0012	0.00022	2.84	0.060	2.97	0.053
400								
500	0.28		0.00043		1.92	0.044	1.68	0.037

### 2.3. Metallic brazes

The plastic deformation behaviour and the low stiffness of metallic materials make them able to withstand to considerable thermo-mechanical stresses, therefore metallic brazes are an attractive solution in the field of the rigid seals for reversible solid oxide cells.

Thanks to their appreciable resistance in both reducing and oxidizing atmosphere, even at high temperatures, brazes made of Ag and Au are very effective solutions. However, many studies are focusing on the improvement of their wettability on ceramic surfaces. Nowadays, several solutions have been introduced to solve the wettability issue [12, 14]:

- Addition of reactive elements, such as Ti, Hf or Zr, that reduce the oxide formations;
- Use the thermite reaction between Al and Ni to create a chemical bond between the FeCr alloy and the YSZ;
- Use of a mixture of metal and oxide which exhibits eutectic reactions in air;

The last solution is generally the most used, with the addition of Ag-CuO that reduces the contact angle on all the materials, increasing the bonds strength, as explained in *Figure 2.4*.

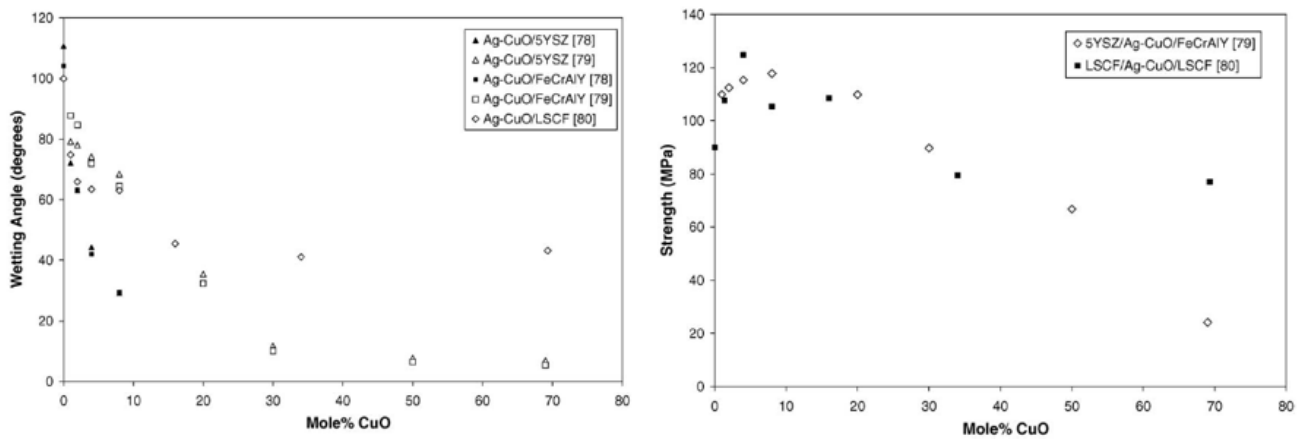


Figure 2.4: Wetting angle of Ag-CuO (left) and bond strength (right) with different cell components as a function of the Ag-CuO concentration [14],

## 2.4. Glass and glass-ceramic sealants

Nowadays, glasses and glass-ceramics are the most used materials as sealants for reversible solid oxide cells thanks to the possibility to modify their properties tailoring their composition.

A glass is an amorphous material characterized by a disordered atomic structure at long range (*Figure 2.5 b*), similar to the one of the liquid from which it is derived. In a disordered three-dimensional structure, the molecules are bonded in a casual orientation and distance, so the chemical bond strength is different in each part of the structure; therefore, it is impossible to identify a precise melting temperature for a glass, which is a parameter proper of the crystalline structured materials (*Figure 2.5 a*).

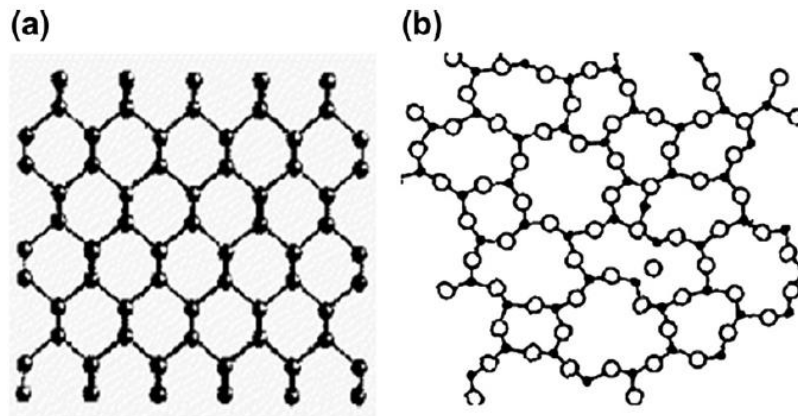


Figure 2.5: Crystalline structure (a) and amorphous structure (b) [20]

The amorphous structure is due to the high viscosity of the melted material, which does not allow the molecules to flow and to arrange in an ordered crystalline structure during the cooling process. The viscosity of an amorphous material is a function of the temperature, increasing when the temperature decreases; *Figure 2.6* shows a typical temperature viscosity curve of a glass. On the basis of viscosity values, some characteristic temperatures can be defined for a glass; the most important are: the glass transition temperature ( $T_g$ ) and the softening temperature ( $T_s$ ). In particular,  $T_g$  represents the temperature below which the glass behaves as a rigid solid, while at temperatures higher than  $T_g$  it shows a viscous flow behaviour. The literature suggests an average viscosity of  $10^{11.3}$  Pa s at the  $T_g$  and viscosity of  $10^{6.6}$  Pa s at the  $T_s$  (Littenton softening point) [19].

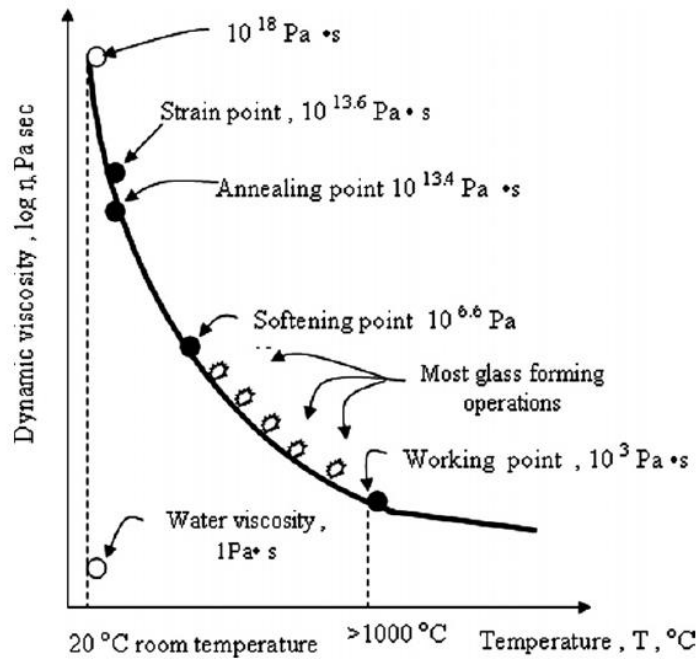


Figure 2.6: Temperature-viscosity curve of a glass [20]

In general, joining treatments of glass-based sealants are carried out above the softening temperature, aiming to obtain an effective viscous flow which can lead to an effective sintering; furthermore, the material flows through the sealed interfaces providing good adhesion and hermeticity. The presence of a glassy phase may also be beneficial thanks to the possible self-healing effects that may develop at the operating temperatures. Characteristic temperatures (i.e.  $T_g$  and  $T_s$ ) and other properties of a glass (such as the CTE or the viscosity) can be tailored by modifying its composition.

The volume variations with the temperature of a glass are functions of two temperature-affected contributions [21]:

- the thermal vibration, which regulates the distance between the bonded molecules;
- the free volume, which regulates the configuration, namely the relative position between the molecules.

Following the curve in *Figure 2.7*, when the temperature decreases the molecules come closer to each other due to the thermal vibration contribution, but they would need longer periods to change their relative position because the viscosity increasing makes this process more difficult. The temperature at which the viscosity is such high to “freeze” the molecular configuration is the glass transition temperature. At this temperature, it corresponds an inflexion point in the temperature-specific density curve of the glass (red point in *Figure 2.7*); below this value, the shrinkage is ensured only by the thermal vibration contribution, while the specific density which will have a lower increment.

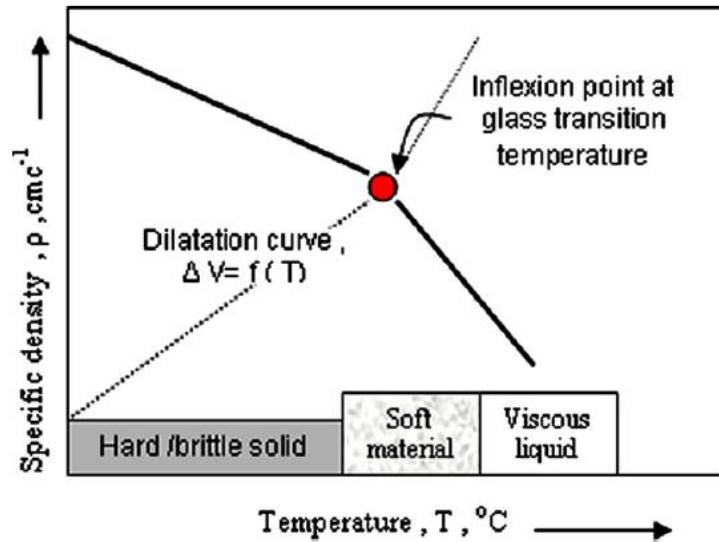


Figure 2.7: Temperature – specific density curve of a glass [20].

It is important to clarify that the glass transition temperature is defined experimentally into a certain range, because it's affected by the cooling rate of the melting process, as shown in *Figure 2.8* [21]; generally, fast cooled glasses have higher melting temperature.

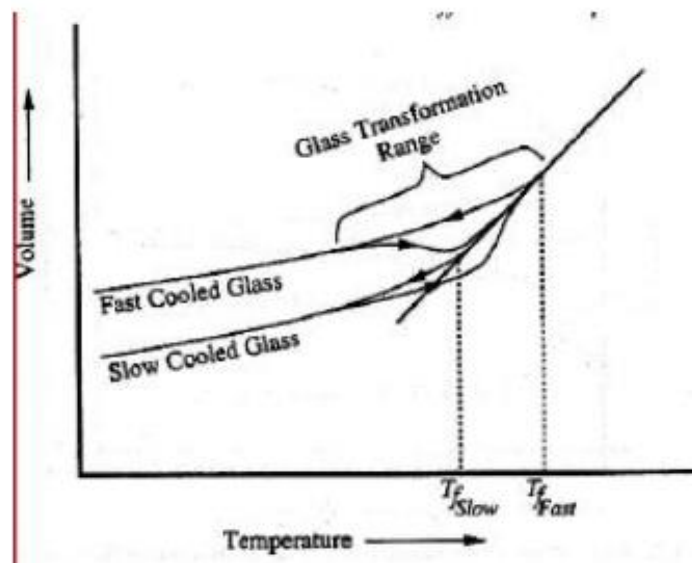


Figure 2.8: Temperature – volume curve of a glass obtained at two different cooling rates [21].

Two theories have been formulated about the glass formation [21]: structural theories and kinetic theory. A first structural theory was proposed by Zachariasen. It describes the glass structure as a three-dimensional random network where each molecule is in the form of  $AO_3$ , like into a crystalline-structured material. The disorder of the amorphous structure is represented by the modification of the A-O-A angles at the corner of each molecule, which are not equal along the same direction such as into a crystalline phase.

Following the Zachariasen theory, a generic oxide that can be described in the form  $A_mO_n$ , and it can be considered a glass former if it satisfies four rules:

- Each oxygen atoms linked to no more than two A atoms;
- Small oxygen coordination around A, such as 3 or 4;
- Polyhedra shares corners, not edge or faces;
- At least three corners are shared;

Sun enriched this structural theory considering the chemical bond strength of a compound to predict its ability to form a glass; according to this important parameter, the oxides are so distinct into three groups (*Table 2.5* and *Figure 2.9*):

- Glass networks formers (NWF), having single bond strength exceeding 80 kcal/mol, high enough to avoid the molecules arrangement into a crystalline structure; they are the main compounds of the random networks;
- Glass networks modifiers (NWM), for which the single bond strength is less than 60 kcal/mol, so not sufficient to form an amorphous structure; they break the random network through the formation of non-bridging oxygen species. These oxides can be introduced in the glass composition to modify the characteristic temperature and thermo-mechanical properties.;
- Glass intermediates, having single bond strength in the range 60-80 kcal/mol and, consequently, able to act both as modifiers or formers;

Table 2.5: Main oxides used in the glass fabrication [20]

No.	Oxide type	Characteristics	Examples
1	Main glass former oxides	Suitable structures and low crystallization rates  Form glass under slow cooling rates	SiO <sub>2</sub> B <sub>2</sub> O <sub>3</sub> GeO <sub>2</sub> P <sub>2</sub> O <sub>5</sub>
2	Conditional glass formers oxides	Form glass under certain conditions	Al <sub>2</sub> O <sub>3</sub> ; Bi <sub>2</sub> O <sub>3</sub> WO <sub>3</sub> ; MoO <sub>3</sub>
3	Intermediate oxides	Cannot form glass themselves but form glass in mixture with former oxides	TiO <sub>2</sub> ; ZnO; PbO; Zr <sub>2</sub> O <sub>3</sub>
4	Network modifier oxides	Cannot form glass themselves neither in mixture with former oxides  They can modify the properties of glass by affecting Si-O bonds	MgO CaO Na <sub>2</sub> O K <sub>2</sub> O

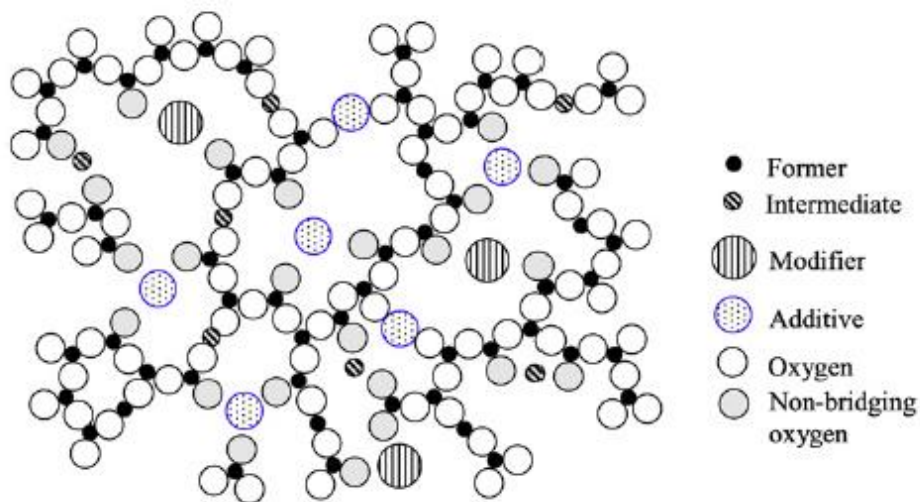


Figure 2.9: Schematic representation of a glass network structure [18].

In principle, all the liquids can be cooled into a glassy phase (regardless of their composition) if the cooling rate is high enough. The kinetic theory provides three steps for the identification of the minimum cooling rate able to bring a liquid into a solid amorphous structure, avoiding the crystallization [21]:

- Identification of the rate of nucleation rate  $I$  as function of the temperature;
- Identification of the rate crystal growth  $u$  as a function of the temperature;
- Combination of  $I$  and  $u$  to determine the volume fraction of crystallization of a mass kept at a certain temperature for a given period, using the Johnson-Mehl-Avrami equation and the T-T-T (time-temperature-transformation) diagram;

A nucleus is small agglomerate of atoms into a regular array, direct consequence of the atoms vibration and moving due to the thermal energy of the system, and it represents the first step of a crystal formation process. The number of nuclei formed per unit volume per second is called nucleation rate  $I$ , and it's evaluated as follow [21]:

$$I = nv \cdot e^{\left(\frac{-NW}{RT}\right)} \cdot e^{\left(\frac{-\Delta E_D}{RT}\right)} \quad \text{Eq. 2.1}$$

where  $n$  is the number of atoms,  $v$  is the atomic vibration frequency per second,  $N$  is the Avogadro number,  $R$  the gas constant,  $T$  the absolute temperature,  $W$  the thermodynamic barrier (net free energy change in the system after a nucleus formation) and  $\Delta E_D$  the kinetic barrier (activation energy required for an atom to cross the liquid-nucleus interface).

Once a nucleus reaches a critical size, it starts to growth by the addition of atomic layers; the rate of crystal growth  $u$  is defined as [21]:

$$u = av \cdot e^{\left(\frac{-\Delta E'}{RT}\right)} \cdot \left(1 - e^{\left(\frac{\Delta G_x}{RT}\right)}\right) \quad \text{Eq. 2.2}$$

where  $a$  is the distance between the crystal site and the liquid site,  $\Delta E'$  is the activation energy for motion and  $\Delta G_x$  is the net free energy change when the atom goes from the liquid site to the crystal site.

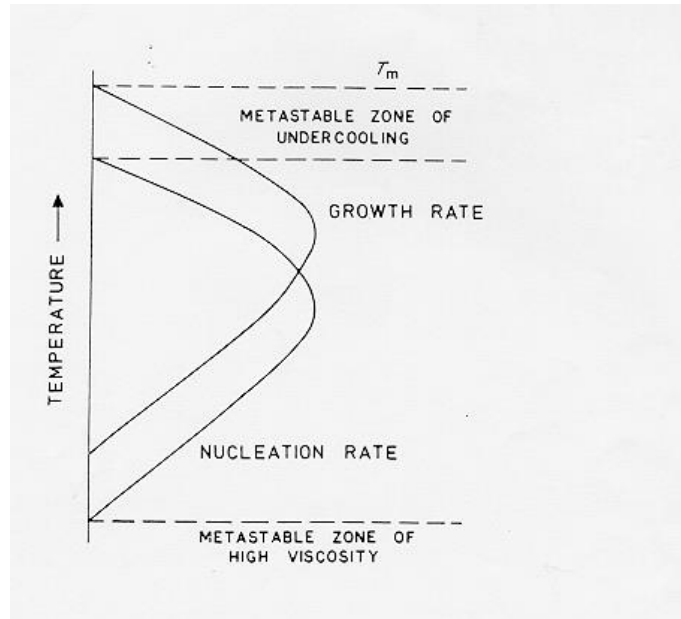


Figure 2.10: Rate of nucleation and rate of growth as a function of the temperature [21].

The region of the previous graph in *Figure 2.10* where the nucleation rate and the crystal growth rate are overlapped gives an indication about the capability of a liquid to form a crystal structure after the cooling process: the higher is the region, the higher is the probability to obtain crystals formation.

The Johnson-Mehl-Avrami equation combines the I-T curve and the u-T curve obtaining the fraction of material crystallized  $V_x$  as a function of the heat treatment time  $t$  [21]:

$$X = \frac{V_x}{V_0} = 1 - e^{\left(-\frac{\pi I u^3 t^4}{3}\right)} \cong \frac{\pi I u^3 t^4}{3} \quad \text{Eq. 2.3}$$

Remembering the functional dependence of  $I$  and  $u$  on  $T$ , and evaluating the time  $t$  needed to obtain a certain volume fraction crystallization  $X$  through an isothermal heat treatment at temperature  $T$ , it's possible to construct the T-T-T diagram (*Figure 2.11*):

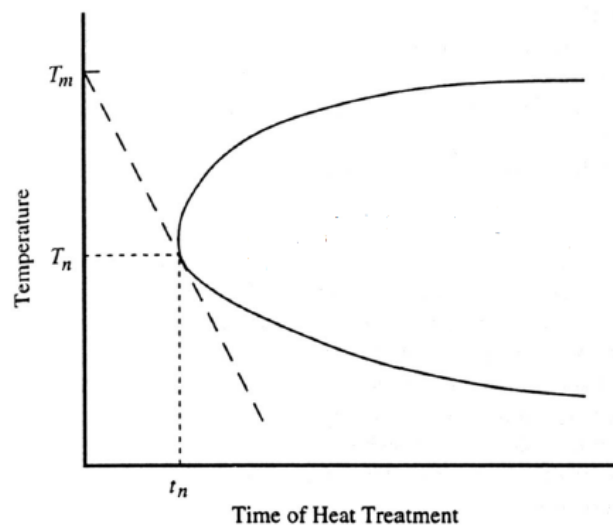


Figure 2.11: T-T-T diagram for the glass formation examination, obtained for  $X=10^{-6}$ , which represents the instrumental limit for crystals detection [21].

Finally, from the temperature-time-transformation graph (*Figure 2.11*) is possible to assert that, starting from the melting temperature  $T_m$ , the glass formation is ensured for cooling rate faster than the rate obtained by the tangent at the nose [21]:

$$\left(\frac{dT}{dt}\right)_c = \frac{T_m - T_n}{t_n} \quad \text{Eq. 2.4}$$

The state of art in the glass-based sealants proposes several glass compositions in terms of constituents adopted, each of them characterized by both advantages and disadvantages, as summarized in *Table 2.6*.

Table 2.6: Main constituents and respectively functions of glass-based sealants [18]

Glass constituent	Oxide	Function
Network former	SiO <sub>2</sub> , B <sub>2</sub> O <sub>3</sub>	Form glass network Determine $T_g$ and $T_s$ Determine thermal expansion coefficient Determine adhesion/wetting with other SOFC/SOEC components
Network modifier	Li <sub>2</sub> O, Na <sub>2</sub> O, K <sub>2</sub> O BaO, SrO, CaO, MgO	Maintain charge neutrality Create non-bridging oxygen species Modify glass properties such as $T_g$ , $T_s$ , and thermal expansion coefficient
Intermediate	Al <sub>2</sub> O <sub>3</sub> , Ga <sub>2</sub> O <sub>3</sub>	Hinder devitrification Modify glass viscosity
Additive	La <sub>2</sub> O <sub>3</sub> , Nd <sub>2</sub> O <sub>3</sub> , Y <sub>2</sub> O <sub>3</sub> ZnO, PbO NiO, CuO, CoO, MnO Cr <sub>2</sub> O <sub>3</sub> , V <sub>2</sub> O <sub>5</sub> TiO <sub>2</sub> , ZrO <sub>2</sub>	Modify glass viscosity Increase thermal expansion coefficient Improve glass flowability Improve seal glass adhesion to other cell components Induce devitrification

The most used glass formers oxides are SiO<sub>2</sub> and B<sub>2</sub>O<sub>3</sub>, which can be adopted individually or together. Silicate glasses have  $T_g$  in the range 675-725 °C and  $T_s$  in the range 725-750 °C; on the contrary, borate glasses have smaller  $T_g$  temperatures range (575-590 °C) [18]. In the borosilicate glasses  $T_g$  and  $T_s$  depend on the B<sub>2</sub>O<sub>3</sub>, because an increment of its molar fraction involves the viscosity and network rigidity decrement, which follows the lowering of both the temperatures. *Figure 2.12* and *Figure 2.13* explain the  $T_g$  and  $T_s$  dependence on the B<sub>2</sub>O<sub>3</sub>/SiO<sub>2</sub> ratio for some borosilicate glasses.

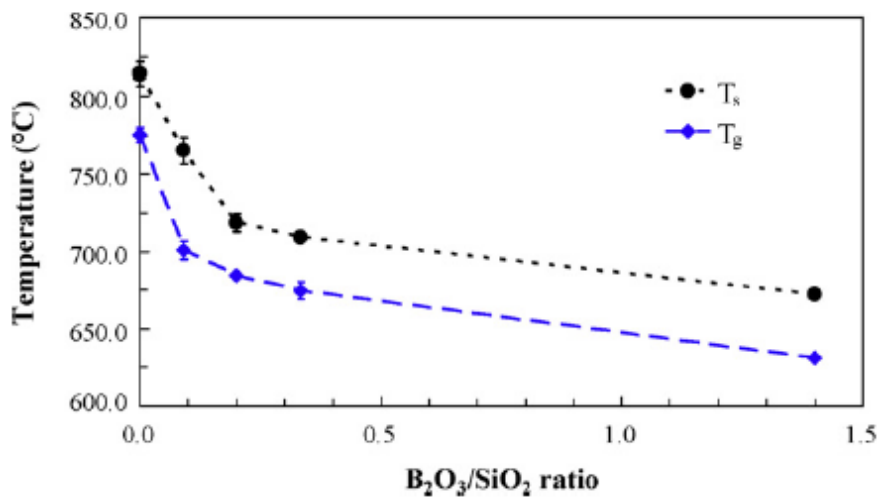


Figure 2.12:  $T_g$  and  $T_s$  of a borosilicate glass as a function of the ratio B<sub>2</sub>O<sub>3</sub>/SiO<sub>2</sub> [18].

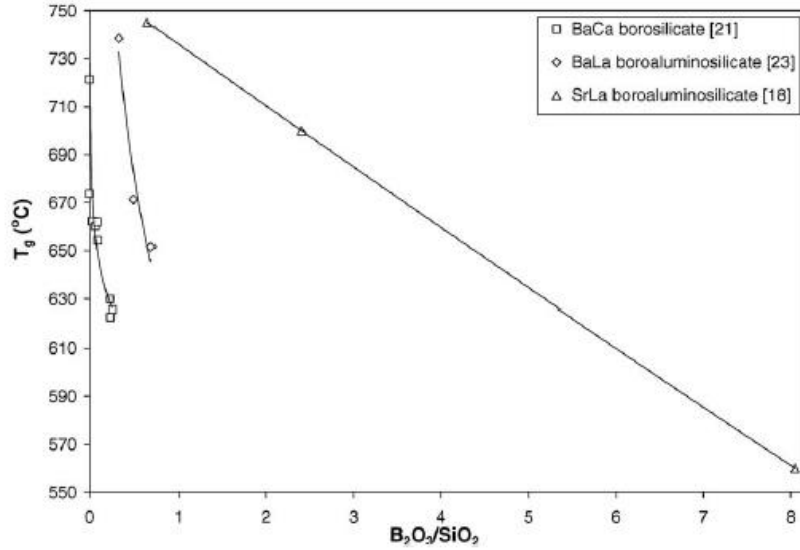


Figure 2.13:  $T_g$  of some borosilicate glasses as a function of the ratio  $B_2O_3/SiO_2$  [14].

The introduction of glass modifiers reduces  $T_g$  and  $T_s$  because of the formation of non-bridging oxygens in the structure which lower the continuity degree of the network. This is not strictly true for borosilicate and borate glasses, where the presence of  $B_2O_3$  involves some anomalies, known as “boron anomalies” [18], for which an initially addition of modifiers can bring to a  $T_g$  and  $T_s$  increment, because of the decrement of non-bridging-oxygen ions. The impact that a modifier could have on the characteristic temperatures of a glass depends on its field strength, namely the capability of modifier cations to bond with the oxygen. Alkaline oxides ( $Na_2O$ ,  $K_2O$  and  $Li_2O$ ) have a field strength smaller than that of alkaline earth oxides ( $CaO$ ,  $SrO$ ,  $MgO$ ,  $BaO$ ), so their ions are more mobile and, consequently, they lead to higher  $T_g$  and  $T_s$  than those of alkaline earth containing glasses [18]. The glass intermediates have lower impact on the  $T_g$  and  $T_s$ ; the  $Al_2O_3$ , which is the most common intermediate for SOFC/SOEC glass sealants, acts as a glass network former when the coordination number of the  $Al^{3+}$  is four, increasing  $T_g$  and  $T_s$ , and as modifier when the coordination number of the  $Al^{3+}$  is five or six, decreasing  $T_g$  and  $T_s$ . Further compounds may be added to the glass structure known as additives. For example, they can be nucleating agents, such as rare earth metal oxides ( $La_2O_3$ ) or transition metal oxides ( $ZrO_2$ ,  $TiO_2$ ,  $NiO$ ,  $ZnO$  and  $Y_2O_3$ ) used to further tailor the  $T_g$  and the  $T_s$  of a glass. The most used additive is the  $La_2O_3$  in quantities smaller than 10 mol%, whose addition involves an increment of  $T_g$  and  $T_s$  higher than that of transition metal oxides, which have negligible effects. Additive can be used also to tune the viscosity of the glass, modify its CTE and its adhesion to other component in the case of sealants.

As said, the glass composition defines also the glass CTE (Coefficient of Thermal Expansion) value, which is expected to be in the range  $9-12 \cdot 10^{-6} \text{ } ^\circ\text{C}^{-1}$  for SOCs sealing applications; outside this range, the CTE mismatch with that of the joined components produces thermo-mechanical stresses which could lead to the sealing failure. The tensile ( $\alpha_G < \alpha_C$ ) or compressive ( $\alpha_G > \alpha_C$ ) stress  $\sigma$  involved at the glass/adjacent component interfaces due to CTE mismatch can be expressed as follow [18]:

$$\sigma = CE \cdot \int_{T_Q}^{T_R} (\alpha_G - \alpha_C) dT \quad \text{Eq. 2.5}$$

where  $C$  is a geometrical constant,  $E$  is the glass Young's module,  $\alpha_G$  and  $\alpha_C$  the glass and the component CTEs respectively,  $T_R$  is the room temperature and  $T_Q$  the glass set point temperature; the CTEs of a common rSOC components are  $10.5 \cdot 10^{-6} \text{ K}^{-1}$  for the electrolyte,  $12.4 \cdot 10^{-6} \text{ K}^{-1}$  for the cathode,  $10\text{--}14 \cdot 10^{-6} \text{ K}^{-1}$  for the anode and  $11.0\text{--}15 \cdot 10^{-6} \text{ K}^{-1}$  for the interconnect [19]. Due to its higher symmetry, pure silica has a CTE of  $0.6 \cdot 10^{-6} \text{ }^\circ\text{C}^{-1}$ , much lower of that of the  $\text{B}_2\text{O}_3$  ( $14.4 \cdot 10^{-6} \text{ }^\circ\text{C}^{-1}$ ). So, considering a borosilicate glass, its CTE could be tuned by set a proper  $\text{B}_2\text{O}_3/\text{SiO}_2$  ratio, as shown in *Figure 2.14* and *Figure 2.15*.

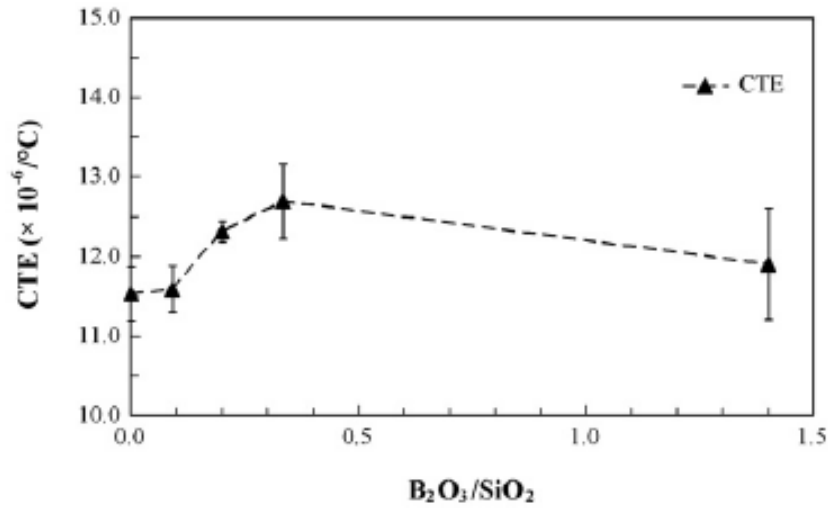


Figure 2.14: CTE variation of a  $\text{B}_2\text{O}_3\text{-SiO}_2\text{-SrO-AlO}_3\text{-La}_2\text{O}_3$  glass as a function of the  $\text{B}_2\text{O}_3/\text{SiO}_2$  ratio [18].

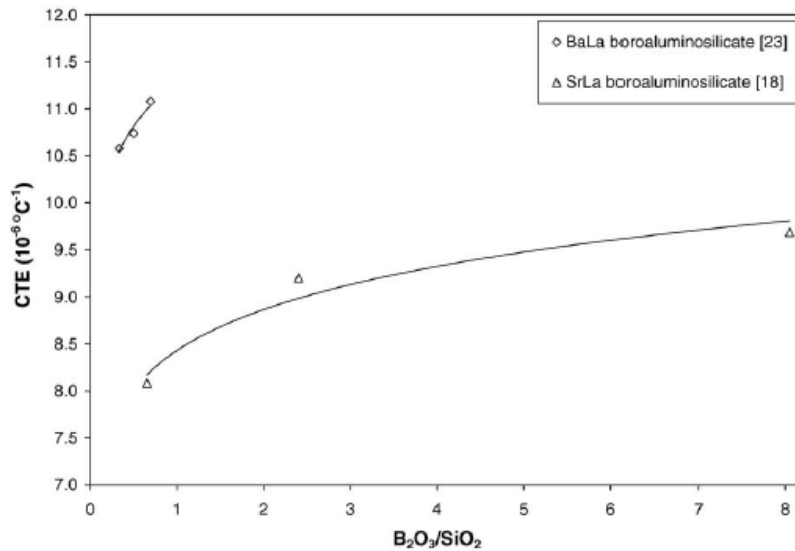


Figure 2.15: CTE variation of silicate glasses as a function of the ratio  $\text{B}_2\text{O}_3/\text{SiO}_2$  [14].

Like for the  $T_g$  and the  $T_s$ , the effect of the modifiers on the CTE depends on their quantity and field strength; in particular, the CTE increases with the increasing of the modifiers quantity and the decreases with field strength of the modifiers ions. An example is given in the *Figure 2.16* [18], where the CTE has been tuned by acting on the BaO content.

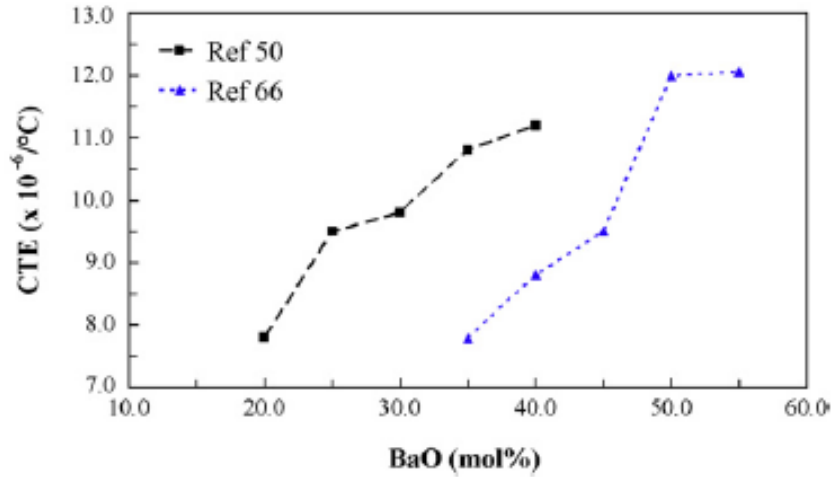


Figure 2.16: CTE variation of borosilicate glasses as a function of the BaO content in two different references [18].

The alumina acting as network former increases the symmetry of the structure, lowering the CTE; on the contrary, it's impossible to identify a precise effect of the additives on the CTE value.

By its nature a glass is a non-equilibrium structure, for this is possible to induce a crystallization (devitrification) by carrying out suitable thermal treatments. In this case the resulting material is classified as a glass-ceramic, a class of materials constituted in general by a residual glassy phase (still amorphous) and by one or more crystalline phases resulted by the devitrification process. It is possible to modify the starting composition of the parent glass in order to tailor the nature and the amount of the crystallized phases. This strategy is effective in order to modify the overall properties of the material such as the CTE inducing the crystallization of suitable crystalline phases.

The main crystalline phases and their own CTE values are listed in the *Table 2.7* and *Table 2.8*:

Table 2.7: CTE of different devitrified phases [18]

Devitrified phases	Formula	CTE ( $\times 10^{-6} \text{ } ^\circ\text{C}^{-1}$ )
Quartz	SiO <sub>2</sub>	11.2–23.3
Enstatite	MgSiO <sub>3</sub>	9.0–12.0
Clinoenstatite	MgSiO <sub>3</sub>	7.8–13.5
Protoenstatite	MgSiO <sub>3</sub>	9.8
Forsterite	Mg <sub>2</sub> SiO <sub>4</sub>	9.4
Wollastonite	CaSiO <sub>3</sub>	9.4
Calcium orthosilicate	Ca <sub>2</sub> SiO <sub>4</sub>	10.8–14.4
Barium silicate	BaSiO <sub>3</sub>	10.5–12.5
	Ba <sub>2</sub> Si <sub>3</sub> O <sub>8</sub>	12.6
Barium borate	BaB <sub>2</sub> O <sub>4</sub>	$\alpha_a = 4.0$ $\alpha_c = 36.0$
Barium zirconate	BaZrO <sub>3</sub>	7.9
Hexacelsian	BaAl <sub>2</sub> Si <sub>2</sub> O <sub>8</sub>	6.6–8.0
Monocelsian	BaAl <sub>2</sub> Si <sub>2</sub> O <sub>8</sub>	2.3
Orthorhombic celsian	BaAl <sub>2</sub> Si <sub>2</sub> O <sub>8</sub>	4.5–7.1
Hexacelsian	SrAl <sub>2</sub> Si <sub>2</sub> O <sub>8</sub>	7.5–11.1
Monocelsian	SrAl <sub>2</sub> Si <sub>2</sub> O <sub>8</sub>	2.7
Orthorhombic celsian	SrAl <sub>2</sub> Si <sub>2</sub> O <sub>8</sub>	5.4–7.6
Cordierite	Mg <sub>2</sub> Al <sub>4</sub> Si <sub>5</sub> O <sub>18</sub>	2.0

Table 2.8: Coefficients of thermal expansion of crystalline phases characteristic of alkaline-earth containing glass-ceramics [14]

System	Phase	CTE ( $^{\circ}\text{C}^{-1} \times 10^6$ )
Mg-Si-O	Enstatite ( $\text{MgSiO}_3$ )	7-9
Ca-Si-O	Wollastonite ( $\text{CaSiO}_3$ )	4-9
	Calcium orthosilicate ( $\text{Ca}_2\text{SiO}_4$ )	10-14
Ba-Si-O	Barium silicate ( $\text{BaSiO}_3$ )	9-13
	Barium orthosilicate ( $\text{BaSi}_2\text{O}_5$ )	14
Ba-Ca-Si-O	Barium calcium orthosilicate ( $\text{Ba}_3\text{CaSi}_2\text{O}_8$ )	12-14
Mg-Al-Si-O	Cordierite ( $\text{Mg}_2\text{Al}_4\text{Si}_5\text{O}_{18}$ )	1
Sr-Al-Si-O	Hexacelsian ( $\text{SrAl}_2\text{Si}_2\text{O}_8$ )	8-11
	Monocelsian ( $\text{SrAl}_2\text{Si}_2\text{O}_8$ )	3
	Orthocelsian ( $\text{SrAl}_2\text{Si}_2\text{O}_8$ )	5-8
Ba-Al-Si-O	Hexacelsian ( $\text{BaAl}_2\text{Si}_2\text{O}_8$ )	7-8
	Monocelsian ( $\text{BaAl}_2\text{Si}_2\text{O}_8$ )	2-3
	Orthocelsian ( $\text{BaAl}_2\text{Si}_2\text{O}_8$ )	5-7

Many studies [14, 18, 19, 23, 24] have focused on different system of glass-ceramic sealants in order to find suitable solution depending on the stack design and operating conditions. Many of them shown the crystallization of one or more of the following phases:

- Cristobalite( $\text{SiO}_2$ ), formed in the silicate and borosilicate glass-ceramics. It's an undesired compound because of its strong volume change due to its polymorphic transformation during the cooling-down processes, that can induce cracks formation;
- Barium silicate ( $\text{BaSiO}_3$ ) and orthosilicate, formed in the barium-containing glass-ceramics, which leads to an overall CTE increment due to its large coefficient of thermal expansion;
- Celsian ( $\text{BaAl}_2\text{Si}_2\text{O}_8$ ), can crystallize in barium aluminosilicate glass-ceramics. Celsian can show two polymorphic structures with very different coefficients of thermal expansion: hexacelsian, with a CTE slightly higher than that desired for a rSOC sealant, and monocelsian, with a CTE considerable lower. In case of presence of strontium in the initial composition, the celsian crystals can contain a solid solution of Sr and Ba which stabilize the monocelsian form;
- Barium calcium orthosilicate ( $\text{Ba}_3\text{CaSi}_2\text{O}_8$ ), formed in the barium aluminosilicate glasses, which increases the overall glass-ceramic CTE;
- Wollastonite and/or anorthite ( $\text{CaSiO}_3$  and  $\text{CaAl}_2\text{Si}_2\text{O}_8$ ), formed in Ba-freealuminosilicate glass-ceramics;
- Enstatite ( $\text{MgSiO}_3$ ), can be formed in case Mg is added to the glass composition.

Both thermodynamic and kinetic parameters are taken into account in the devitrification process: onset devitrification temperature  $T_x$  and crystallization peak temperature  $T_p$ ,  $T_g$ ,  $T_m$  and activation energy for crystallization. In silicate glasses the  $\text{SiO}_2$  addition increases the  $T_x$  because of a high glass network connectivity, as reported in *Figure 2.17*; on the contrary, the addition of  $\text{B}_2\text{O}_3$  in borosilicate glasses has shown a contrasting trend, depending on the composition involved (*Figure 2.18* and *Figure 2.19*) [18]. High field strength modifiers increase the devitrification temperatures, enhancing the thermal stability; the same occurs for glass containing less than 10 mol% of  $\text{Al}_2\text{O}_3$ , which in these quantities acts as network former homogenising the structure and avoiding phase separation and devitrification.

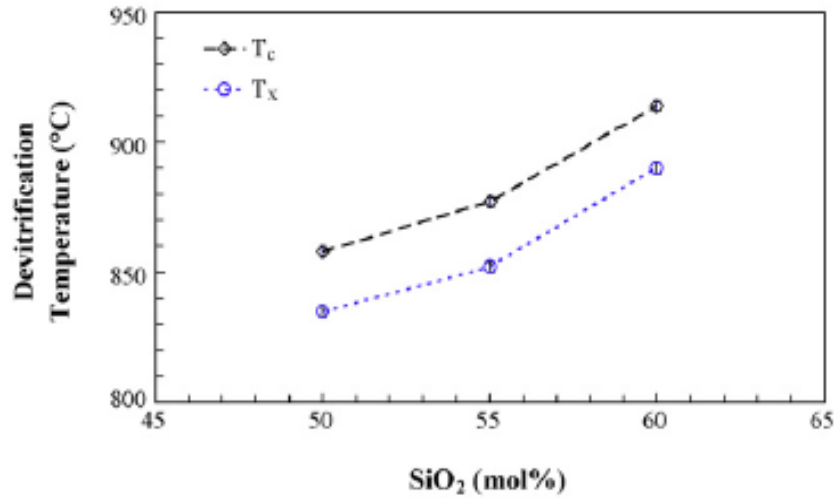


Figure 2.17: Devitrification temperatures as a function of the SiO<sub>2</sub> content in a SiO<sub>2</sub>-MgO-BaO glass [18].

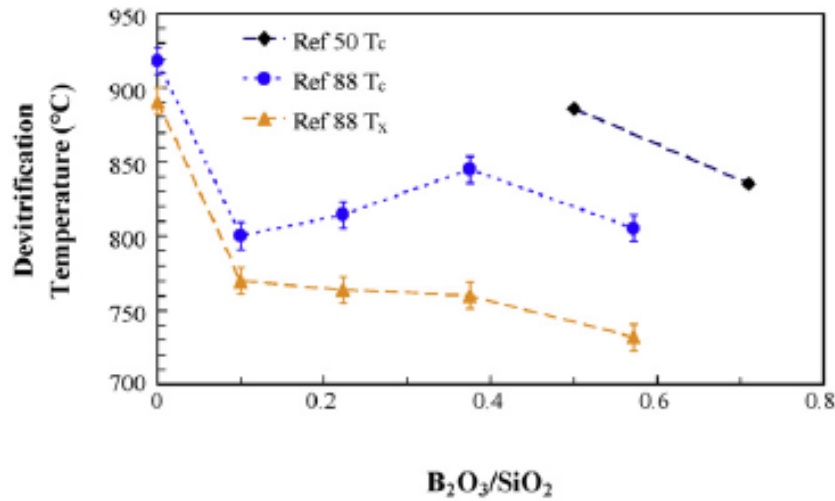


Figure 2.18: Devitrification temperatures as a function of the B<sub>2</sub>O<sub>3</sub>/SiO<sub>2</sub> ratio in a SiO<sub>2</sub>-B<sub>2</sub>O<sub>3</sub>-MgO-BaO glass (88) and SiO<sub>2</sub>-B<sub>2</sub>O<sub>3</sub>-MgO-BaO-Al<sub>2</sub>O<sub>3</sub> glass (50) [18].

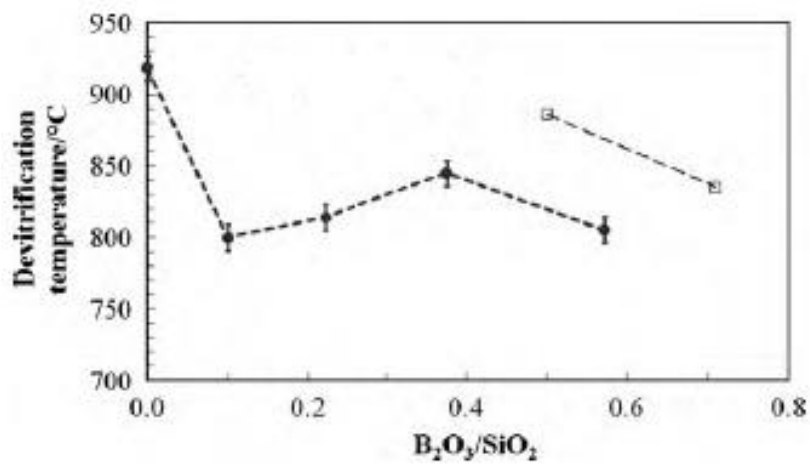


Figure 2.19: Devitrification temperatures as a function of the ratio B<sub>2</sub>O<sub>3</sub>/SiO<sub>2</sub> in borosilicate earth alkaline oxides-containing glasses [19].

The crystallization is a kinetic process, and each system has its own kinetic behaviour according to its activation energy; therefore, the devitrification thermal treatment has to be properly selected in order to control the sintering and the crystallization of the system. The correct understanding of crystallization mechanisms and characteristic temperatures needs to be assessed in order to design an optima sinter-crystallization treatment. Indeed, the crystallization can hinder the sintering process which is crucial to obtain a well densified glass-ceramic sealant. In general, is desirable a complete sintering by viscous flow before the crystallization, this would allow the glass to wet and bond the adjacent components before the devitrification and an effective densification. In a second stage a suitable treatment would allow the formation of an adequate percentage of crystalline phases. The kinetic of the crystallization process can be properly modified through the addition of nucleating agents, such as Ni, Cr<sub>2</sub>O<sub>3</sub>, TiO<sub>2</sub> and ZrO<sub>2</sub>, which are able to reduce the energy of activation functionally to their electronegativity, as shown in *Figure 2.20*.

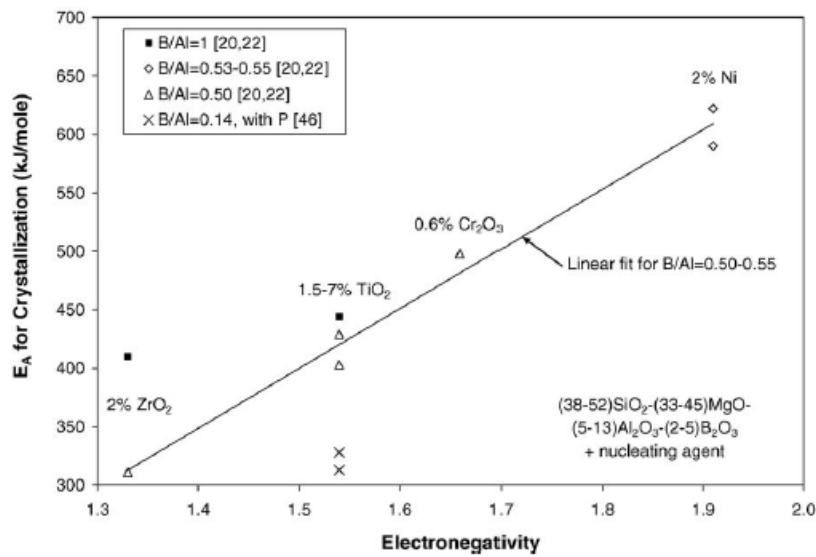


Figure 2.20: Activation energy of crystallization of a glass containing different nucleating agents [14].

The activation energy for the crystallization can be estimated starting from the definition of crystallization peak temperature  $T_p$ , namely the temperature at which the crystallization process occurs. The  $T_p$  can be experimentally detected through DTA (differential Thermal Analysis), an analysis conducted on glass powders of different sizes, which are obtained from the glass grinding and sieving; the powders are placed in a crucible and heated-up with controlled heating rates. The DTA can measure the temperature differences between the glass powders and a reference, such as the Al<sub>2</sub>O<sub>3</sub>. In this way it is possible to understand the temperatures corresponding to thermal events, endothermic or esothermic.

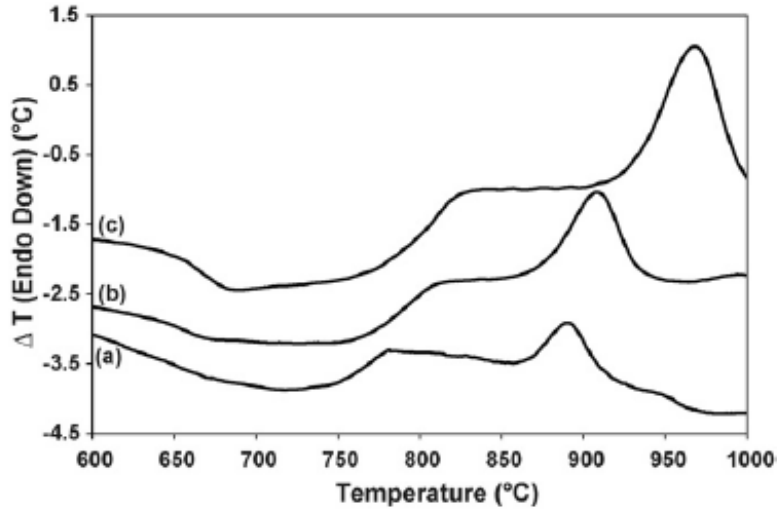


Figure 2.21: DTA of glass powders ( $38 < d < 75 \mu\text{m}$ ) obtained at different heating rate:  $5^\circ\text{C}/\text{min}$  (a),  $10^\circ\text{C}/\text{min}$  (b),  $25^\circ\text{C}/\text{min}$  (c) [24].

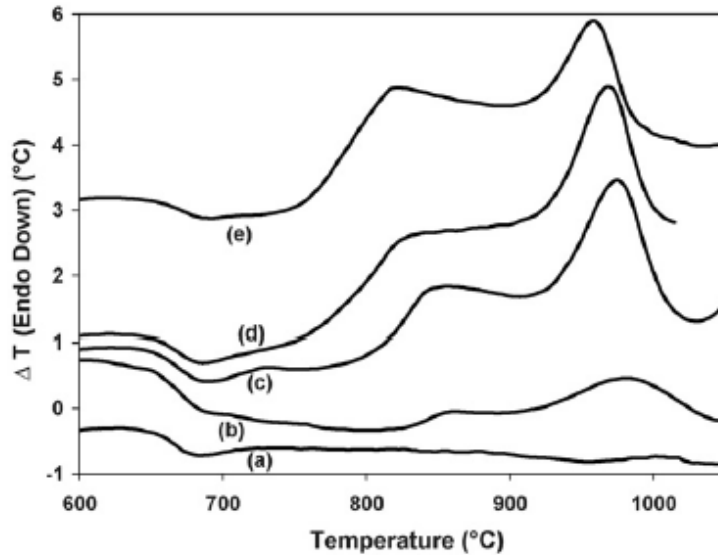


Figure 2.22: DTA of glass powders of different sizes (heating rate  $25^\circ\text{C}/\text{min}$ ): bulk glass (a),  $d > 106 \mu\text{m}$  (b),  $75 < d < 106 \mu\text{m}$  (c),  $38 < d < 75 \mu\text{m}$  (d),  $d < 38 \mu\text{m}$  (e) [24].

From the DTA curve, such as in *Figure 2.21* and *Figure 2.22*, is possible to extract two main glass thermal properties: the glass transition temperature  $T_g$  and the peak temperature  $T_p$ . The experiences have shown that the peak temperature is directly affected by both the particle size and the heating rate; in the specific,  $T_p$  shifts to higher values when the heating rate or the particle size are increased.

The Kissinger equation relates the activation energy for the crystallization  $E_{ck}$  with the peak temperature [23]:

$$\ln\left(\frac{\alpha}{T_p^2}\right) = -\frac{E_{ck}}{RT_p} + const \quad \text{Eq. 2.6}$$

where  $\alpha$  is the heating rate and  $R$  is the gas constant. The Kissinger equation can be applied to crystallization processes occurring completely from the surface sites; if not, Matusita and Sakka equation has to be used [23]:

$$\ln\left(\frac{\alpha^n}{T_P^2}\right) = -\frac{mE_{ck}}{RT_P} + \text{const} \quad \text{Eq. 2.7}$$

where  $n$  is the Avrami coefficient and  $m$  is the growth of dimensionality of the crystalline phase; the Avrami coefficient  $n$  can be estimated using the Ozawa equation [23]:

$$-n = \left(\frac{d\{\ln[-\ln(1-\chi)]\}}{d(\ln\alpha)}\right)_T \quad \text{Eq. 2.8}$$

where  $\chi$  is the volume fraction of the crystallized phase at given temperature  $T$ , estimated from the DTA graph as the ratio of the partial area under the peak to the total area of the peak.

A rSOC sealant is in contact with both oxidizing and reducing atmosphere and with different materials, so a high chemical stability at high temperatures is required to this component to avoid detrimental interactions. Two main chemical degradation phenomena can occur during the operating life of a glass-based sealant: vaporization of the glass constituents and chemical interactions of the glass with the cell components in both the atmospheres. The vaporization of glass compounds can result in variation in its overall composition (and as a consequence in its properties).  $B_2O_3$  can vaporize into gaseous species in presence of  $H_2O$  in the atmosphere. It can be vaporized as  $H_3BO_3$  or alkaline methaborates (in case also alkaline oxides are present in the glass). In some cases, also silica can react with hydrogen and water at temperature around  $1000\text{ }^\circ\text{C}$  producing  $SiO$  and  $Si(OH)_4$  (volatile). The volatility of these oxides can easily lead to the glassy network degradation, changes in characteristic temperatures and CTE.

Several research activities [18, 19, 20] have investigated the chemical interaction of the glass sealants at the interface with the interconnect, the electrolyte and the electrodes. Among this the most challenging coupling of a glass-ceramic sealant is with the metallic materials typically used as interconnects. The most common interconnect materials used up to now are ferritic stainless steels containing different percentage of Cr (i.e. Crofer 22 APU or AISI 441), and they represent the most critical components in terms of chemical interactions with the glass sealant when they are exposed to a dual atmosphere at high temperatures. For example, alkaline oxides showed a strong tendency to form chromates reacting with Cr from the interconnects (e.g.  $Na_2CrO_4$ ,  $K_2CrO_4$ ). These compounds are volatile in the typical operating conditions of a rSOC stack, and this may be translated in the destabilization of the glass network, in the acceleration of the chromium vaporization and in the cathode poisoning. Nowadays the adoption of coating layers and the peroxidation of the interconnector surfaces represent a valid solution against the chemical interaction between the glass sealant and the interconnect; moreover, chemical stability is enhanced by identifying a proper glass composition, free of alkaline oxides and with a content of  $B_2O_2$  as low as possible.

The interfaces of the seal glass with the other cell components are sensitive regions due to the development of strain produced on them by the thermal cycling; two types of strains can be considered:

- the thermal strain, function of the CTEs mismatch between glass and adjacent component and the temperature drop;
- the mechanical strain, function of the elastic moduli, shear moduli and Poisson's ratios of the glass and the adjacent component.

Also in this case, the glass/interconnect interfaces are the most critical regions, especially during the system cooling-down. The failures involved by thermomechanical strains are represented by the presence of cracks (opened or sliding) or delamination, and they can be avoided by the selection of a glass composition which ensures a CTE mismatch and an elastic module mismatch with adjacent components as lower as possible.

The glass sealant must also avoid the electrical connection between the joined components, so high electrical resistivity values are required. Resistivity values higher than  $10^4 \Omega \text{ cm}$  are necessary to avoid current shunting [19]. Due to the boron anomaly which decreases the non-bridging oxygen species when modifiers are initially added, borate glasses have an electrical resistivity higher than silicate glasses, when both the systems contain modifiers (e.g.  $10^{11.4} \Omega \text{ cm}$  for  $15\text{Na}_2\text{O}-15\text{BaO}-70\text{SiO}_2$  and  $10^{12.5} \Omega$  for  $15\text{Na}_2\text{O}-15\text{BaO}-60\text{SiO}_2-10\text{B}_2\text{O}_3$ ). Modifiers with higher ionic radius increase the resistivity because of their lower ionic mobility; under this point of view, alkaline earth oxides have a better behaviour than the alkaline oxides. Generally, an increasing in the content of modifiers leads to a reduction of the electrical resistivity due to the production of non-bridging oxygen ions. A reduction in the electrical resistivity value occurs also with the addition of the intermediates oxides above a certain amount, because of the enhancement of the modifiers ions mobility. Electrical resistivity and ions mobility are strictly dependent, and they are both function of the temperature according to the Arrhenius equation (for  $T < T_g$ ) and the Vogel–Tammann–Fulchar equation ( $T > T_g$ ) [19]:

$$\rho = \frac{T}{A} e^{\left(\frac{E}{kT}\right)} \quad \text{for } T < T_g \quad \text{Eq. 2.9}$$

$$\rho = \frac{T}{A'} e^{\left(\frac{B}{T-T_0}\right)} \quad \text{for } T > T_g \quad \text{Eq. 2.10}$$

where T is temperature, A is pre-exponential terms, k is the Boltzmann constant, E is the activation energy for ionic mobility and A', B and T<sub>0</sub> are the system specific constants. The temperature increment enhances the ionic mobility and, as a consequence, reduce the electrical resistivity.

The last requirement for a rSOC glass sealant is the gas tightness, expected to be less than 1% of the total entering fuels to avoid reactants mixing and leakages [19]. The main causes of leakages are cracks and pores, generally produced by thermomechanical stresses involved at the interfaces, in presence of devitrified species or during the system cool-down.

According to what has been said so far, silicate or borosilicate glasses, avoiding the B<sub>2</sub>O<sub>3</sub> as unique network former, are commonly used as glass-based sealants for rSOCs. Alkaline earth oxides with lower field strength ions (such as CaO, BaO and SrO) should be preferred as network modifiers to alkaline oxides and alkaline earth oxides with higher field strengths. *Table 2.9* reports some glass and glass-ceramic common compositions.

Table 2.9: Some glass and glass-ceramic sealants compositions and main thermal properties [14]

Composition (mole%)					Properties		
SiO <sub>2</sub>	B <sub>2</sub> O <sub>3</sub>	Al <sub>2</sub> O <sub>3</sub>	Alkaline-earth		Other	T <sub>g</sub> (°C)	CTE (°C <sup>-1</sup> × 10 <sup>6</sup> )
			BaO/SrO	CaO/MgO			
<b>Boroaluminosilicates</b>							
30	15	10	40 BaO		5 La <sub>2</sub> O <sub>3</sub>	667	11.2
38	13	10	35 BaO		5 La <sub>2</sub> O <sub>3</sub>	739	10.6
33	17	10	35 BaO		5 La <sub>2</sub> O <sub>3</sub>	670	10.8
29	21	10	35 BaO		5 La <sub>2</sub> O <sub>3</sub>	652	11.1
33	17	10	35 BaO		5 La <sub>2</sub> O <sub>3</sub>	656	11.1
30	22	10	36 BaO		2 ZrO <sub>2</sub>	614	10.6
34	17	10	36 BaO		2 NiO	617	11.5
<b>Borosilicates</b>							
32	2	0	40 BaO	10 CaO	16 unspecified	660	10.7
33	3	0	40 BaO	10 CaO	14 unspecified	662	10.5
31	8	0	38 BaO	15 CaO	8 unspecified	626	11.3
34	8	0	42 BaO	8 CaO	8 unspecified	623	10.8
30	7	0	37 BaO	16 CaO	10 unspecified	630	11.4
<b>Aluminosilicate</b>							
50	0	5	45 BaO			730	10.7
<b>Silicates</b>							
35	0	0	44 BaO	11 CaO	10 unspecified	721	10.6
50	0	0	40 BaO	10 MgO		686	12.0
50	0	0	40 BaO		10 ZnO	676	10.7
<b>Borate</b>							
8	40	7	25 SrO		20 La <sub>2</sub> O <sub>3</sub>	760	11.5

### 3. Thermal characterization of glass-ceramic sealants

A glass-ceramic material is obtained from the partial devitrification of a glass. The following sections will describe how different glass-ceramic materials have been obtained and characterized together with their behaviour as sealants for rSOC technologies. The present work focused on two main systems on the basis of the parent glass compositions: Ba-based and Sr-base, respectively containing Ba and Sr as main network modifiers. In particular, six different systems labelled as shown in *Table 3.1* were designed, produced, characterized and tested:

Table 3.1: Systems composition and labelling.

	Sr-based		Ba-based			
Oxides (mol%)	HJ14	GS7	HJ11	HJ26	HJ27	HJ28
SiO <sub>2</sub>	48-53	45-50	50-60	50-60	50-60	55-65
CaO	8-10	8-10	5-10	5-10	5-10	5-10
Al <sub>2</sub> O <sub>3</sub>	1-3	3-5	2-6	2-5	1-3	2-5
B <sub>2</sub> O <sub>3</sub>	5-10	5-10	5-10	5-10	5-10	5-10
BaO	/	/	25-30	25-30	25-30	20-25
SrO	30-35	30-35	/	/	/	/
Y <sub>2</sub> O <sub>3</sub>	/	/	/	/	/	1
Ga <sub>2</sub> O <sub>3</sub>	/	1-5	/	1-3	2-5	/

SiO<sub>2</sub>, Al<sub>2</sub>O<sub>3</sub>, Y<sub>2</sub>O<sub>3</sub> and G<sub>2</sub>O<sub>3</sub> were weighted as pure materials, while CaO, B<sub>2</sub>O<sub>3</sub>, BaO and SrO were introduced in the compositions starting from CaCO<sub>3</sub>, H<sub>3</sub>BO<sub>3</sub>, BaCO<sub>3</sub> and SrCO<sub>3</sub> respectively. Once the chemicals were weighted and mixed, the powders were melted in a platinum-rhodium crucible into a furnace for 1h at 1600 °C. The melt was then cast on a brass plate to obtain the glass in form of bulk. From the melted, glass in the form of a bulk piece was selected for dilatometry test after a proper preparation in order to obtain a cylinder like sample with a thickness around 5mm. The remaining glass was grounded and sieved to obtain powders smaller than 25 µm. The powders were used to produce glass-ceramic pellets, after the selected joining thermal treatment. In addition, Crofer22APU/glass-ceramic/Crofer22APU and Crofer22APU/glass-ceramic/3YSZ joined samples were produced. For all the investigated systems the chosen joining thermal treatment was 950°C for 1h and 850°C for 2h at 2°C/min, to allow the glass to partially crystallize and effectively sinter, then wetting and bonding the Crofer plates surfaces. The joining treatment was chosen on the basis of the results of thermal characterization.

The complete thermal characterization of each composition was carried out through the following tests:

- *Differential Thermal Analysis (DTA)*

The differential thermal analysis is performed on the glass powders to obtain glass transition temperature  $T_g$ , the onset of the crystallization temperature  $T_x$  and the crystallization peak temperature  $T_p$  of each composition. The device is composed by two platinum crucibles, one for the sample powders and one for the reference, consisting of alumina. A thermocouple measures the temperature of both the crucibles while the system is heated up to a set temperature and with a defined heating rate. At the end of the test, a graph with the crucibles temperature difference as a function of the sample temperature is obtained. For a typical glass it is possible to identify four characteristic points: an inflection point (glass transition temperature,  $T_g$ ), an onset (crystallization temperature,  $T_x$ ) a maximum point (crystallization peak temperature,  $T_p$ ) and a minimum point (melting temperature,  $T_m$ ). In our case, the DTAs were performed on almost 100g of glass powders heated up to 1300 °C at 5 °C/min.

- *Dilatometry*

The dilatometry is a thermo-mechanical analysis which aims to evaluate the coefficient of thermal expansion (CTE) and the softening temperature ( $T_s$ ) of as-casted glasses or the CTE of glass-ceramic samples, both as-joined or aged in different conditions. In this way it is possible to understand how this parameter could change during the working life of a sealant. The instrument is equipped with a furnace to heat up the sample; during a controlled heating, the relative thickness is continuously measured as a function of temperature to determine the CTE, according to the following relation:

$$\frac{\Delta L}{L_0} = CTE \cdot \Delta T \quad \text{Eq. 3.1}$$

In the present work, the dilatometry tests were performed on three kinds of samples: as-casted glasses, as joined glass-ceramics and aged glass-ceramics. For a glass, a linear trend is expected until a peak is reached; the temperature corresponding to the peak represents the glass softening temperature. On the contrary, for a glass-ceramic a linear trend is expected. The presence possible of variations from the linear trend suggests that a consistent residual amorphous phase is still present in the glass-ceramic system. The CTEs were estimated as the angular coefficient of the dilatometry curve in the range 200-500 °C; these temperatures are considered the most critical for the heating up and cooling down of a SOCs stack. During the tests, samples of almost 5 mm of thickness were tested with a heating rate of 5°C/min.

- *Heating Stage Microscopy (HSM)*

Heating Stage Microscopy is used to study the sintering and wetting behaviour of a powder compact during a controlled thermal treatment. In general, a heating stage microscopy is composed by a furnace (which heats up the sample with a defined thermal program) and a camera (which produces detailed images of the sample shape changes during the thermal treatment). The shrinkage is measured as a function of temperature during all the test. The most interesting points on the curve are the temperature of first shrinkage ( $T_{FS}$ ), which detects the initiating of the sintering process, and the temperature

of maximum shrinkage ( $T_{MS}$ ), which detects the end of the sintering process. A constant shrinkage above the  $T_{MS}$  suggests that the glass has a refractory nature; otherwise, a subsequent decrement of the shrinkage means that the glass has still a consistent amorphous residual phase which leads to a strong flowing behaviour.

- *Scanning Electrons Microscope (SEM) and Electron Dispersive X-ray Spectroscopy (EDS)*

The Scanning Electron Microscope is a device able to produce detailed images at high magnification of the surface of a sample, thanks to its interaction with an electron beam properly focused. The images are produced by the detection of the secondary electrons emitted by the sample atoms after their interaction with the electrons beam, showing the morphology of the scanned surfaces. In this case morphological information will be collected. It is possible also to collect the backscattered electron from the surface to have a compositional contrast (heavier will be the atoms that back-scatter the electrons, brighter will appear the phase in the image). A second detector can be used to perform the EDS (Energy Dispersive X-ray Spectrometry); this is a chemical investigation which allows the identification and quantification of the chemical elements present in the investigated region, aiming to have a first characterization about the chemical species involved. Differently from a SEM, the EDS detects the X-ray emitted by the sample atoms after the interaction with the incident electrons; the atoms of each chemical element have their own emission wave length which can be properly detected. SEM and EDS have been performed on the Crofer22APU/glass-ceramic/Crofer22PAU and Crofer22APU/glass-ceramic/3YSZ joined samples after the joining treatment and the aging tests, aiming to identify the presence of pores, cracks, interaction between the joined materials, wettability of the joined surfaces, phases and chemical elements involved, in order to assess the compatibility of the joined materials.

- *X-Ray Powder Diffraction (XRD)*

The XRD analysis allows the identification of the different crystalline phases formed in the glass-ceramic powders after the joining process or after the aging test. The device is able to produce X-rays beams with proper direction and wavelength which hit the powders; the crystalline phases present in the sample diffract the X-ray to characteristic angles ( $2\theta$ ). Thanks to a database (X-pert) it is possible to identify the crystalline compounds formed in the glass-ceramic as consequence of the thermal treatments.

### 3.1. Sr-based systems

HJ14 is a borosilicate Sr-based composition, containing also slight amounts of alumina ( $\text{Al}_2\text{O}_3$ ) and calcium oxide ( $\text{CaO}$ ).

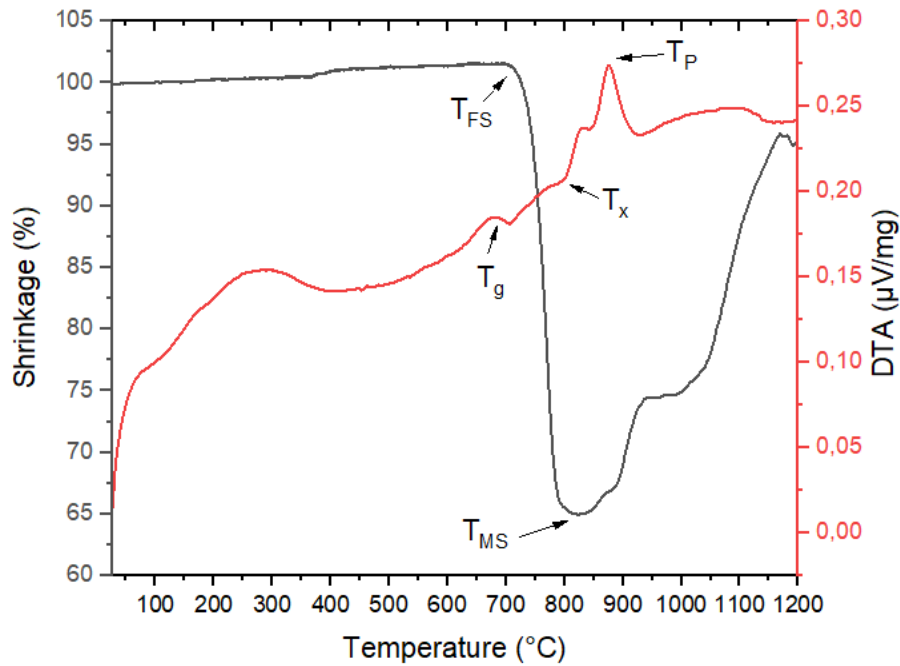


Figure 3.1: DTA curve (red) and HSM curve (black) for the HJ14.

Figure 3.1 shows the results of DTA and HSM analyses carried out on HJ14 powders. The system has a  $T_g$  of 702 °C, a crystallization onset detected at 855 °C ( $T_x$ ) and a crystallization peak temperature of 876 °C. The sintering process, occurring in the range 702-814 °C ( $T_{FS}$ - $T_{MS}$ ), ended before the crystallization process as expected, with a  $T_{MS} < T_x$ .

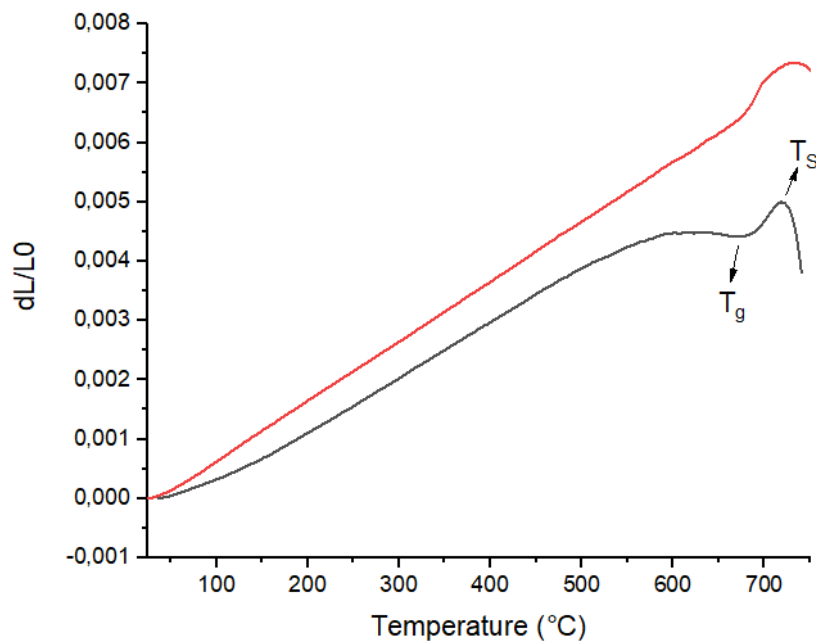


Figure 3.2: dilatometry curves of the HJ14 as-casted glass (black) and as-joined glass-ceramic (red).

The joining thermal treatment has increased HJ14 CTE from  $9.2 \cdot 10^{-6} \text{ K}^{-1}$  of the as-casted glass to  $10.1 \cdot 10^{-6} \text{ K}^{-1}$  of the as-joined glass-ceramic in the range 200-500 °C. This value is suitable for SOC sealing applications, so a good thermo-mechanical compatibility with the joined materials should be expected for HJ14. The dilatometry curves of both the samples are shown in *Figure 3.2*.

*Figure 3.3* reports the results of the XRD analysis on HJ14 glass-ceramic powders; a higher CTE after the thermal treatment was due to the presence of strontium silicate crystals ( $\text{SrSiO}_3$ ) in the glass-ceramic structure, which was the only crystalline phase detected in the as-joined state.

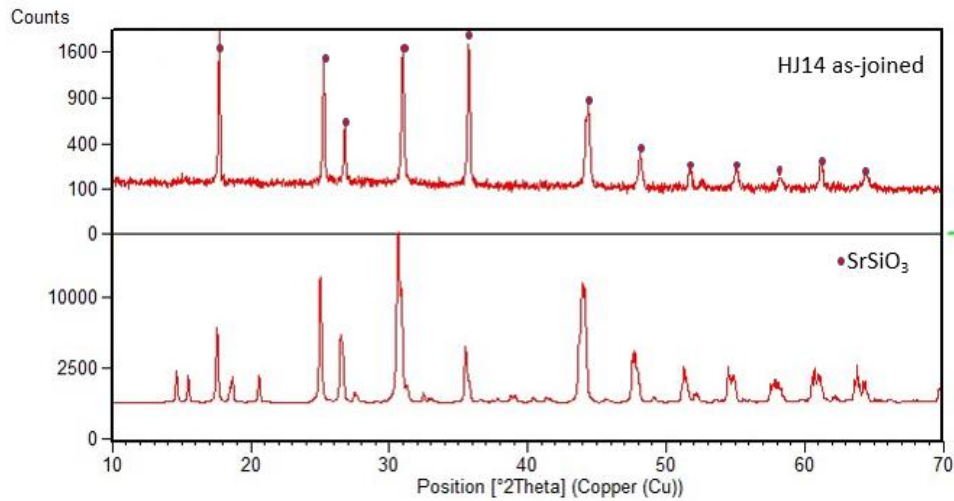


Figure 3.3: XRD analysis on the HJ14 as-joined glass-ceramic powders.

*Figure 3.4* shows an excellent wettability of the Crofer plates and the 3YSZ layer by the glass-ceramic sealant. Moreover, the thermal treatment for the crystallization and the joint has not induced any critical porosity in the joining layer. The SEM image has confirmed that the good CTE of the HJ14 as-joined glass-ceramic avoided the formation of cracks or other thermomechanical issues during the joining thermal process. Furthermore, no detrimental reaction seems to have taken place between the glass-ceramic and the steel after the thermal treatment. It is also possible to see that the crystal phase (light grey shapes) is considerable and it is present in extent higher than the amorphous one (dark grey), confirming the “refractory” nature of the HJ14 suggested by XRD analyses.

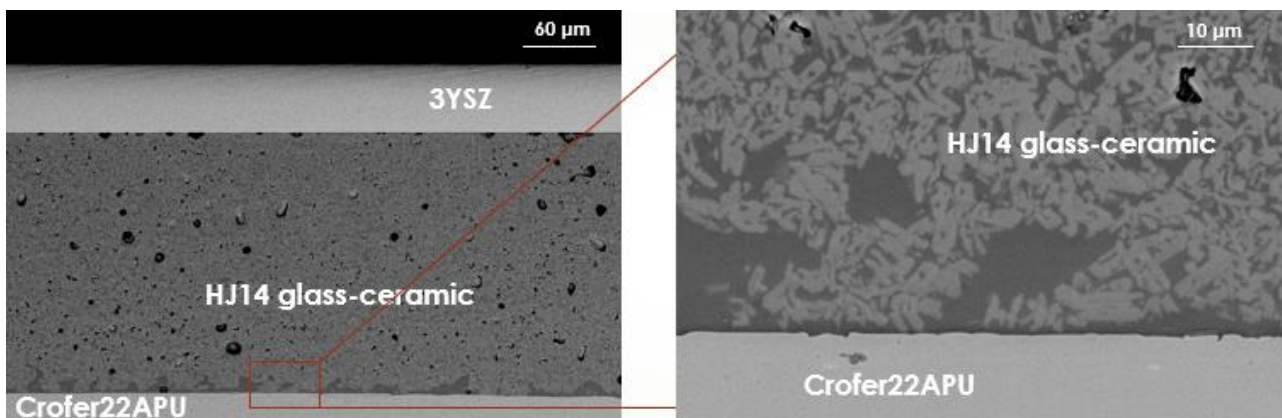


Figure 3.4: SEM image of a Crofer22APU/HJ14 glass-ceramic/3YSZ joined sample.

GS7 is a borosilicate Sr-based glass obtained by modifying the HJ14 composition. The main objective was to reduce the refractory nature of the HJ14 (increasing the amount of residual glassy phase in the glass-ceramic) by designing a new composition with the same  $\text{SiO}_2/\text{SrO}$  ratio and with higher amounts of  $\text{Al}_2\text{O}_3$  and  $\text{Ga}_2\text{O}_3$  to delay the crystallization process, as suggested by the literature [28, 29, 30].

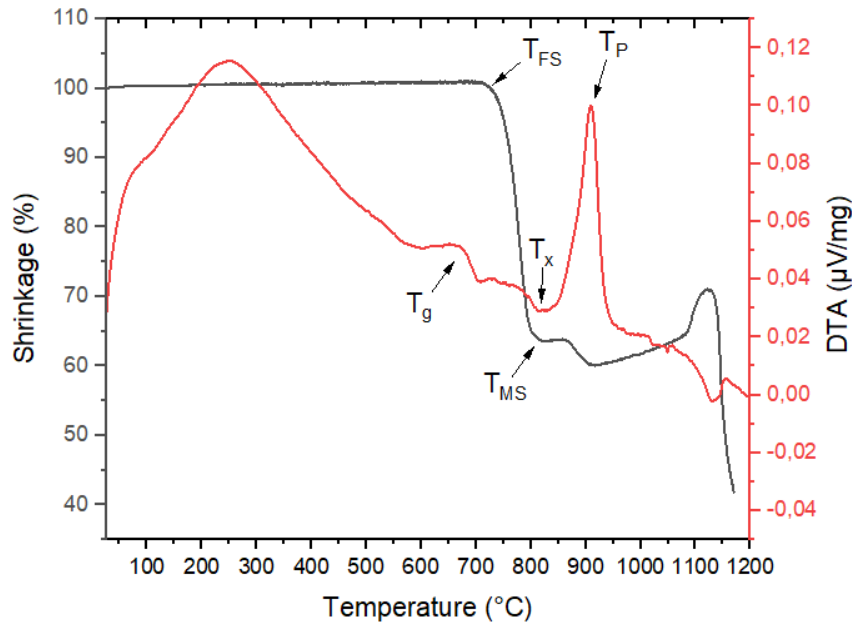


Figure 3.5: GS7 DTA curve (red) and HSM curve (black).

The curves obtained at the end of the differential thermal analysis and the Heating Stage Microscopy on the GS7 system are illustrated in *Figure 3.5*. The glass transition temperature is  $695\text{ °C}$ , while the crystallization process occurred at  $886\text{ °C}$  ( $T_x$ ), reaching its maximum at  $909\text{ °C}$  ( $T_p$ ). The sintering process, occurred in the range  $708\text{--}827\text{ °C}$  ( $T_{FS}\text{--}T_{MS}$ ), ended before the crystallization process initiating, with a  $T_{MS} < T_x$ .

The dilatometry tests have been performed on the glass as-casted and on the as-joined glass-ceramic:

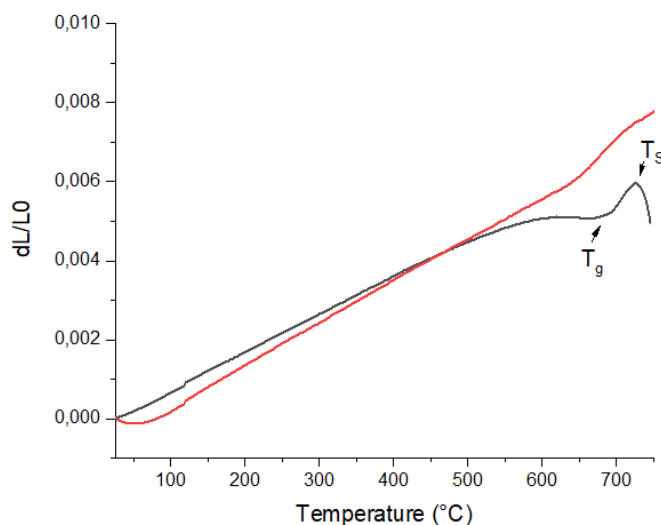


Figure 3.6: dilatometry curves of GS7 as-casted glass (black) and as-joined glass-ceramic (red).

GS7 has a  $T_s$  of 726 °C; the as-casted glass has a CTE of  $9.3 \cdot 10^{-6} \text{ K}^{-1}$ , strongly dependent on the presence of alkaline earth oxides and  $\text{B}_2\text{O}_3$ . The crystal phase formed inside the GS7 after the joining thermal treatment led to a significant increase in the CTE value, from  $9.3 \cdot 10^{-6} \text{ K}^{-1}$  to  $10.6 \cdot 10^{-6} \text{ K}^{-1}$ . Also in this case this value can be considered suitable for SOCs sealing. Dilatometry curve recorded on the as-joined glass-ceramic shown in *Figure 3.6* suggests also a lower refractory nature of the GS7 glass-ceramic with respect to HJ14, as expected; an evidence of the residual glassy phase is visible at 650°C about. To deeply understand which are the crystalline phases involved in the CTE variation, XRD analyses were performed on GS7 as-joined glass-ceramic powder.

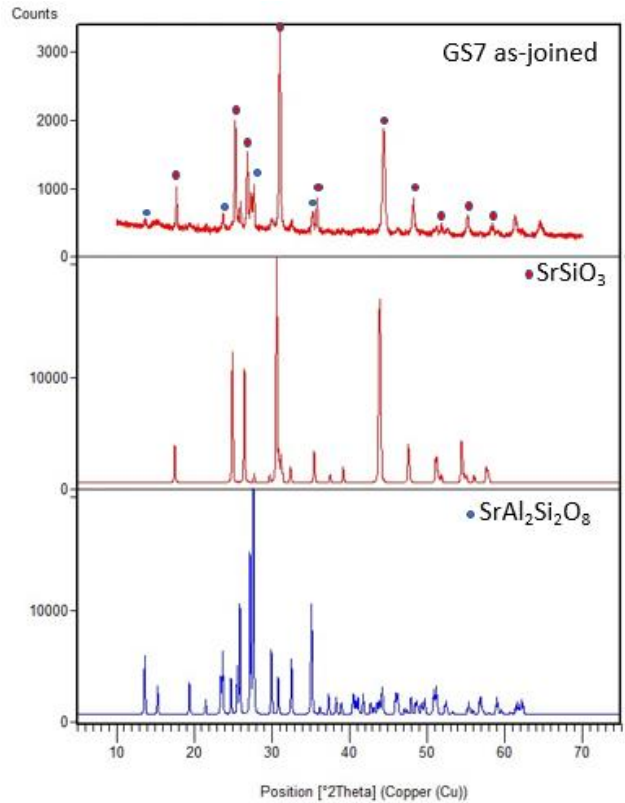


Figure 3.7: XRD analysis on the GS7 as-joined glass-ceramic powders.

XRD analyses are reported in *Figure 3.7*. According to its composition, in the GS7 as-joined powders the presence of  $\text{SrSiO}_3$  was detected together with a lower amount of undesired  $\text{SrAl}_2\text{Si}_2\text{O}_8$  phase; the presence of strontium silicate was confirmed also by the SEM and EDS analysis on the Crofer22APU/GS7 glass-ceramic/Crofer22APU as-joined sample, shown in *Figure 3.8*.

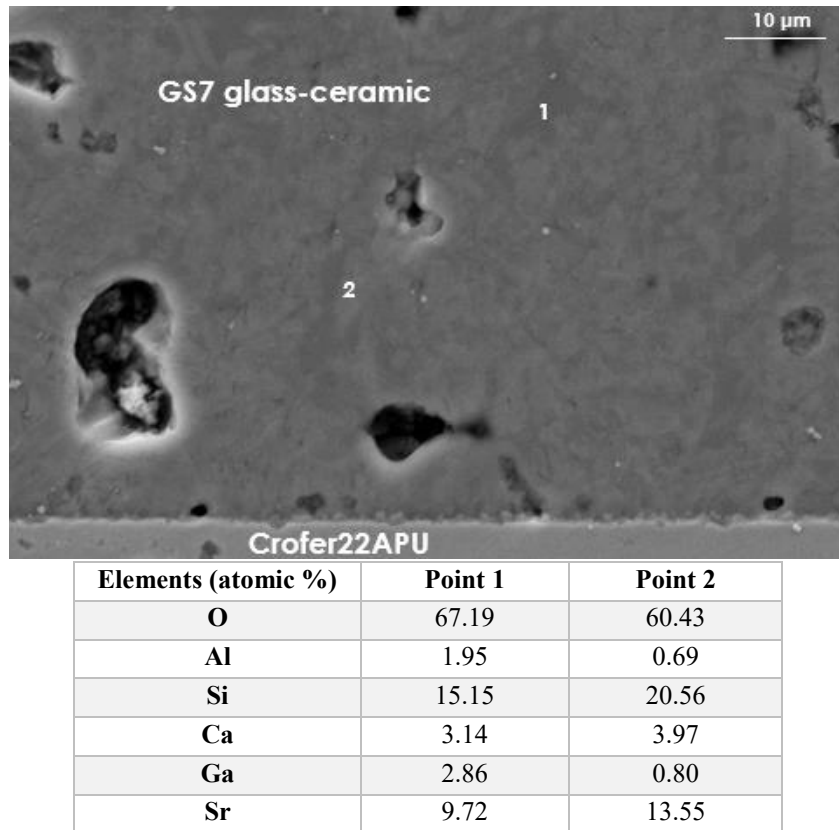


Figure 3.8: SEM and EDS on a Crofer22APU/GS7 glass-ceramic/Crofer22APU as-joined sample.

Point 2 in *Figure 3.8* contains only O, Si, Ca and Sr, thus revealing strontium silicate (with slight amount of diffused Ca) already detected in the XRD analysis; the other composition (point 1) refers to the residual amorphous phase.

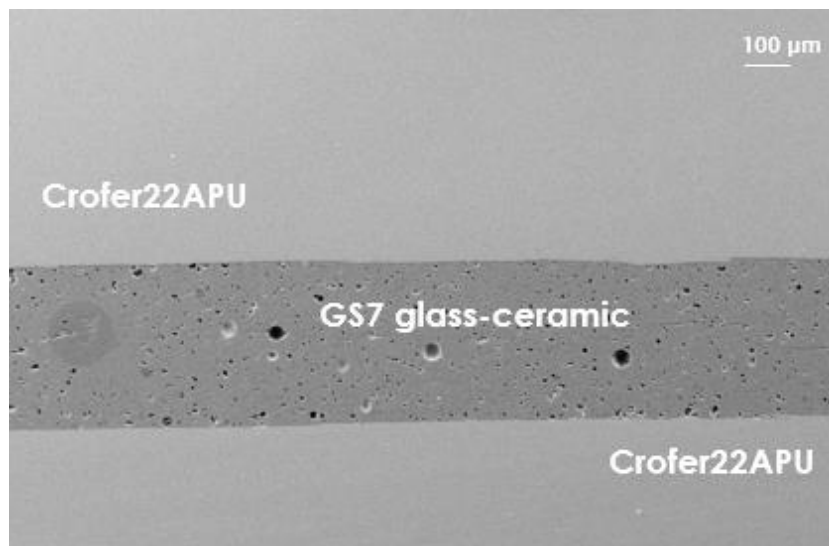


Figure 3.9: SEM image of a Crofer22APU/GS7 glass-ceramic/Crofer22APU as-joined sample.

*Figure 3.9* shows a perfect wettability of the Crofer plates by the glass-ceramic sealant. Moreover, the joining area does not show any critical porosity or cracks induced by the crystallization and joining thermal treatment. The SEM image confirmed that the good CTE of the GS7 as-joined glass-ceramic avoided the formation of cracks or other thermomechanical failures during the joining thermal process.

### 3.2. Ba-based systems

HJ11 is a borosilicate Ba-based glass containing also slight amounts of  $\text{Al}_2\text{O}_3$  and  $\text{CaO}$ .

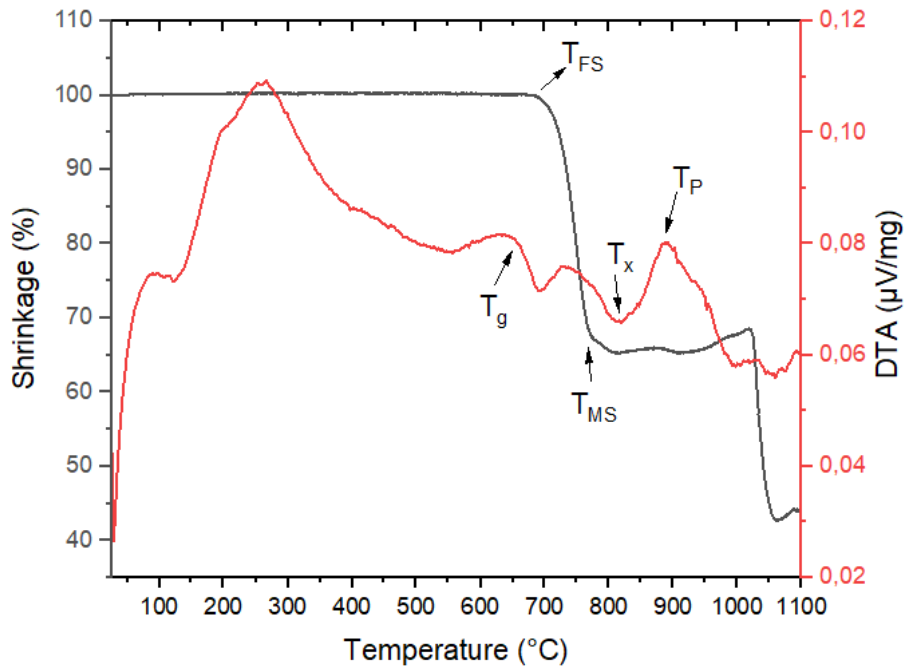


Figure 3.10: HJ11 DTA curve (red) and HSM curve (black).

HJ11 glass transition temperature suggested by the DTA and reported in *Figure 3.10* was found to be  $680\text{ }^\circ\text{C}$ ; furthermore, the DTA curve presents a clear crystallization onset at  $833\text{ }^\circ\text{C}$  and a crystallization peak at  $887\text{ }^\circ\text{C}$ . The sintering process occurred in the range  $675\text{--}778\text{ }^\circ\text{C}$ , so before the crystallization process started ( $T_x > T_{MS}$ ).

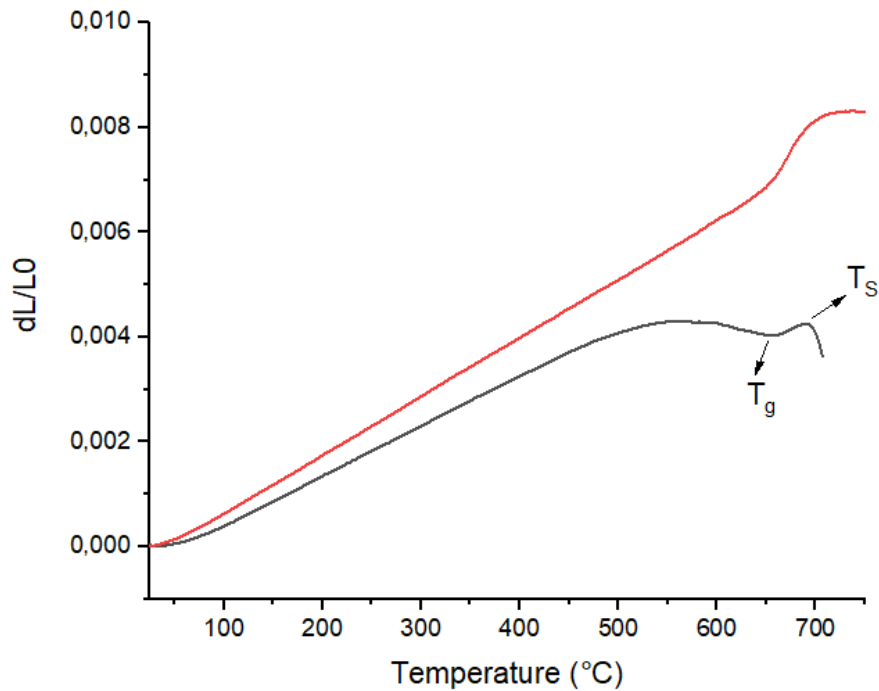


Figure 3.11: Dilatometry curves of HJ11 as-casted glass (black) and as-joined glass-ceramic (red).

From the dilatometric analyses, the glass CTE has been evaluated as  $9.1 \cdot 10^{-6} \text{ K}^{-1}$  in the temperature range 200-500 °C, with a softening temperature of 690 °C, so very close to the  $T_g$ . The thermal treatment for the partial crystallization increased the HJ11 CTE up to  $11.2 \cdot 10^{-6} \text{ K}^{-1}$ , laying in the desired range for a rSOC applications. Moreover, the dilatometry curve of the as-joined glass-ceramic (*Figure 3.11*) shows the presence of a residual amorphous phase having a  $T_g$  around 650 °C.

The HJ11 glass has been used to prepare Crofer22APU/HJ11 glass-ceramic/Crofer22APU and Crofer22APU/HJ11 glass-ceramic/3YSZ joined samples. *Figure 3.12* and *Figure 3.13* from SEM show good compatibility at interfaces between the glass-ceramic sealant and both the Crofer and the 3YSZ; furthermore, the joining thermal process did not lead to the formation of cracks or delamination thanks to the close match between the CTEs of the different joined materials. SEM detected the presence of bright crystalline phase together with a consistent surrounding residual glassy phase. The amount of visible glassy phase suggests a more viscous behaviour as expected from the dilatometry results.

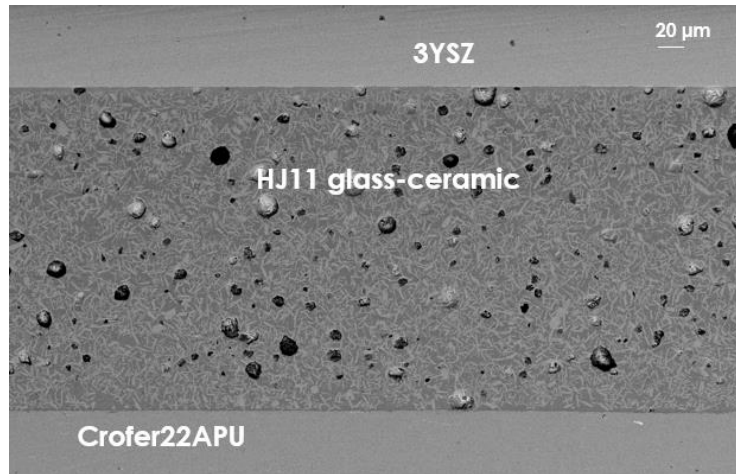


Figure 3.12: SEM image of a Crofer22APU/HJ11 glass-ceramic/3YSZ joined sample.

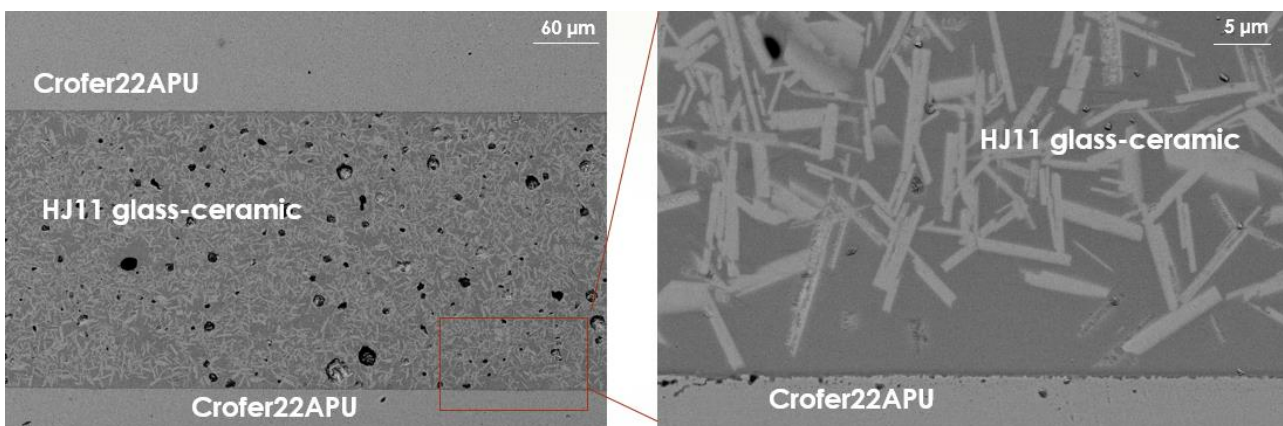


Figure 3.13: SEM images of a Crofer22APU/HJ11 glass-ceramic/3YSZ joined sample.

The XRD analysis (*Figure 3.14*) on the HJ11 as-joined glass-ceramic powders detected barium silicate ( $\text{BaSi}_2\text{O}_5$ ), also known as sanbornite, as main crystal phase after the joining thermal process. An amorphous halo is also present at low  $2\theta$  angles, thus suggesting the presence of a residual glassy phase.

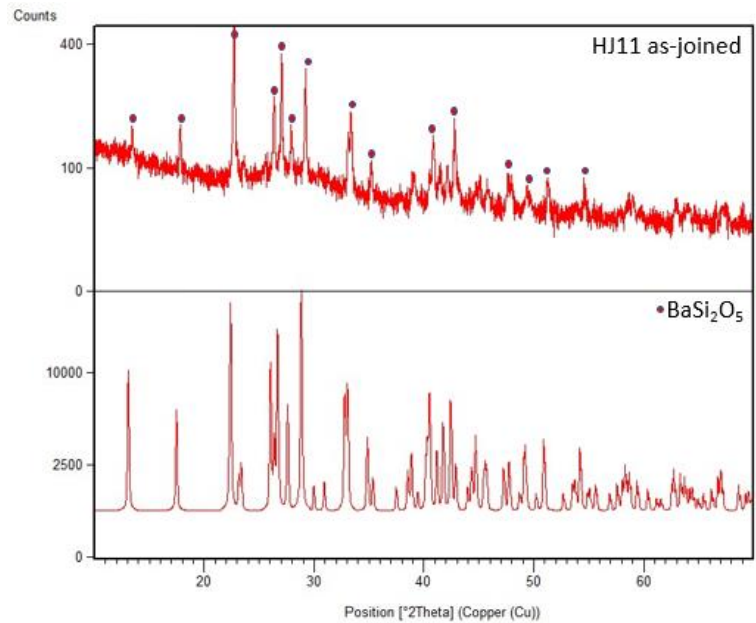


Figure 3.14: XRD analysis on the HJ11 as-joined powders.

HJ26 and HJ27 are two borosilicate Ba-containing glasses characterized by a very similar composition, so their thermal characterization was carried simultaneously. They were designed starting from the HJ11 composition, using the same  $\text{SiO}_2/\text{BaO}$  ratio and partially substituting  $\text{Al}_2\text{O}_3$  with  $\text{Ga}_2\text{O}_3$  in order to obtain a higher amount of residual glassy phase.

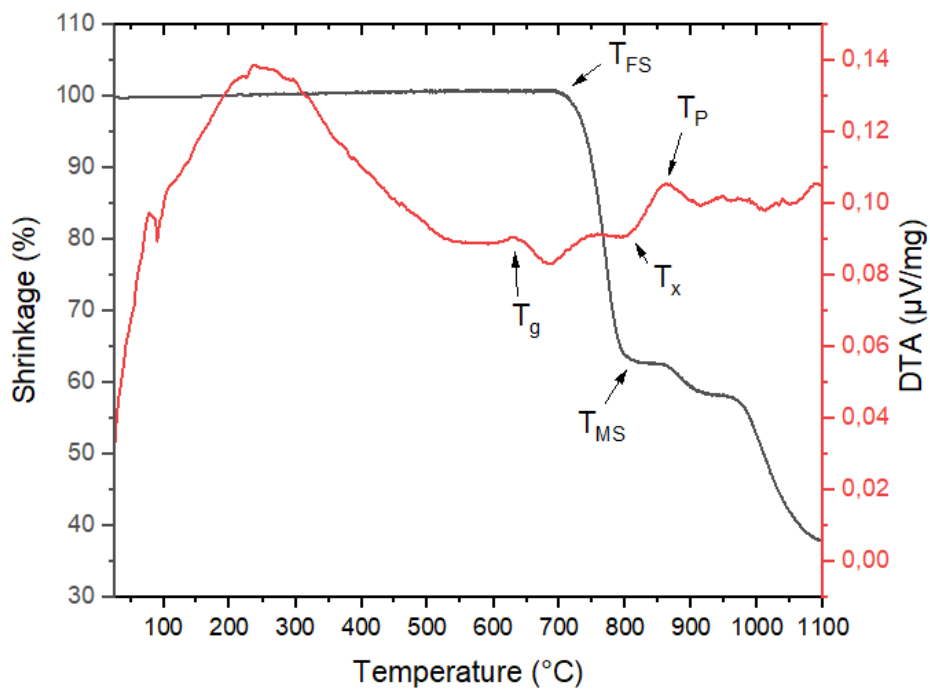


Figure 3.15: HJ26 DTA curve (red) and HSM curve (black).

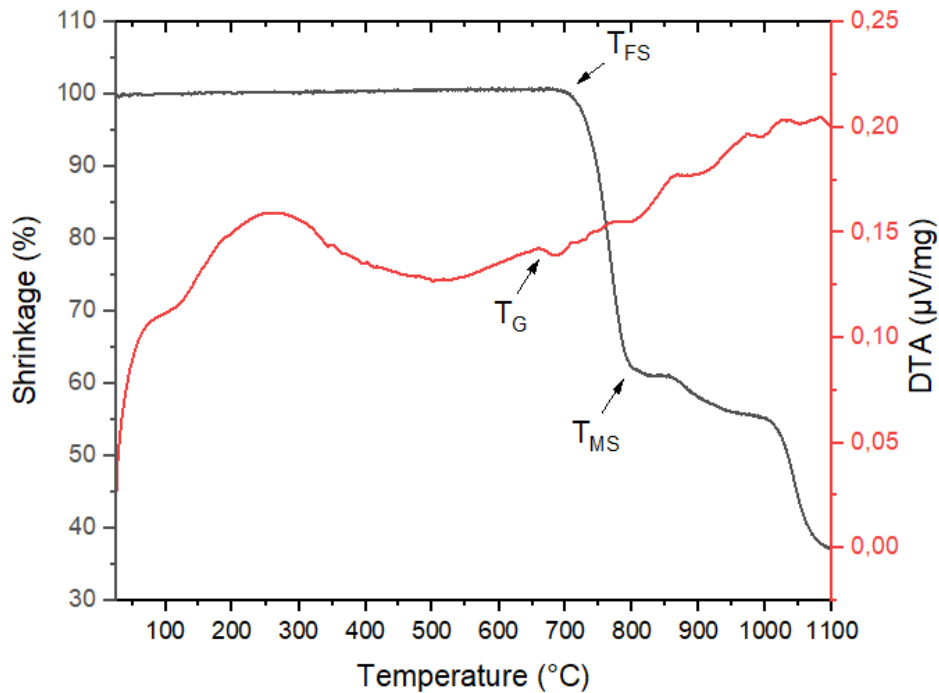


Figure 3.16: HJ27 DTA curve (red) and HSM curve (black).

In HJ26 and HJ27 compositions, formers and modifiers oxides were similar in terms of chemical species and quantities, so it is not surprising that the  $T_g$  of both the glasses are very close each other (673 °C and 677 °C for the HJ26 and the HJ27 respectively) as pointed out by DTA. Moreover, both the systems have similar sintering temperature ranges (696-835 °C and 696-828 °C for the HJ26 and HJ27 respectively). In comparison with HJ11, HJ26 and HJ27 curves (reported in *Figure 3.15* and *Figure 3.16*) a clear crystallization peak is not visible. This suggests that both the compositions have not a refractory nature as expected, thus confirming the tailoring of the parent glass composition.

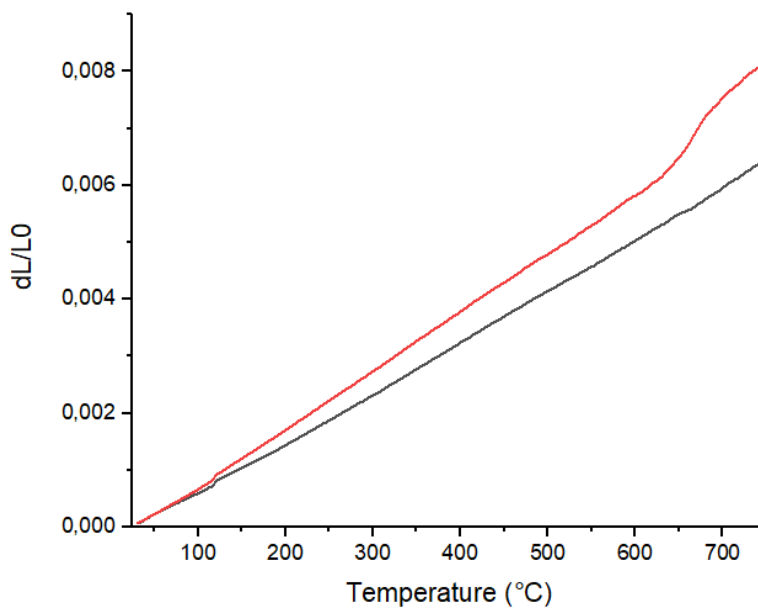
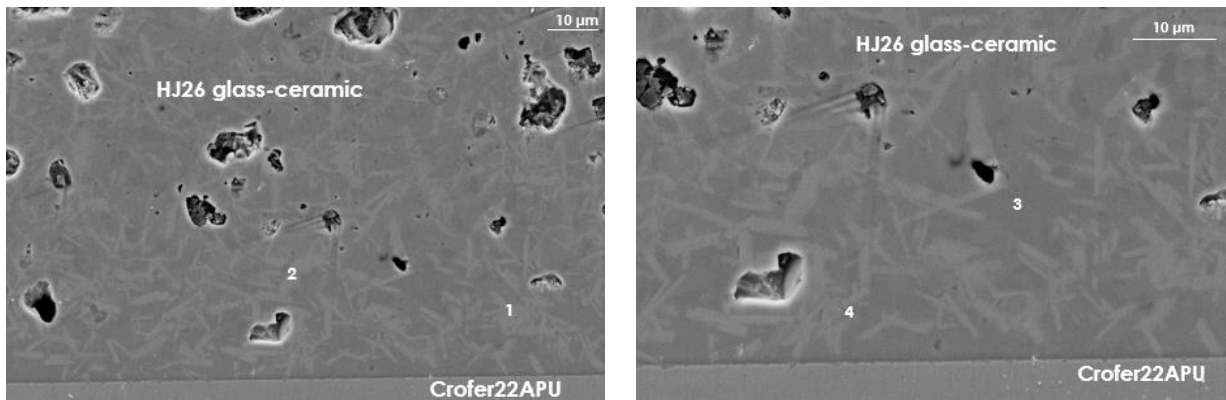


Figure 3.17: Dilatometry curves of HJ26 (black) and HJ27 (red) as-joined glass-ceramics.

The HJ26 dilatometry curve in *Figure 3.17* suggests a high degree of crystallization, in contrast with the DTA results discussed above. Furthermore, the CTE value ( $9.0 \cdot 10^{-6} \text{ K}^{-1}$ ) could not be acceptable for rSOC applications. On the contrary, the HJ27 dilatometry curve shows different results in terms of trend and CTE value in comparison with HJ26; the curve is not perfectly linear, and this suggests the presence of a residual amorphous phase having a  $T_g$  in the range 640-680 °C. The CTE value obtained ( $10.3 \cdot 10^{-6} \text{ K}^{-1}$ ) is closer to the typical materials to be sealed.

Point number 1 and point number 2 in *Figure 3.18*, according to their compositions, were identified as barium silicate crystals, very frequent in this kind of system. This crystalline phase allowed an overall CTE increment, but the value obtained was still outside the acceptability range. Compositions 3 and 4 indicated the residual amorphous phase, which is not very presents compare to the crystalline phase, as already suggested by the dilatometry curve.



Elements (atomic %)	Point 1	Point 2	Point 3	Point 4
O	43.45	41.92	48.04	44.59
Al			3.16	3.18
Si	38.79	39.39	28.97	32.14
Ca			4.93	3.73
Ga			2.30	2.10
Ba	17.76	18.70	12.60	14.26

Figure 3.18: SEM and EDS on a Crofer22APU/HJ26 glass-ceramic/Crofer22APU joined sample.

*Figure 3.19* from the SEM suggests that both the glass-ceramic layer and the bonding interfaces have not any critical defect induced by the thermal treatment, despite the low CTE value detected by the dilatometry test.

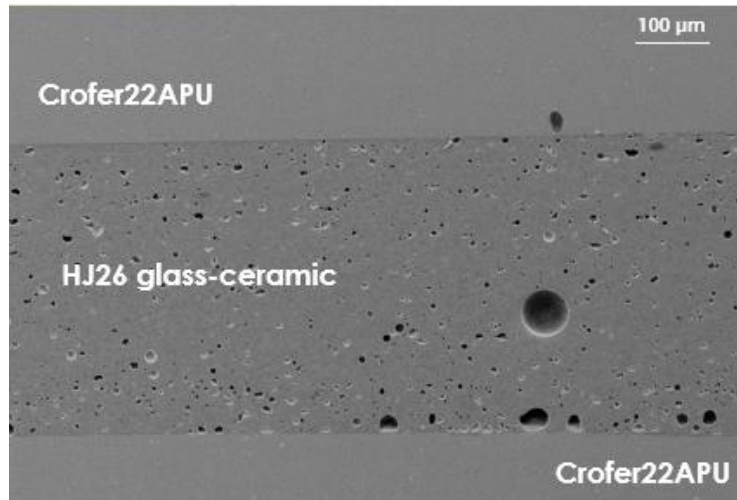
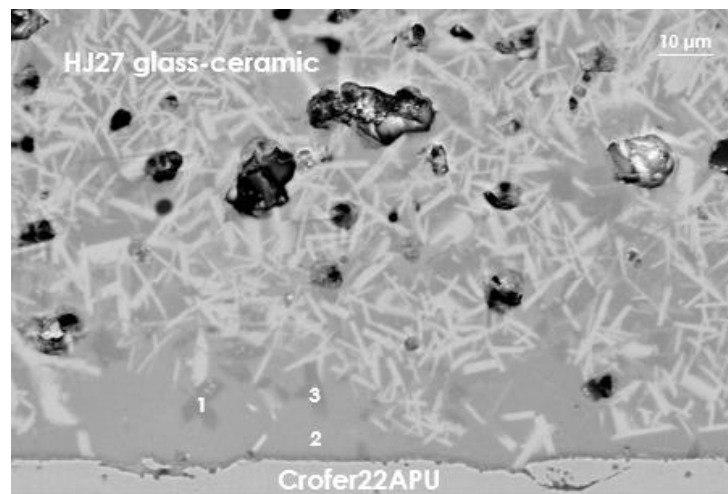


Figure 3.19: SEM image of a Crofer22APU/HJ26 glass-ceramic/Crofer22APU as-joined sample.

The grey shapes observed in *Figure 3.20* and labelled as point number 1 and point number 3 are composed by O, Si, Ca and Ba, so they were identified as barium calcium orthosilicate crystals, a negligible phase which was not detected by the XRD analysis. The other composition detected refers to the residual amorphous phase of the glass-ceramic sealant, present in high extent according also to the dilatometry curve.



Elements (atomic %)	Point 1	Point 2	Point 3
O	47.61	53.61	47.94
Al		1.86	
Si	29.17	25.56	28.45
Ca	13.19	3.61	13.98
Cr		1.21	
Ga		53.61	
Ba	10.03	1.86	9.63

Figure 3.20: SEM and EDS on a sample made of two Crofer 22 APU plates joined through HJ27 glass-ceramic.

The bonding interfaces in *Figure 3.21* look intact and the porosity of the glass-ceramic system is negligible. The HJ27 glass-ceramic compatibility with Crofer22APU avoided the formation of cracks during the thermal treatment.

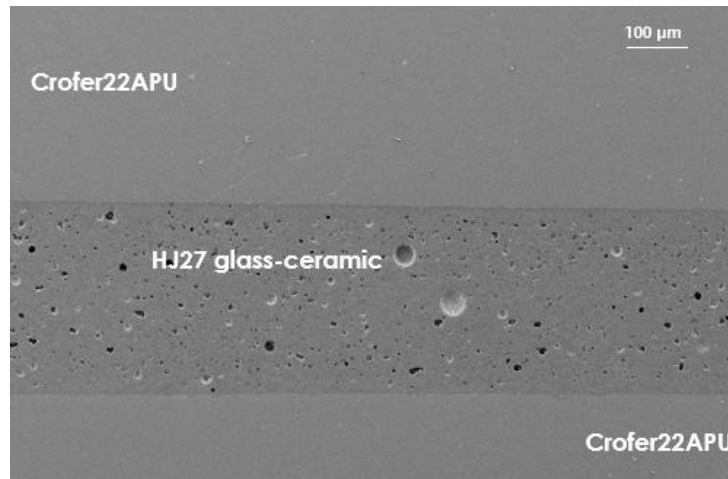


Figure 3.21: SEM on a sample made of two Crofer 22 APU plates joined through HJ27 glass-ceramic.

From the XRD analyses on HJ26 and HJ27 glass-ceramic as-joined, reported in *Figure 3.22* and *Figure 3.23* respectively it is possible to identify the barium silicate ( $\text{BaSi}_2\text{O}_5$ ) as the predominant crystalline phase in the structure, as expected according to their compositions and to the results of the EDS analysis shown in *Figure 3.18* and *Figure 3.20*. The amorphous halo in *Figure 3.23* confirms the presence of a considerable amount of glassy phase, in line with the DTA, HSM and dilatometry results on HJ27.

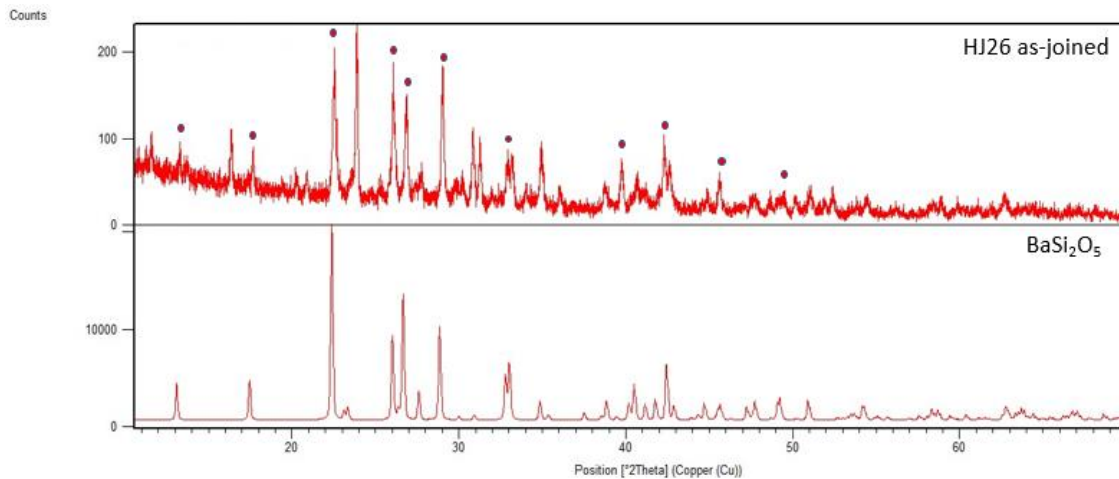


Figure 3.22: XRD analysis on the HJ26 as-joined powders.

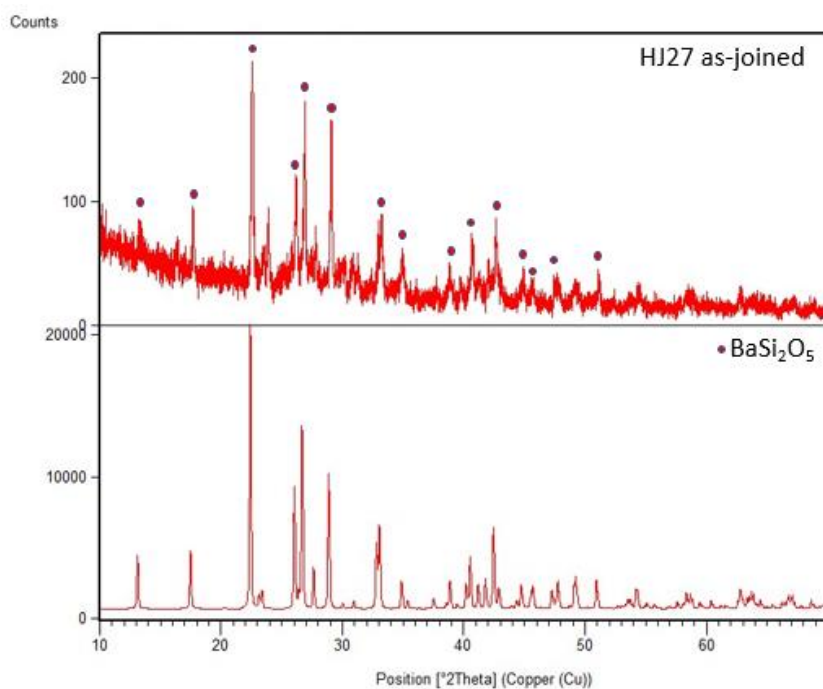


Figure 3.23: XRD analysis on the HJ27 as-joined powders.

HJ28 is the last borosilicate Ba-containing system considered in the present work, composed also by  $\text{Al}_2\text{O}_3$ ,  $\text{CaO}$  and a small amount of  $\text{Y}_2\text{O}_3$ . With respect to the other Ba-based systems, in HJ28 a different  $\text{SiO}_2/\text{BaO}$  ratio was chosen and a slight amount of  $\text{Y}_2\text{O}_3$  was added to partially substitute the  $\text{Al}_2\text{O}_3$ . The main purpose of this strategy was to further reduce the tendency to crystallize of HJ11. Furthermore, the content of  $\text{Al}_2\text{O}_3$  was also reduced to minimize the possibility of formation of the celsian phase ( $\text{BaAl}_2\text{Si}_2\text{O}_8$ ) after the thermal treatments.

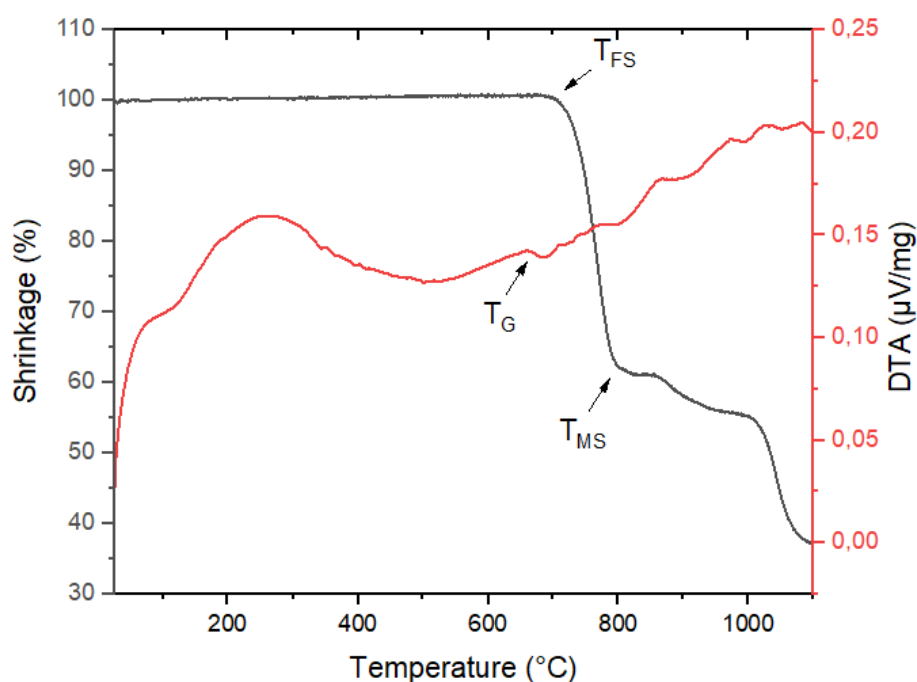


Figure 3.24: HJ28 DSC curve (red) and DTA curve (black).

Despite of the content of modifier oxides in HJ28 composition, the DSC curve in *Figure 3.24* shows a high glass transition temperature (706 °C); moreover, the absence of a peak confirms the “viscous” nature of this system, as already seen for the HJ26 and HJ27.

The main weak point of this system is the CTE value of both the as-casted glass and the as-joined glass-ceramic, very close each other ( $8.5 \cdot 10^{-6} \text{ K}^{-1}$  and  $8.8 \cdot 10^{-6} \text{ K}^{-1}$  respectively), obtained by dilatometry characterization in the range 200-500 °C and too low for being used in sealing technology for SOCs. Furthermore, the dilatometry curve on the as-joined glass-ceramic, reported in *Figure 3.2*, shows a net change in its shape at 700 °C, which corresponds to the glass transition temperature of the residual amorphous phase. The glass softening temperature has been evaluated as 720 °C.

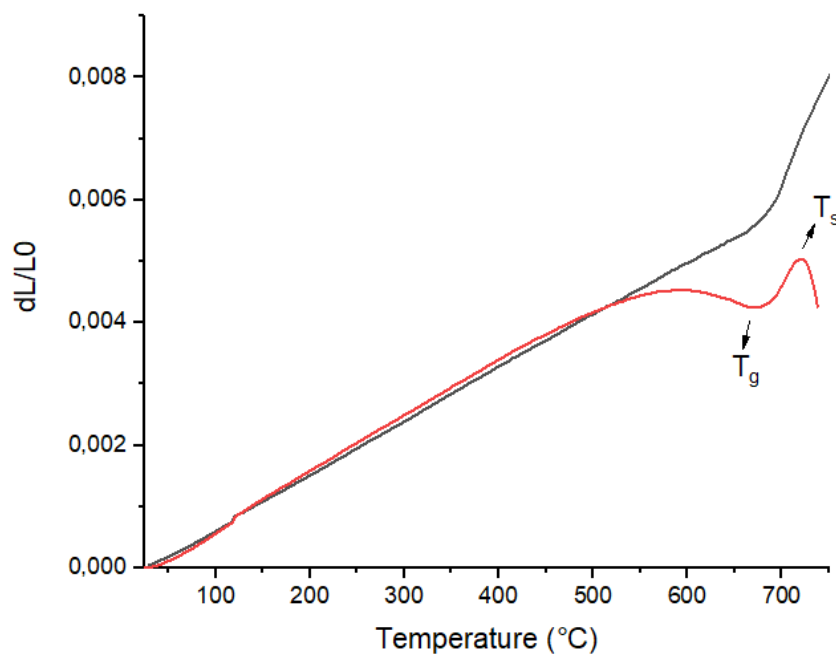
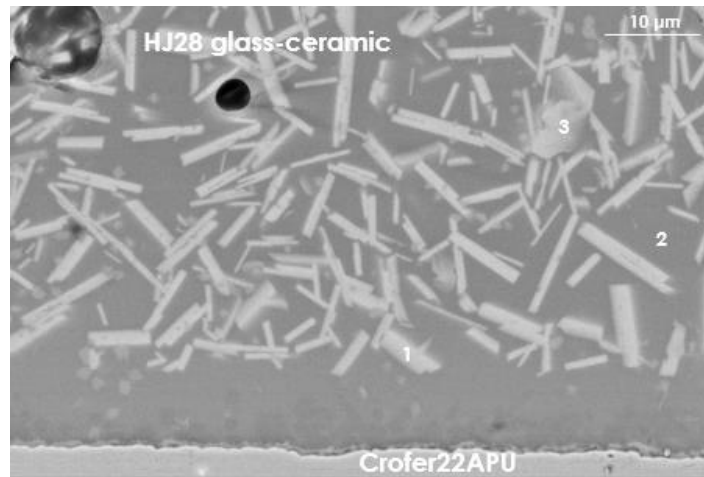


Figure 3.25: Dilatometry curve of HJ28 as-casted glass (red) and as-joined glass-ceramic (black).

The white crystals in *Figure 3.26*, labelled as point 1 and point 3, are composed by O, Si and Ba, so they should be barium silicate, according also to the XRD results (*Figure 3.28*) and the system composition. The detected composition at point 2 refers to the residual amorphous phase, with a high content in the system as expected by the DSC results.



Elements (atomic %)	Point 1	Point 2	Point 3
O	52.28	52.59	47.93
Al		3.67	
Si	30.64	28.08	35.23
Ca	1.48	4.10	1.73
Y		0.87	
Ba	13.38	9.01	15.10

Figure 3.26: SEM and EDS on a Crofer22APU/HJ28 glass-ceramic/Crofer22APU joined sample.

In *Figure 3.27*, obtained at the SEM, a crack can be easily identified in the glass-ceramic layer, originated during the thermal process due to the unacceptable CTE value of the glass-ceramic system.

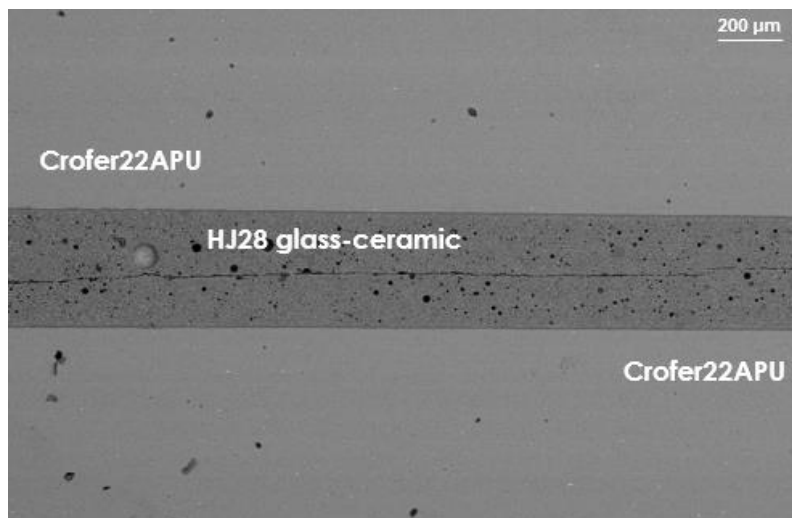


Figure 3.27: SEM image of a Crofer22APU/HJ28 glass-ceramic/Crofer22APU as-joined sample.

In line with the other Ba-based systems, the XRD analysis on HJ28 as-joined powders (*Figure 3.28*) detected the presence of barium silicate (sanbornite) as main crystalline phase in the glass-ceramic structure, confirming the EDS results. Furthermore, a clear amorphous halo is visible in the XRD pattern of the glass-ceramic. This is coherent with the presence of a residual glassy phase previously described.

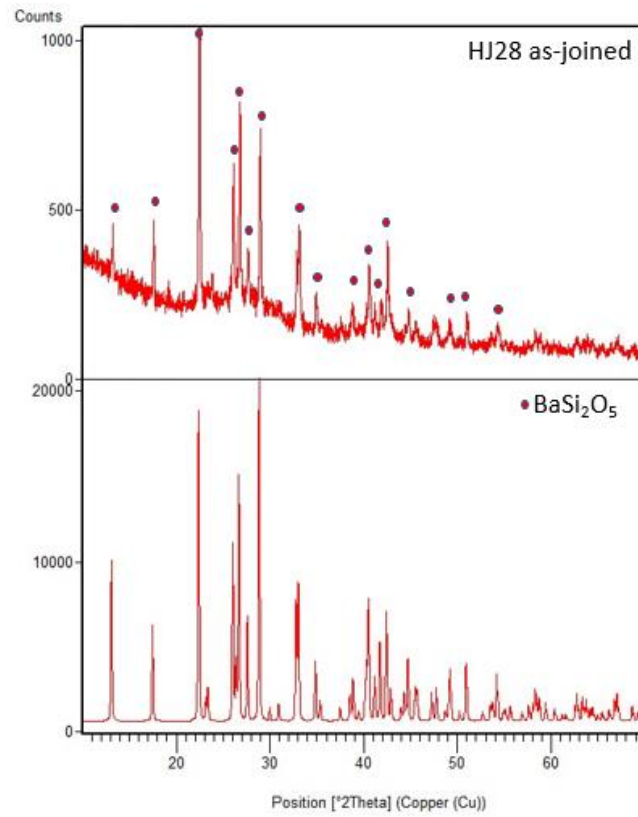


Figure 3.28: XRD analysis on the HJ28 as-joined powders.

## 4. Electrical characterization and post mortem analysis of glass-ceramic sealants

As said before, another important requirement for a SOCs sealant is its electrical resistivity, which is expected in the range  $10^5$ - $10^6 \Omega \text{ cm}$  at high temperatures in order to avoid short circuits. Furthermore, the sealant has to face severe conditions in terms of simultaneous oxidizing and reducing atmospheres, so chemical, thermal and thermo-mechanical stability of sealants in dual atmosphere becomes even more critical, especially at high working temperature and under electric load. Therefore, the performance and reliability of sealants in dual atmosphere needed to be investigated.

In this study, the glass-ceramic sealants were designed with the aim of working at  $850^\circ\text{C}$ , therefore, their electrical behavior was investigated at the target temperature in the presence of dual atmosphere. During the aging tests, a mixture of hydrogen and steam in different ratio was applied to obtain the real conditions of operation of an rSOC. Two  $4 \times 6 \text{ cm}^2$  Crofer22APU plates were joined using the glass-ceramic systems introduced in Section 3, to produce Crofer22AU/glass-ceramic/Crofer22APU joints. Before joining, Pt wires were welded to the upper and lower Crofer22APU plates of the joined samples and connected to the external voltage source, as illustrated in *Figure 4.1*. The preparation of a Crofer22APU/glass-ceramic/Crofer22APU joint is shown in *Figure 4.2*. Small pieces of YSZ with a thickness of almost  $90 \mu\text{m}$  were used to ensure the final minimum height, by leveling the shrinkage of the glass during sintering. The lower Crofer22APU plate contains two holes to let the gas enter and exiting, as shown *Figure 4.1*. A controlled evaporator mixer and mass flow rate controller were used to control the composition of gases and their flow rate respectively. At the same time, thermocouples and pressure gauges were used to control and to measure temperature and pressure, respectively. A portable flow meter was used to measure the output flow from the furnace.

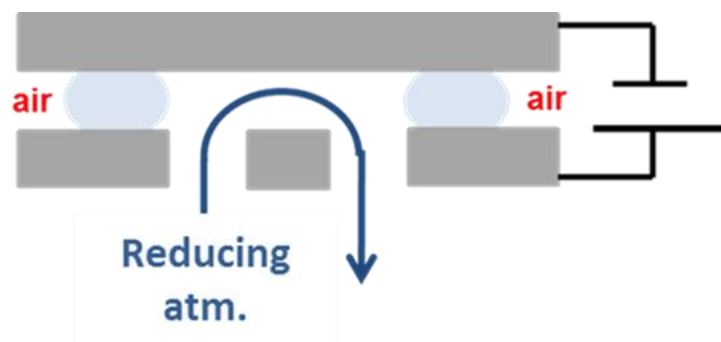


Figure 4.1: Illustration of setup used to measure the electrical resistivity of Crofer22APU/glass-ceramic/Crofer22APU joint in dual atmosphere

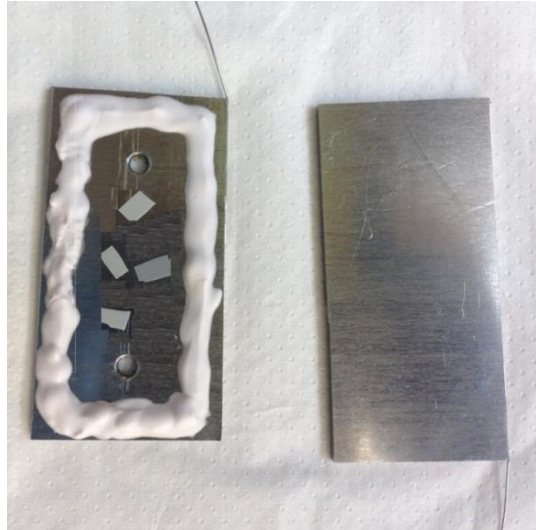


Figure 4.2: Crofer22APU plates with deposited glass slurry.

The process setup to measure the electrical resistivity of the glass-ceramic sealants in dual atmosphere is illustrated in *Figure 4.3*. The electrical resistance in dual atmosphere was measured under the applied voltage of 1.6V, while dual tests were conducted for the duration of 300, 500 and 1000 hours at 850°C. Subsequently, the electrical resistivity was calculated using the data of measured resistance and the area of the glass-ceramic sealant in the joint.

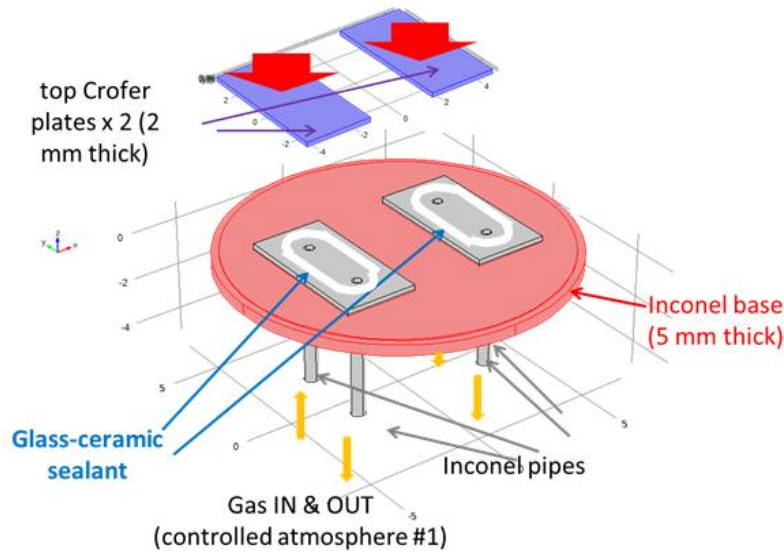


Figure 4.3 Configuration of dual test setup.

After being tested in dual atmosphere, the gas tightness of the the Crofer22APU/glass-ceramic/Crofer22APU joint samples were investigated under the cold leakage test. For this purpose, the joint samples were placed on the surface of a base plate where a sealing was applied between the base plate of the cold leakage setup and the joined samples by using soft plastic O-rings to cover the unwanted gaps. The pressured gas was supplied through one of the holes of the lower Crofer22APU and the flow was measured at the outlet. The difference in the flow rate was used to estimate the gas tightness of the glass-ceramic sealant.

After the aging tests, the samples were further analysed to assess the effects of long term aging in relevant conditions. The aged samples were investigated by means of SEM and EDS to verify the effects of the aging on the morphology and chemistry of the system. Together with the joined samples, for each glass system, glass-ceramic sintered pellets were subjected to the same aging conditions in static air. The aged pellets were analysed by dilatometric tests and XRD, in order to investigate the possible formation of new crystalline phases and how they affected the thermo-mechanical properties.

The long-term resistivity tests were performed at the DENERG (Department of Energy), and labelled as reported in *Table 4.1*:

Table 4.1: Dual test labelling.

	<i>Test G4</i>	<i>Test G6</i>	<i>Test G7</i>
<b>Duration [h]</b>	1000	500	300
<b>Systems</b>	HJ11, HJ14	GS7, HJ26, HJ27	HJ28

#### 4.1. Sr-based systems

The results of the dilatometry measurements performed on two different HJ14 pellets after aging are reported in *Figure 4.4*. An average value for the CTE of  $9.7 \cdot 10^{-6} \text{ K}^{-1}$  was obtained; this value is close to the CTE of the HJ14 as-joined glass-ceramic discussed in Section 3 ( $10.1 \cdot 10^{-6} \text{ K}^{-1}$ ), due to the similar crystalline composition detected by the XRD analysis on both the systems and reported in *Figure 4.5* and *Figure 4.6* respectively.

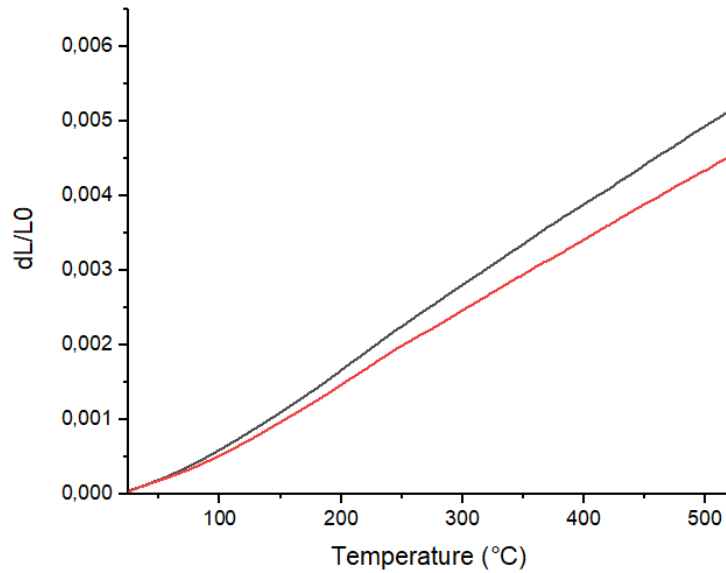


Figure 4.4: HJ14 glass-ceramic pellets after test G4 dilatometry curves.

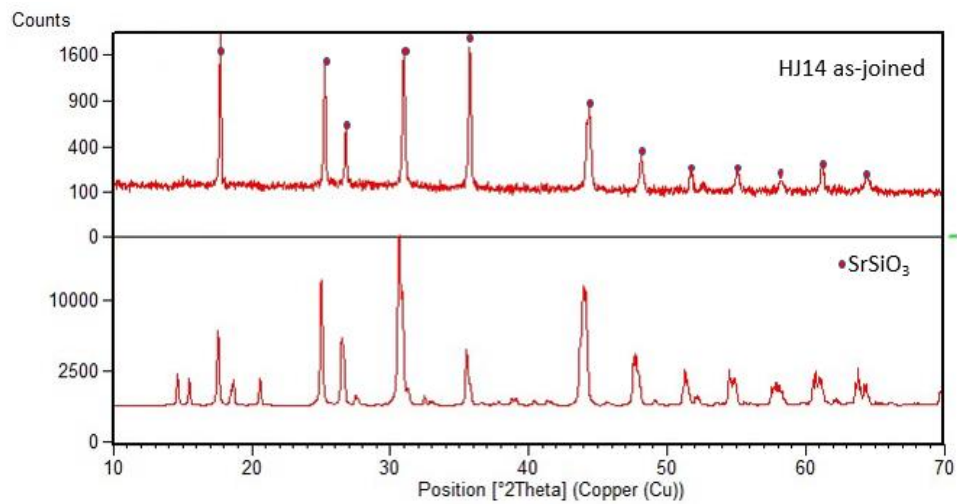


Figure 4.5: XRD analysis on the HJ14 as-joined glass-ceramic powders.

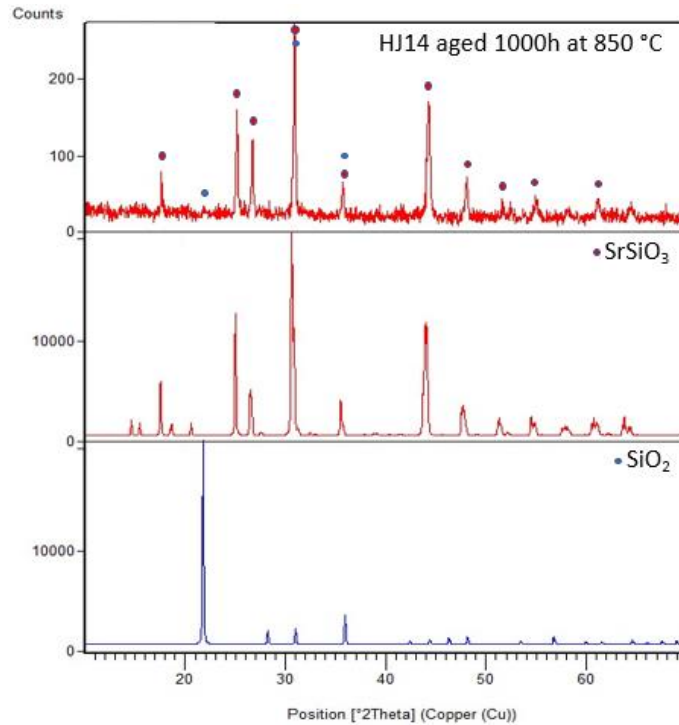
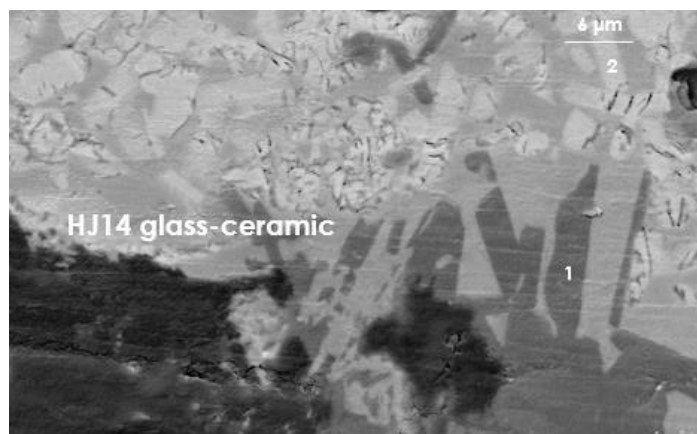


Figure 4.6: XRD analysis on the HJ14 powders after the aging test.

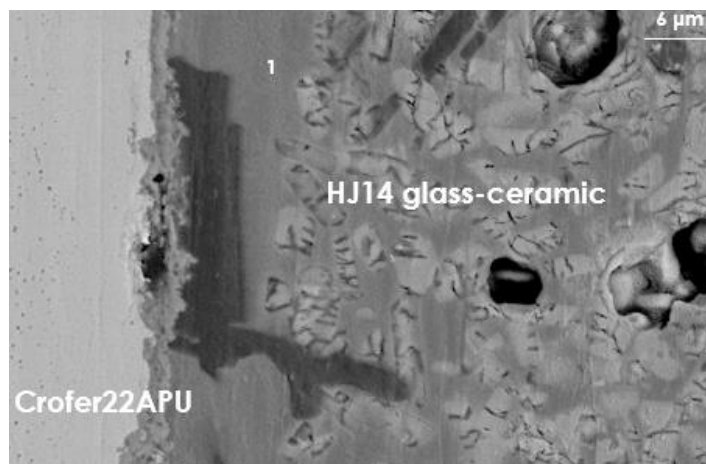
The XRD analysis on HJ14 powders after the aging (*Figure 4.6*) suggests that the  $\text{SrSiO}_3$  is still the most significant crystalline phase in the glass-ceramic, but new peaks appeared as a consequence of the aging. The new phase was identified as  $\text{SiO}_2$ , and SEM and EDS post mortem analyses on the Crofer22APU/HJ14 glass-ceramic/Cofer22APU joined sample after the aging test (*Figure 4.7*, *Figure 4.8* and *Figure 4.9*) confirmed the XRD analysis results. SEM and EDS results suggest also that the amount of  $\text{SrSiO}_3$  is considerable higher than that of the  $\text{SiO}_2$  in the structure, which can be reasonable neglected.

EDS point number 1 in *Figure 4.7* confirms the presence of cristobalite ( $\text{SiO}_2$ ) as secondary phase in the sealant. At the same time, the presence of strontium silicate was also detected, labelled as point number 2. Point number 1 in *Figure 4.8* was collected in the residual amorphous phase of the glass-ceramic system, close to the positive polarized interface. The amounts of Cr, Mn and Fe detected are negligible, thus confirming that diffusion phenomena did not occur during the aging.



Elements (atomic %)	Point 1	Point 2
O	63.1	61.4
Si	36.9	20.1
Ca		3.4
Sr		14.7

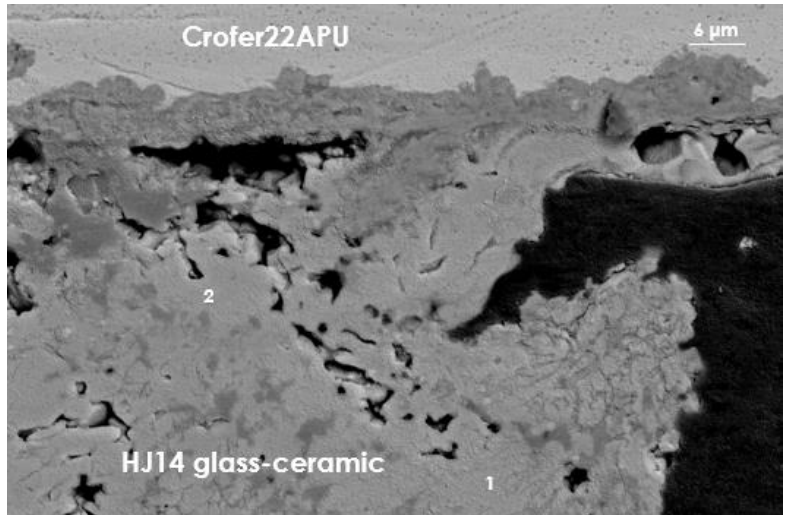
Figure 4.7: SEM and EDS on Crofer22APU/HJ14 glass-ceramic/Crofer22APU joined sample after the aging test, collected close to the positive polarized interface at the fuel side.



Elements (atomic %)	Point 1
O	65.6
Al	3.1
Si	17.3
Ca	2.4
Cr	0.5
Mn	1.4
Fe	0.7
Sr	9.2

Figure 4.8: SEM and EDS on Crofer22APU/HJ14 glass-ceramic/Crofer22APU joined sample after the aging test, collected close to the positive polarized interface.

EDS point number 1 and point number 2 in *Figure 4.9* were identified as strontium silicate crystals, thus confirming their high extent in the glass-ceramic structure. At the same times, the amounts of Cr and Fe detected in *Figure 4.8* are negligible, thus excluding diffusion processes.



Elements (atomic %)	Point 1	Point 2
O	58.1	59.1
Si	21.7	21.7
Ca	4.1	4.1
Sr	16.0	15.1

Figure 4.9: SEM and EDS on Crofer22APU/HJ14 glass-ceramic/Crofer22APU aged sample, negative fuel side, collected close to the negative polarized interface at the fuel side.

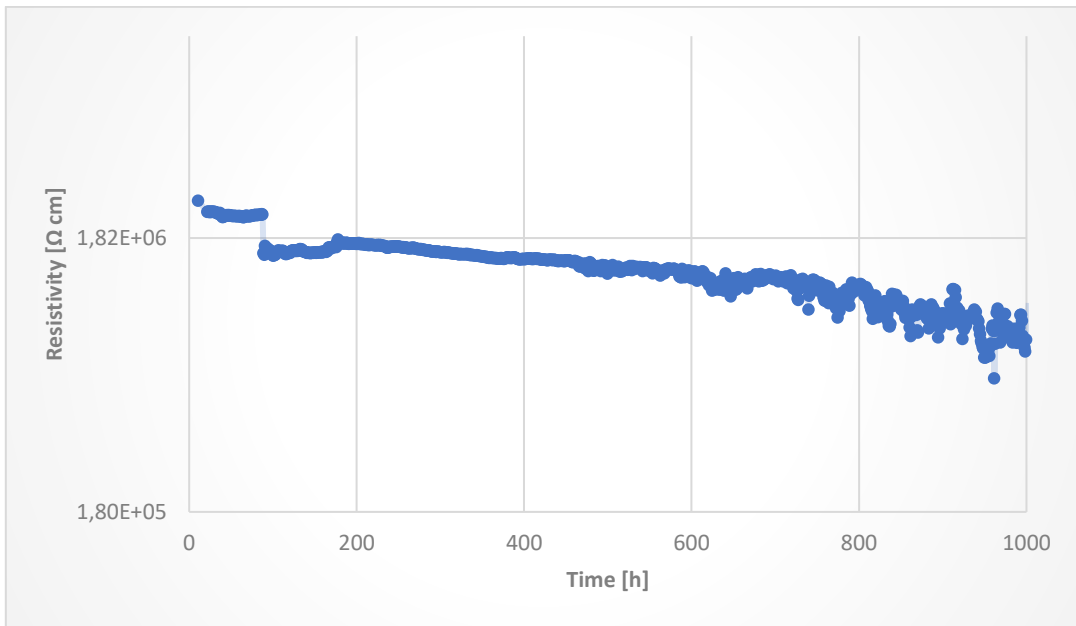


Figure 4.10: HJ14 resistivity curve.

The HJ14 aged glass-ceramic showed an optimal electrical resistivity during 1000h of test in dual atmosphere and under the application of 1.6 V (Figure 4.10). Despite a slight decrease during the test, the electrical resistivity values are always in the range  $10^5$ - $10^6$   $\Omega$  cm, which are considerably higher than the limit to avoid short circuit.

In the case of GS7, the cooling down led to the failure of the joined samples, both the one tested in dual atmosphere and subjected to the application of a voltage and those aged in static air without the applied voltage. This suggest a poor thermo-mechanical compatibility between GS7 and Crofer22APU. Due to this, for all the joined samples

SEM and EDS analyses were not performed. However, dilatometry and XRD analyses were carried out on aged GS7 glass-ceramic pellets in order to investigate its behaviour.

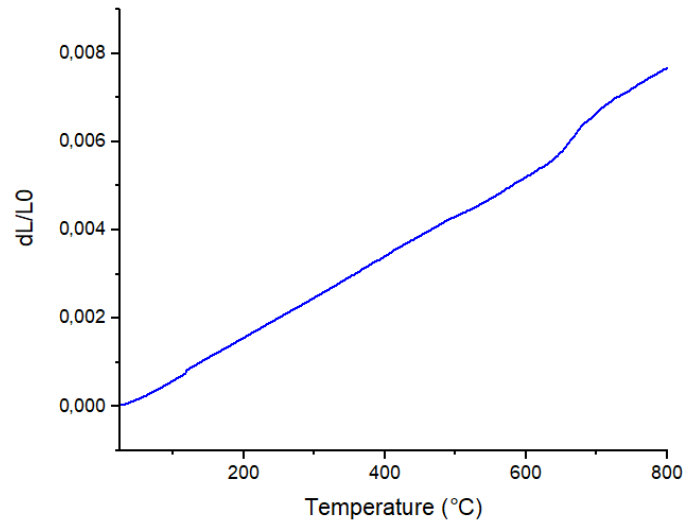


Figure 4.11: GS7 glass-ceramic after test G6+G7 (black) dilatometry curve.

The dilatometry analysis reported in *Figure 4.11* pointed out a CTE value of  $9.2 \cdot 10^{-6} \text{ K}^{-1}$ . The aging led to a decrease of the CTE with respect to the value obtained for the as-joined glass-ceramic ( $10.6 \cdot 10^{-6} \text{ K}^{-1}$  discussed in Section 3), and the new value is outside the acceptability range suggested for rSOC applications.

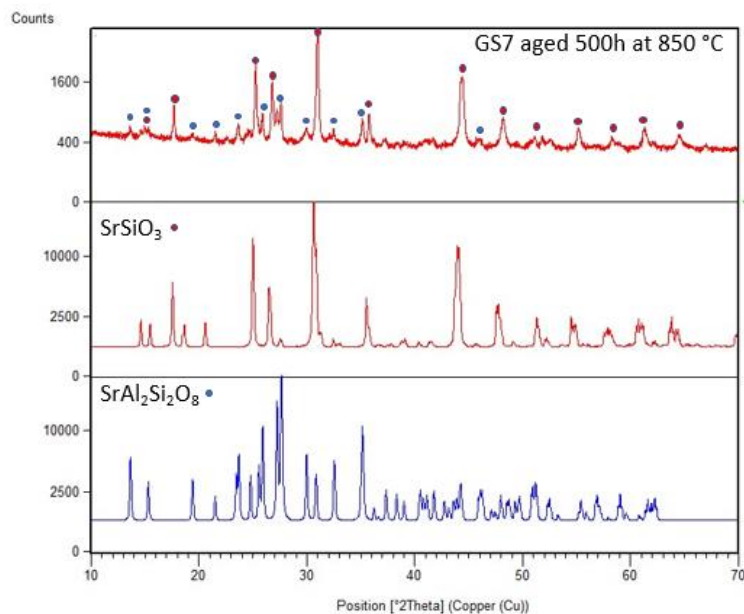


Figure 4.12: XRD analysis on the GS7 aged powders.

The XRD analysis on the aged powders in *Figure 4.12* shows the presence of  $\text{SrAl}_2\text{Si}_2\text{O}_8$  in addition to the  $\text{SrSiO}_3$ , the phase already detected as main one in the as-joined glass-ceramic. The new crystal phase was formed during the aging process due to the

considerable amounts of  $\text{Al}_2\text{O}_3$  adopted in the parent glass composition and used to delay the crystallization process. The main consequence of the  $\text{SrAl}_2\text{Si}_2\text{O}_8$  presence is the CTE variation previously described, which led to the GS7 failure.

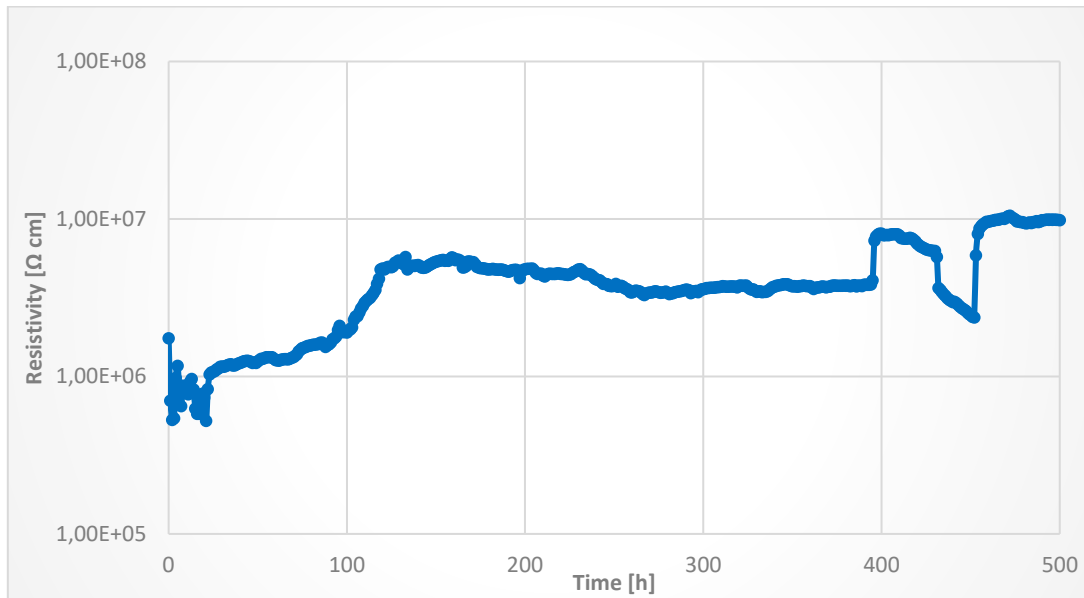


Figure 4.13: GS7 resistivity curve.

After 500 h of aging test at  $850^\circ\text{C}$  in dual atmosphere and under the application of a voltage of 1.6 V, the GS7 glass-ceramic sealant has shown a good electrical resistivity over time, as reported in *Figure 4.13*. The test has been stopped before 1000 h due to the unexpected resistivity drop occurred after 450 h.

## 4.2. Ba-based systems

Crofer22APU/HJ11 glass-ceramic/Crofer22APU joined samples were tested in the G4 test.

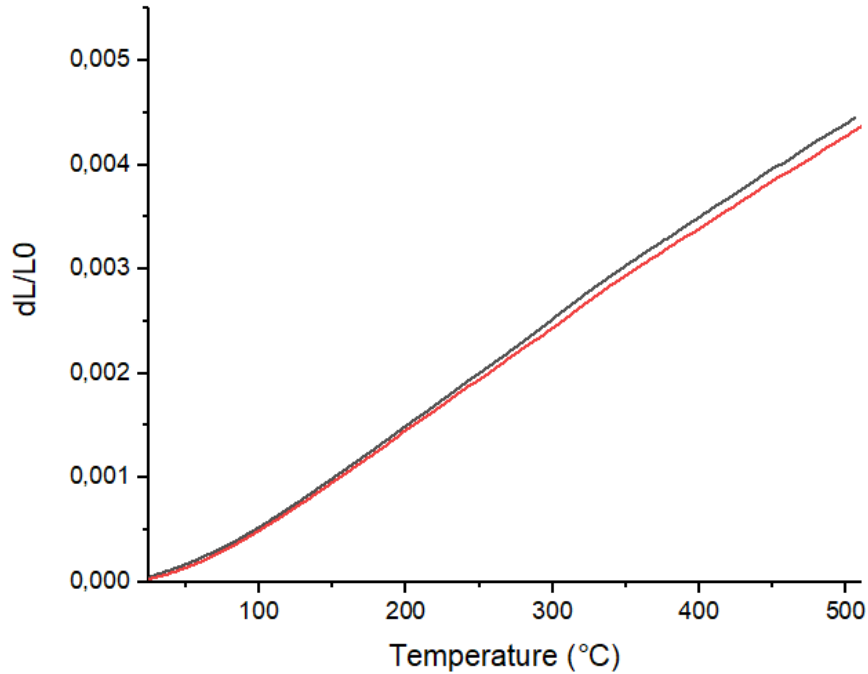


Figure 4.14: HJ11 glass-ceramic after test G4 dilatometry curves.

HJ11 glass-ceramic after the thermal treatment confirmed its refractory behaviour, as suggested by the dilatometric curves of different pellets reported in *Figure 4.14*. The aged glass-ceramic system shown an average CTE of  $9.7 \cdot 10^{-6} \text{ K}^{-1}$  after the aging, lower than the value detected in the as joined state ( $11.1 \cdot 10^{-6} \text{ K}^{-1}$ ).

The EDS analyses close to the interface (*Figure 4.15 a*, point number 1) did not detect Cr, thus excluding diffusion phenomena at the negative interface under the applied electrical load. Point number 2 (*Figure 4.15 b*) was collected in the residual glassy phase, which also contains negligible amounts of Cr and Fe.

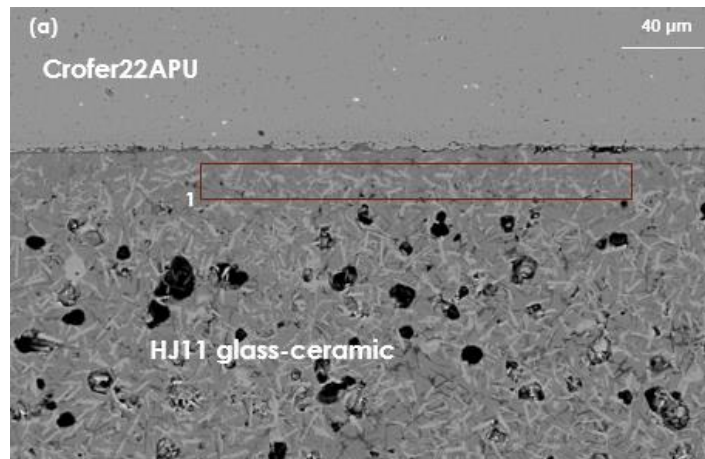
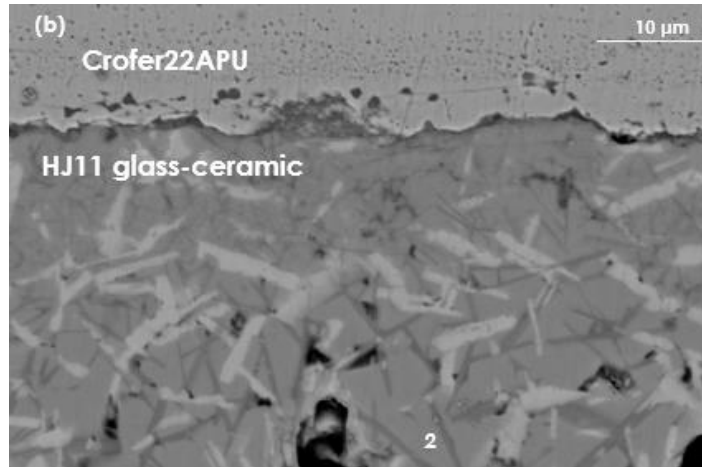


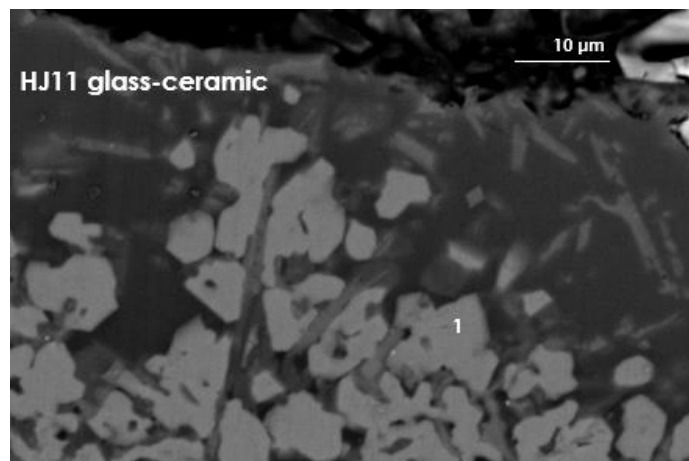
Figure 4.15a: SEM and EDS on Crofer22APU/HJ11 glass-ceramic/Crofer22APU aged sample, collected close to the negative polarized interface.



Elements (atomic %)	Point 1	Point 2
O	65.15	68.13
Al	2.93	1.23
Si	21.02	17.62
Ca	2.18	3.37
Cr		0.59
Fe		1.06
Ba	8.72	8.00

Figure 4.15b: SEM and EDS of Crofer22APU/HJ11 glass-ceramic/Crofer22APU aged sample, collected close to the negative polarized interface.

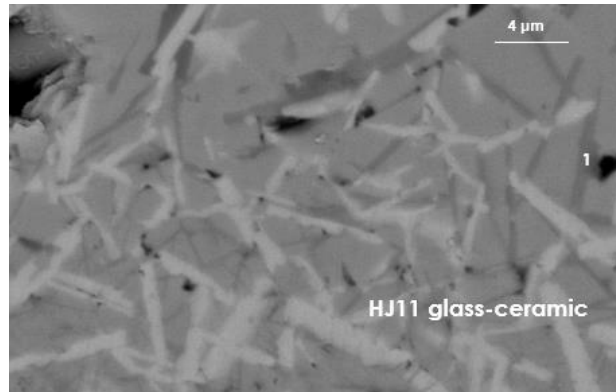
The composition detected in *Figure 4.16* refers to a white crystal containing O, Si and Ba, so it can be identified as barium silicate with slight amounts of Ca.



Elements (atomic %)	Point 1
O	66.75
Si	20.17
Ca	4.14
Ba	8.94

Figure 4.16: SEM and EDS of Crofer22APU/HJ11 glass-ceramic/Crofer22APU aged sample, collected close to the negative polarized interface at the air side.

EDS point number 1 in *Figure 4.17* detected a composition compatible with Celsian ( $\text{BaAl}_2\text{Si}_2\text{O}_8$ ), an undesired crystalline phase for these applications. Due to its polymorphism, this phase can show three different crystalline structures: metastable hexacelsian (CTE  $6.5\text{-}9 \cdot 10^{-6} \text{ K}^{-1}$ ), orthocelsian (CTE  $7\text{-}8 \cdot 10^{-6} \text{ K}^{-1}$ ) and monocelsian (CTE  $2\text{-}3 \cdot 10^{-6} \text{ K}^{-1}$ ). The formation of celsian (especially monocelsian, stable at low temperatures) may induce changes in a specific volume and lower the overall value of the CTE of sealant, thus generating high thermal stresses [18].



Elements (atomic %)	Point 1
O	63.4
Al	8.1
Si	19.9
Ca	1.2
Ba	7.3

Figure 4.17: SEM and EDS of Crofer22APU/HJ11 glass-ceramic/Crofer22APU sample after test G4, collected close to the positive polarized interface.

*Figure 4.18* and *Figure 4.19* suggest that the glass-ceramic joining has not any critical porosity or cracks induced by the aging test. Furthermore, Crofer22APU and plates and HJ11 show a perfect adhesion.

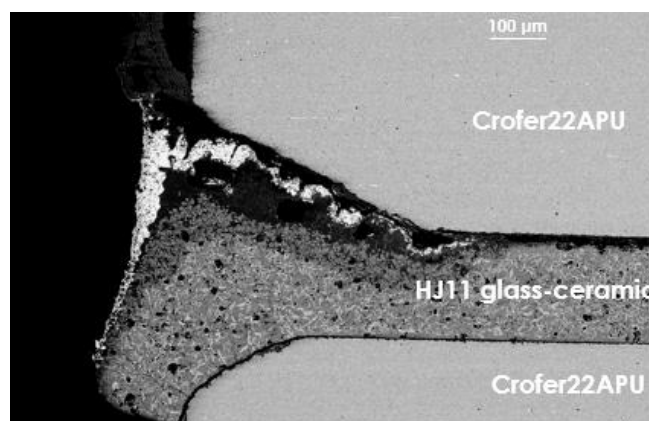


Figure 4.18: SEM image of a Crofer22APU/HJ11 glass-ceramic/Crofer22APU aged sample, air side.

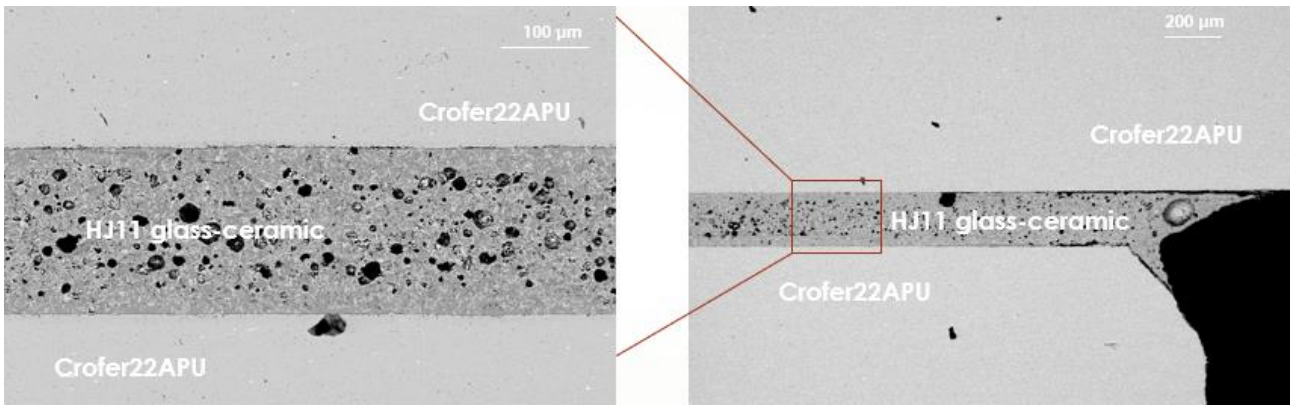


Figure 4.19: SEM images of a Crofer22APU/HJ11 glass-ceramic/Crofer22APU aged sample, fuel side.

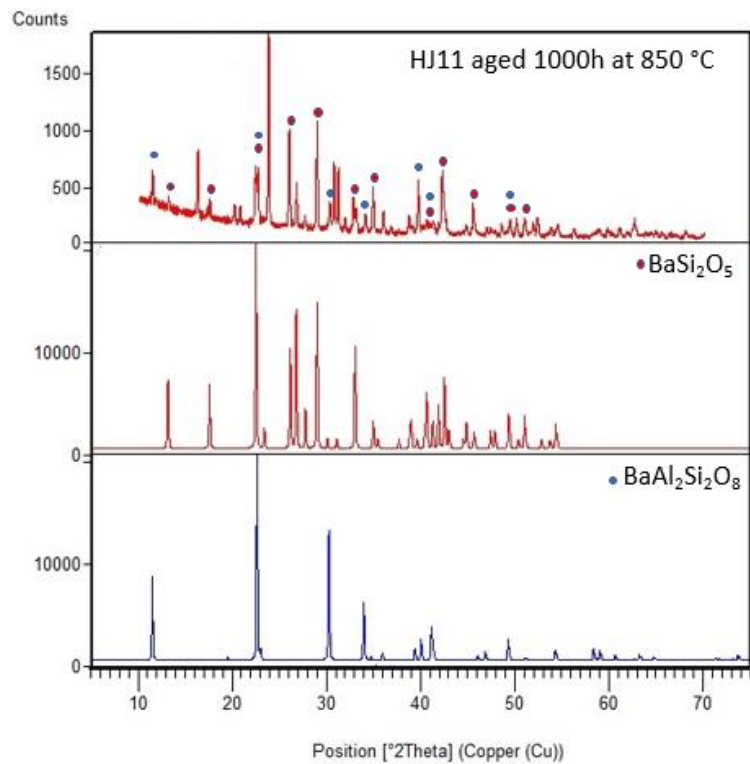


Figure 4.20: XRD analysis on the HJ11 powders.

In accordance with the EDS results (*Figure 4.15*, *Figure 4.16* and *Figure 4.17*), XRD analysis of HJ11 aged glass-ceramic, shown in *Figure 4.20*, detected the presence of slight amounts of celsian ( $\text{BaAl}_2\text{Si}_2\text{O}_8$ ) in addition to the sanbornite ( $\text{BaSi}_2\text{O}_5$ ), which is still the predominant crystalline phase. The new crystalline phase likely determined the overall CTE variation after the aging treatment detected by the dilatometry test.

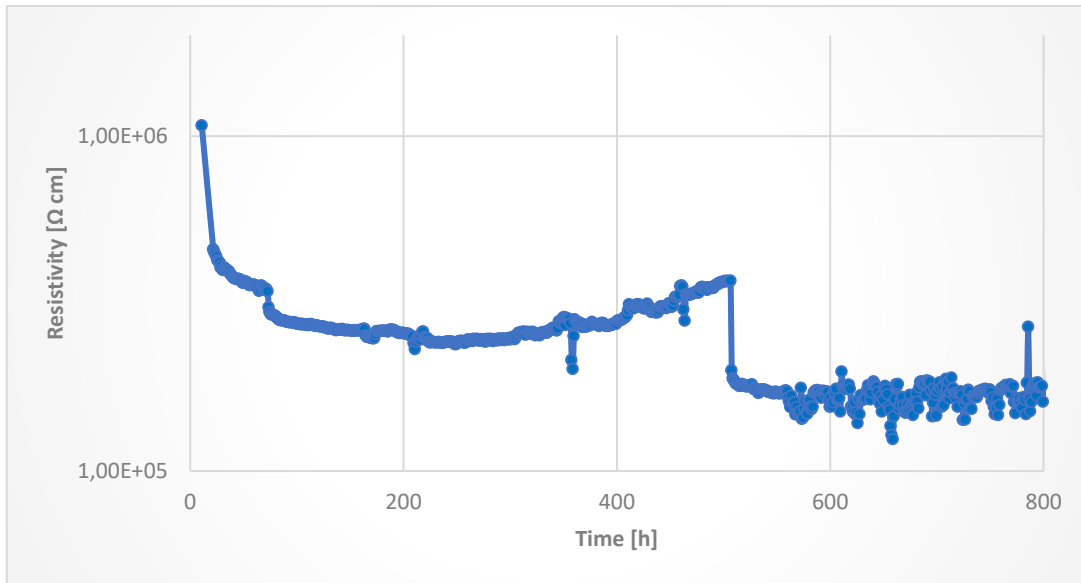


Figure 4.21: HJ11 resistivity curve.

In *Figure 4.21* the electrical resistivity of the HJ11 during the dual test is reported. After 1000h of aging at 850°C in dual atmosphere and under the application of a 1.6 V (test G4), the system demonstrated an electrical resistivity higher than  $10^5 \Omega \text{ cm}$ .

HJ26 and HJ27 samples were tested for 500h at 850 °C under the application of 1.6V. HJ26 was tested in air, whereas the HJ27 was tested in dual atmosphere. HJ26 joined samples were completely detached at the end of the test, suggesting a poor thermomechanical compatibility with the Crofer22APU substrate; on the contrary, Cofer22APU/HJ27 glass-ceramic/Crofer22APU joined samples were still sound.

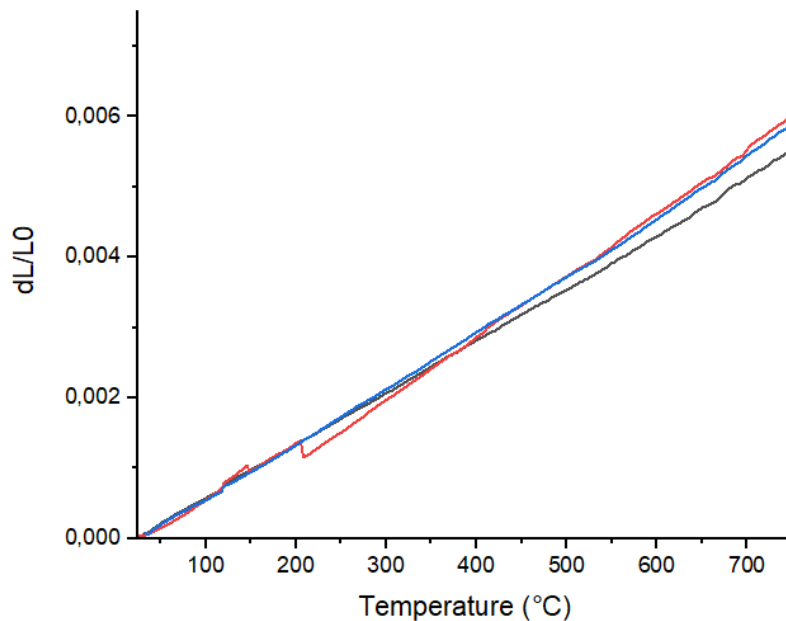
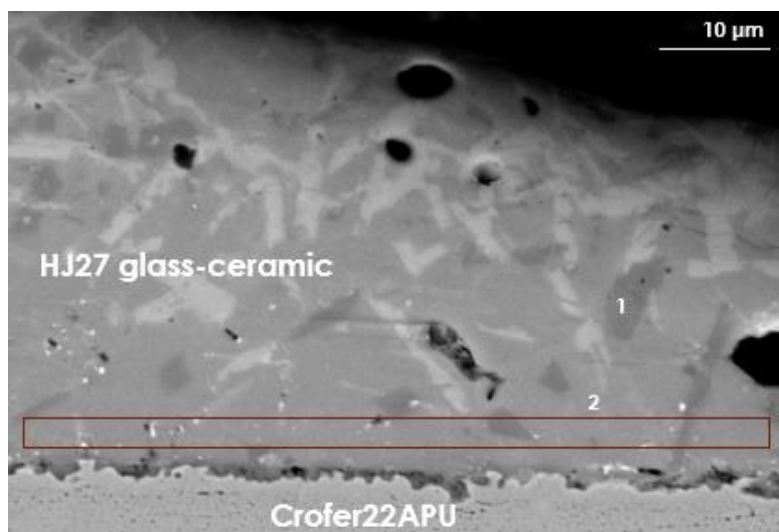


Figure 4.22: HJ27 glass-ceramic after test G6+G7 (blue), HJ27 glass-ceramic after test G6 (red) and HJ26 glass-ceramic after test G6 (black) dilatometry curves.

The CTEs of HJ26 and HJ27 aged glass-ceramics dramatically decreased after the aging. The dilatometry curves in *Figure 4.22* suggest that both the systems were completely refractory, thus excluding the presence of a residual glassy phase. HJ26 showed a value of ( $7.3 \cdot 10^{-6} \text{ K}^{-1}$ ), and this explains the detachment of the joining after the cooling down; on the contrary, despite of the unacceptable CTE ( $8 \cdot 10^{-6} \text{ K}^{-1}$ ), the HJ27 samples were still sound after the test.

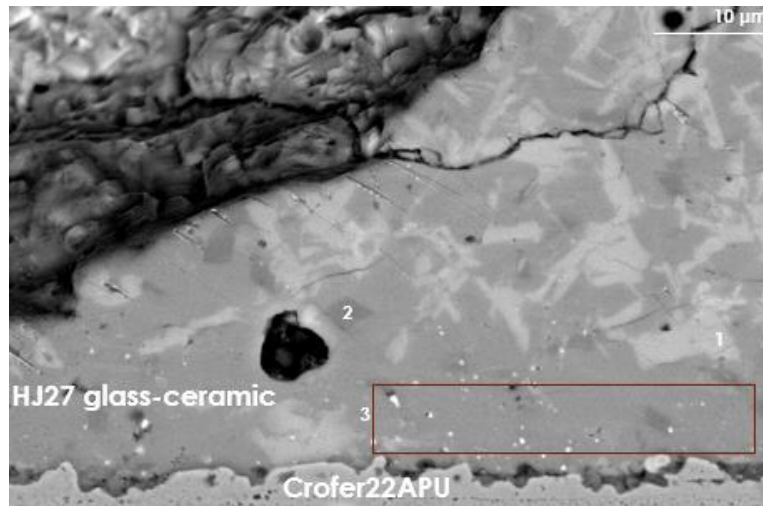
EDS analysis corresponding to point 1 in *Figure 4.23* was identified as a barium calcium orthosilicate crystal, a negligible crystalline phase which was not detected by the XRD analysis. In the second composition (point number 2), the amount of Cr and Fe detected in the residual amorphous phase close to the interface can be neglected, so during the aging no diffusion phenomena occurred.



Elements (atomic %)	Point 1	Point 2
<b>O</b>	46.40	57.99
<b>Al</b>		1.58
<b>Si</b>	25.56	21.30
<b>Ca</b>	17.42	
<b>Cr</b>		0.74
<b>Fe</b>		0.38
<b>Ga</b>		2.91
<b>Ba</b>	10.62	10.57

Figure 4.23: SEM and EDS on Crofer22APU/HJ26 glass-ceramic/Crofer22APU joined sample after test G6, collected in the negative polarized surface at the fuel side.

According to their compositions, point number 1 in *Figure 4.24* indicates a barium silicate crystal, while point number 2 refers to a barium calcium orthosilicate crystal, such as in *Figure 4.22*. In the last composition (point 3) the amount of Cr, Mn and Fe detected in the residual amorphous phase were negligible.



Elements (atomic %)	Point 1	Point 2	Point 3
O	58.10	55.67	60.35
Al			1.18
Si	27.66	23.05	20.67
Ca	0.35	12.44	3.71
Cr			1.10
Mn			0.55
Fe			0.34
Ga			2.23
Ba	13.89	8.84	9.87

Figure 4.24: SEM and EDS on Crofer22APU/HJ26 glass-ceramic/Crofer22APU joined sample after test G6, collected close to the negative polarized interface at the air side.

Figure 4.25 shows that in the Crofer22APU/HJ27 glass-ceramic/Crofer22APU no cracks are present. The white crystals in Figure 4.26, identified as barium silicate, represent the main crystalline phase of the system as confirmed also by the XRD analysis reported in Figure 4.27.

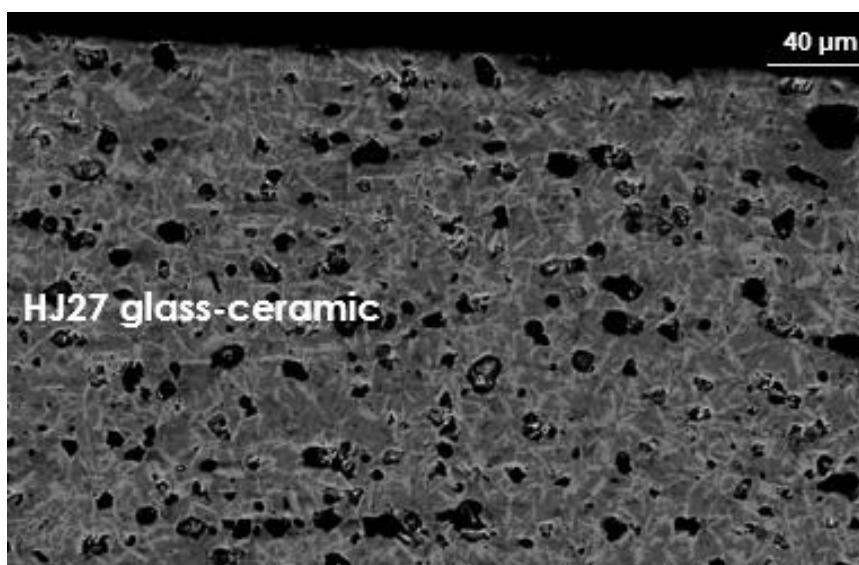


Figure: 4.25 SEM image of a Crofer22APU/HJ27 glass-ceramic/Crofer22APU joined sample after test G6, collected close to the negative polarized interface at the air side.

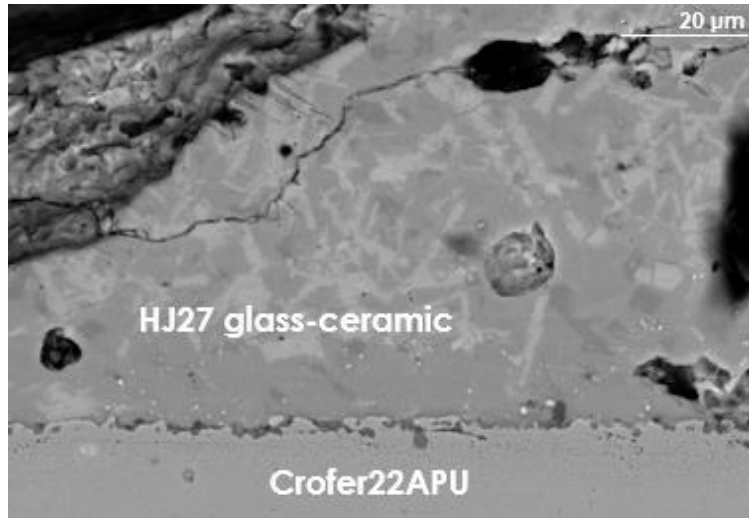


Figure 4.26: SEM image of a Crofer22APU/HJ27 glass-ceramic/Crofer22APU sample after test G6, collected close to the negative polarized interface.

EDS results reported in *Figure 4.23* and *Figure 4.24* for both HJ26 and HJ27 aged samples suggested the presence of  $\text{BaAl}_2\text{Si}_2\text{O}_8$  crystals, together with  $\text{BaSi}_2\text{O}_5$  crystal already detected for the as-joined powders. These results were confirmed by the XRD analysis (*Figure 4.27* and *Figure 4.28*). The undesired presence of this new crystalline phase after the aging test led to the CTEs reduction and to the formation of possible cracks. As alternative, HJ28 (discussed later in this chapter) was properly designed to avoid the formation of this detrimental crystalline phase.

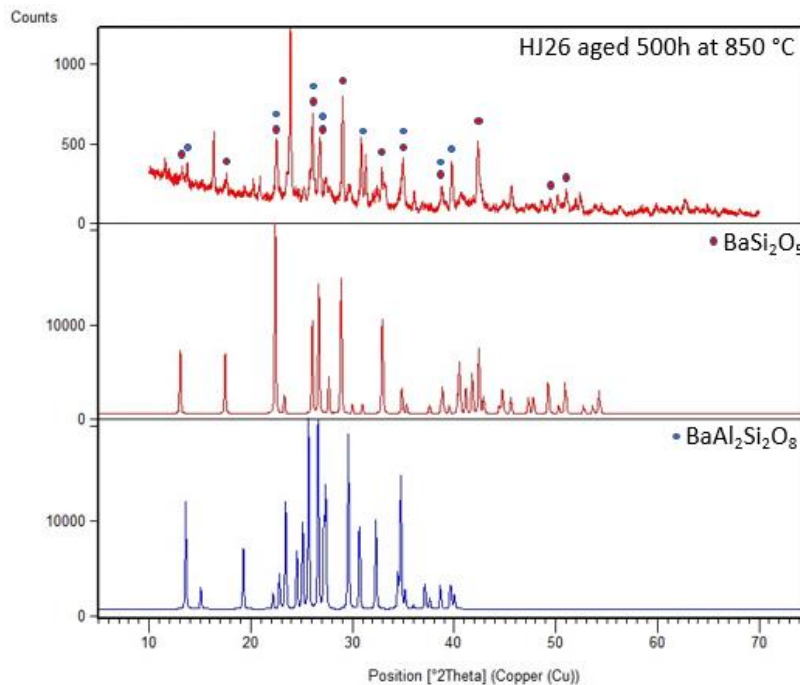


Figure 4.27: XRD analysis on the HJ26 aged powders.

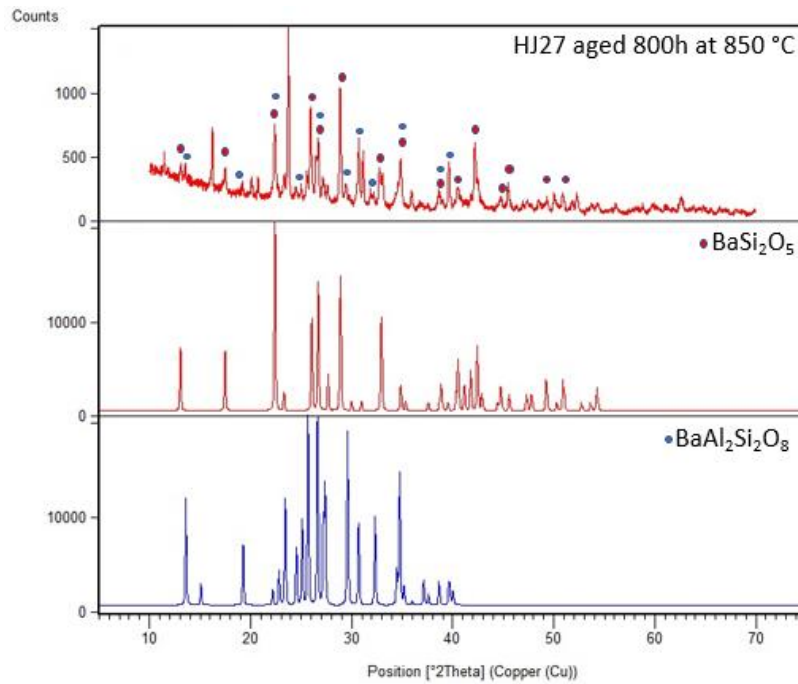


Figure 4.28: XRD analysis on the HJ27 aged powders.

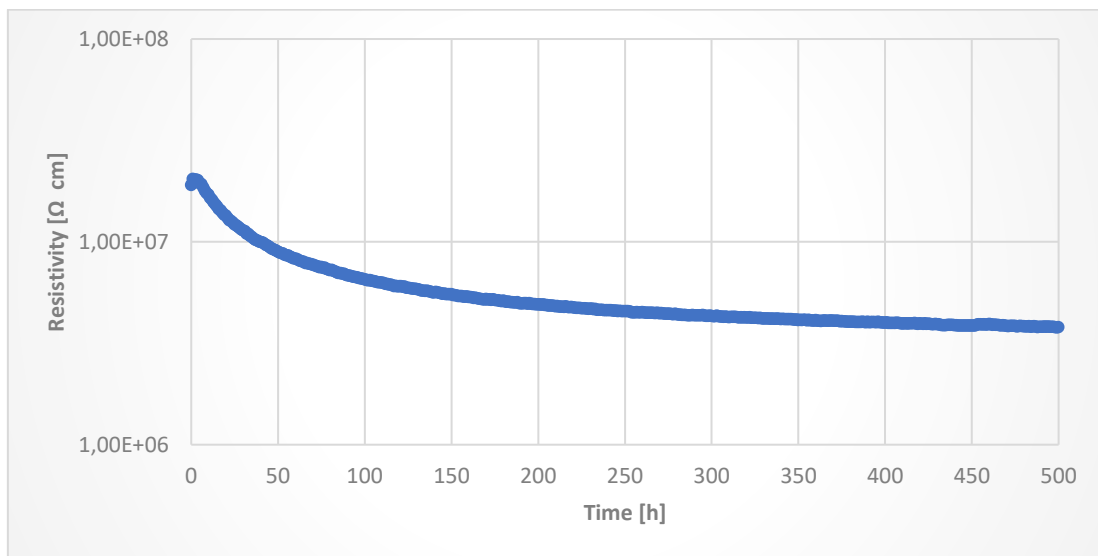


Figure 4.29: HJ27 electrical resistivity curve.

The electrical resistivity vs time of HJ27 glass-ceramic reported in *Figure 4.29* appears to be stable during all the duration of the test showing a slight continuous decrease.

Crofer22APU/HJ28 glass-ceramic/Crofer22APU joined samples and HJ28 glass-ceramic pellets were tested at 850 °C for 300h and they showed the following results.

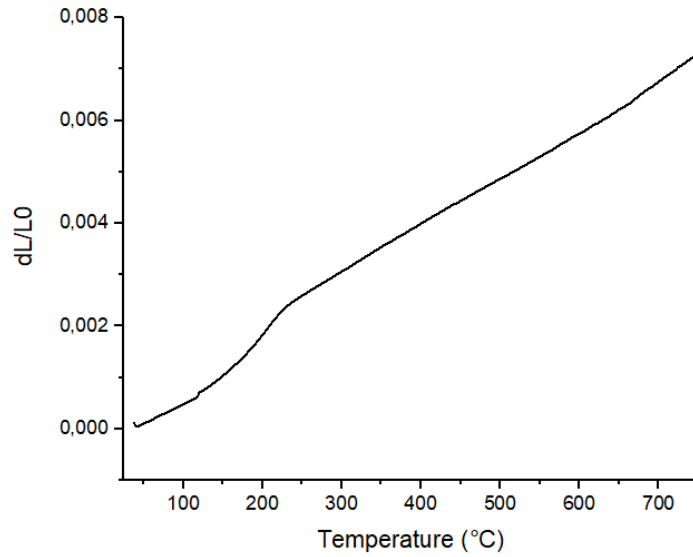
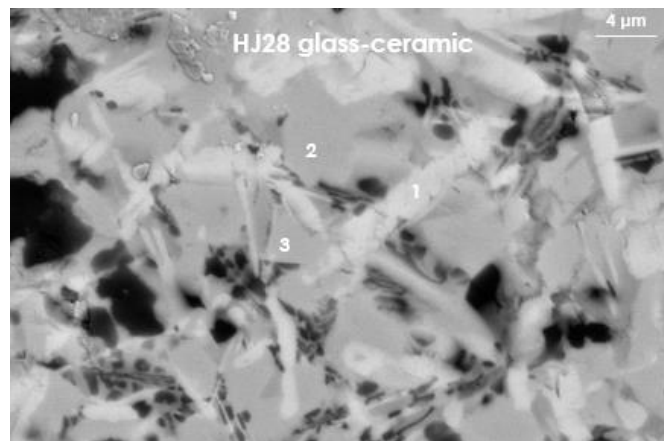


Figure 4.30: HJ28 glass-ceramic after test G7 dilatometry curve.

The thermal aging modified the structure of the glass-ceramic sealant, with the formation of crystalline phases which have increased the CTE from  $8.5 \cdot 10^{-6} \text{ K}^{-1}$  (as-joined) to  $9.1 \cdot 10^{-6} \text{ K}^{-1}$  (aged). The change in slope of the dilatometry curve of HJ28 aged glass-ceramic located in the range 220-260 °C (Figure 4.30) was due to the formation of cristobalite ( $\text{SiO}_2$ ). This phase was detected by the XRD analysis discussed below and reported in Figure 4.32. Cristobalite presents a phase transition around 240°C with strong volume change, affecting the CTE and representing an issue in sealing application [18, 19].

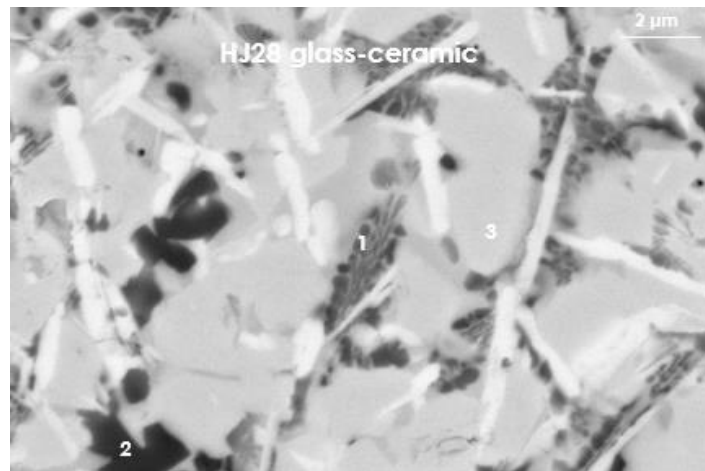
EDS point 1 in Figure 4.31 refers to a crystal containing O, Si and Ba mainly, coherent with the composition of sanbornite, while the other two points were collected on the residual amorphous phase.



Elements (atomic %)	Point 1	Point 2	Point 3
O	46.81	51.19	50.76
Al	0.94	0.95	1.54
Si	36.15	29.05	29.22
Ca	0.66	5.31	5.32
Ba	15.44	15.30	13.15

Figure 4.31: SEM and EDS on a Crofer22APU/HJ28 glass-ceramic/Crofer22APU joined sample after test G7, collected close to the positive polarized interface.

The first and the second compositions from the EDS analysis in *Figure 4.32* refer to black crystals containing mainly O and Si, identified as cristobalite with small traces of Ba and Al. Point number 3 was collected the residual amorphous phase.



Elements (atomic %)	Point 1	Point 2	Point 3
O	53.77	56.19	53.65
Al	5.23	0.51	1.07
Si	38.77	41.33	27.51
Ca	0.92	0.50	5.19
Ba	6.26	1.48	12.58

Figure 4.32: SEM and EDS on a Crofer22APU/HJ28 glass-ceramic/Crofer22APU joined sample after test G7, collected close to the positive polarized interface.

The amounts of Cr, Mn and Fe detected in the residual amorphous phase (*Figure 4.33a* and *Figure 4.33b*) are negligible, thus excluding diffusion phenomena.

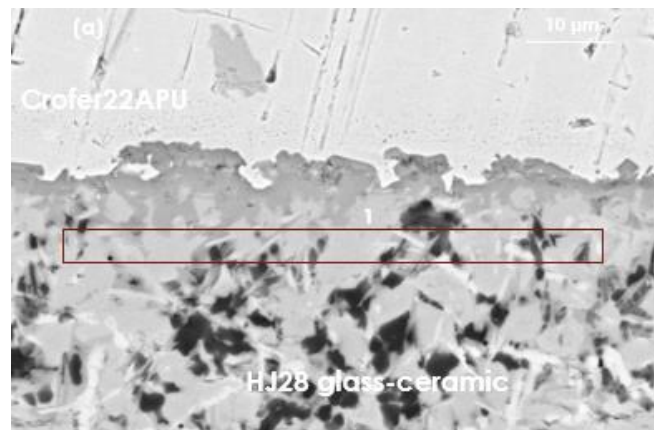
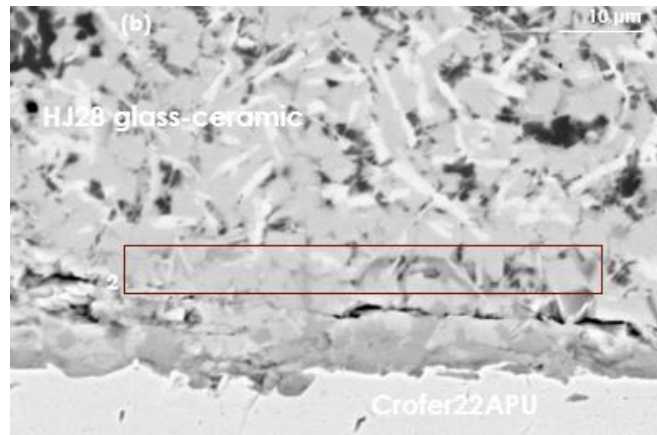


Figure 4.33a: SEM and EDS on a Crofer22APU/HJ28 glass-ceramic/Crofer22APU joined sample after test G7, collected close to the positive polarized interface at the air side.



Elements (atomic %)	Point 1	Point 2
O	52.58	54.55
Al	3.07	3.36
Si	29.98	27.20
Ca	2.98	3.29
Cr	0.33	0.63
Mn	0.54	0.49
Fe	0.25	
Ba	10.35	10.48

Figure 4.33b: SEM and EDS on a Crofer22APU/HJ28 glass-ceramic/Crofer22APU joined sample after test G7, collected close to the negative polarized interface at the air side.

Figure 4.34 shows a crack in the middle of the glass-ceramic sealant, originated as main consequence of low CTE of the system.

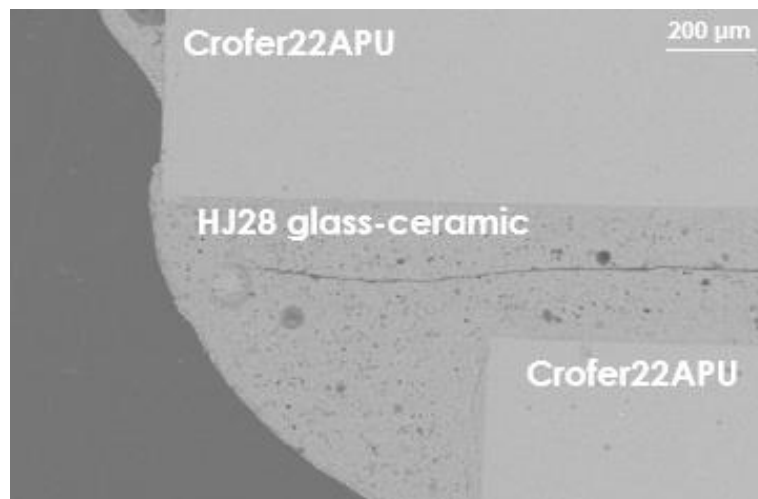


Figure 4.34: SEM image of a Crofer22APU/HJ28 glass-ceramic/Crofer22APU sample after test G7, air side.

As expected from the EDS analysis reported in Figure 4.31, Figure 4.32 and Figure 4.33 and from the dilatometric curve in Figure 4.30, the XRD analysis on the HJ28 aged glass-ceramic (Figure 4.36) pointed out the presence of two different crystalline phases: sanbornite ( $\text{BaSi}_2\text{O}_5$ ), which is the predominant phase and already detected in the as-joined glass-ceramic powders and a slight amount of cristobalite ( $\text{SiO}_2$ ). The evolution in the crystalline phases may be the reason of the CTE variation discussed above.

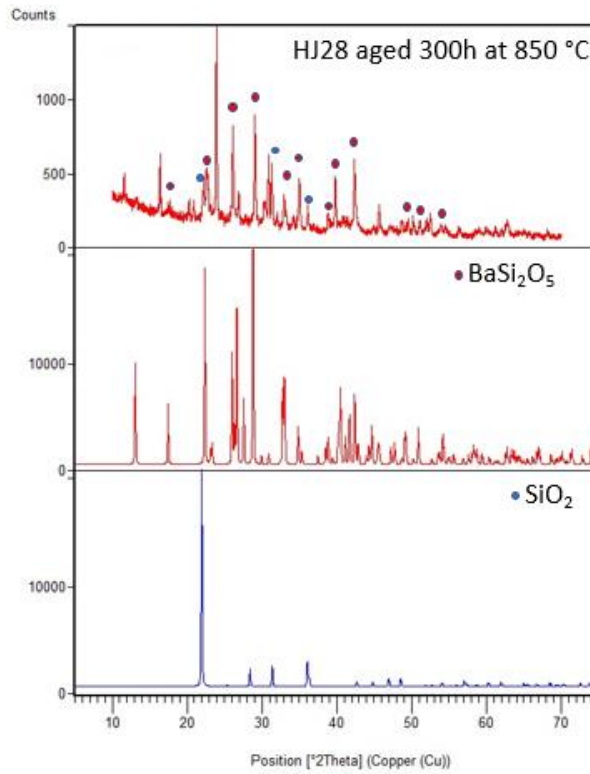


Figure 4.36: XRD analysis on HJ28 aged powders.

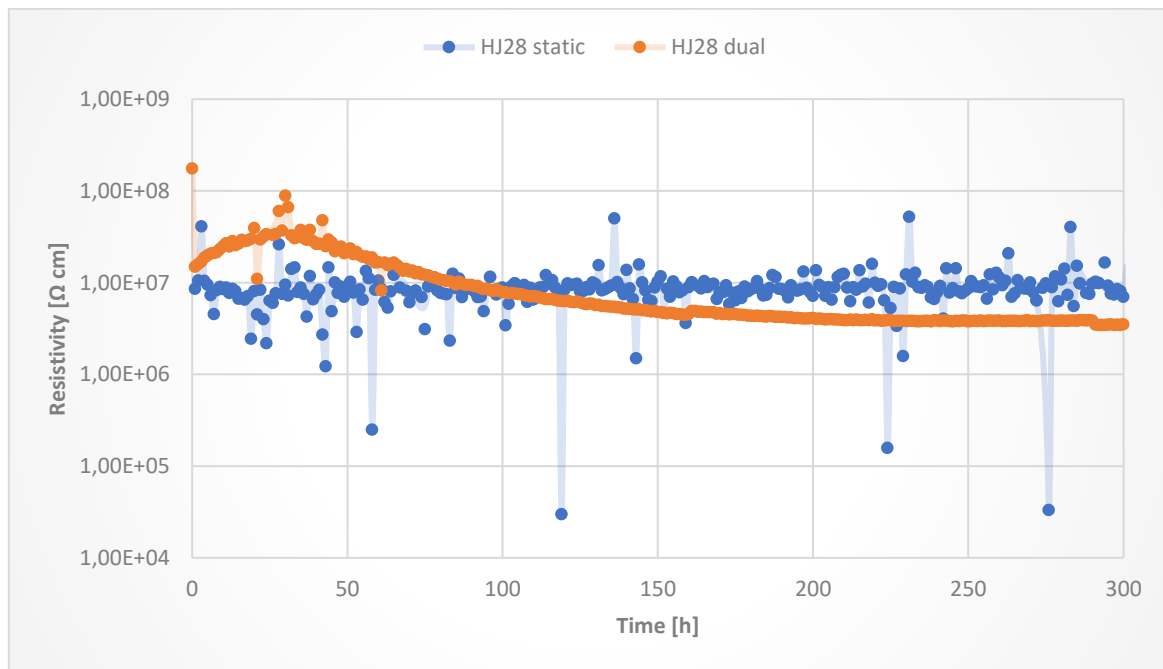


Figure 4.37: HJ28 resistivity curves.

HJ28 joined samples were tested for 300h at 850°C under the application of 1.6 V, both in dual atmosphere and static air (test G4). *Figure 4.37* shows the electrical resistivity curves recorded during the test G4. In both cases the resistivity behaviour of this system is considered suitable for SOCs sealing application excluding the presence of detrimental interaction between the sealant and the steel due to the application of an electrical load and to the presence of the dual atmosphere.

### 4.3. Summary of the results and discussions

In *Table 4.2* are summarized the results collected for each glass-ceramic sealant studied in the present work.:

Table 4.2: Overall results.

		Characteristic temperatures [°C]					CTE in the range 200-500 °C [ $10^{-6}$ K <sup>-1</sup> ]		
		T <sub>g</sub>	T <sub>s</sub>	T <sub>FS-TMS</sub>	T <sub>x</sub>	T <sub>P</sub>	As-casted glass	As-joined glass-ceramic	Aged glass-ceramic
<i>Sr-based systems</i>	<b>HJ14</b>	702	720	702-800	855	876	9,2	10,1	9,7
	<b>GS7</b>	695	726	708-827	886	909	10,3	10,6	9,2
<i>Ba-based systems</i>	<b>HJ11</b>	680	690	675-778	833	887	9,1	11,1	9,7
	<b>HJ26</b>	673	/	696-835	Not detected	Not detected	/	9,0	7,3
	<b>HJ27</b>	677	/	696-828	Not detected	Not detected	/	10,3	8,0
	<b>HJ28</b>	706	720	717-829	Not detected	Not detected	8,6	8,8	9,1

All the characteristic temperatures reported in *Table 4.2* are in line with the expectations suggested by the literature for borosilicate alumina-containing glasses and discussed in Section 2. The glass transition temperatures (T<sub>g</sub>) lay in the range 675-725 °C, with softening temperatures smaller than the cell operating temperatures thus allowing the glass to flow and to bond the materials and at the same time to mitigate thermal stresses or provide possible self-healing effect.

The dilatometry analyses show how the CTE of a system can evolve during the aging in simulated operating conditions, going from the as-joined glass-ceramic to the aged one. Despite their refractory nature, HJ11 and HJ14 represent the most promising compositions according to their CTEs after the thermal aging ( $9.7 \cdot 10^{-6}$  K<sup>-1</sup>), showing values in the range for rSOC applications. Both the XRD analyses and EDS results led to the identification of the main crystalline phases generated by the thermal treatments and involved in the CTEs variations of each systems:

- *Sr-based systems*: the joining thermal treatments led to the formation of the desired SrSiO<sub>3</sub> as main crystalline phase. This was reached thanks to a careful design of the starting glass composition. The crystallization of this phase allowed the tailoring of the CTE of the sealant in order to match the joined materials. GS7 composition was designed increasing the content of Al<sub>2</sub>O<sub>3</sub> and Ga<sub>2</sub>O<sub>3</sub> in comparison with HJ14. This was done to delay the crystallization temperature and to overcome the refractory nature of the HJ14. The main consequence of alumina addition was the formation of celsian (SrAl<sub>2</sub>Si<sub>2</sub>O<sub>8</sub>), which was detected after the thermal treatments and which led a CTE reduction in the sealant. This resulted in the failure of the joining Crofer22APU/GS7 glass-ceramic/Crofer22APU during the cooling down at the end of the long-term test. A possible future approach for Sr-based systems could be a new

composition similar to HJ14, having the same SiO<sub>2</sub>/SrO ratio and with the addition of Y<sub>2</sub>O<sub>3</sub> as additive;

- *Ba-based systems*: in all these systems sanbornite (BaSi<sub>2</sub>O<sub>5</sub>) was identified as the main crystalline phase after the joining treatment as well as after aging at 850°C. HJ26 and HJ27 compositions were derived from HJ11 in order to increase the glassy amorphous phase. SiO<sub>2</sub>/BaO ratio was maintained the same, but Ga<sub>2</sub>O<sub>3</sub> and Al<sub>2</sub>O<sub>3</sub> were added to obtain higher crystallization temperatures. However, thermal treatments on HJ26 and HJ27 led to the formation of celsian (BaAl<sub>2</sub>Si<sub>2</sub>O<sub>8</sub>) as secondary crystalline phase due to the Al<sub>2</sub>O<sub>3</sub> content. Celsian is an unwanted phase for SOCs applications due to its phase transition and formation of monoclinic structure with low CTE. In order to avoid the formation of celsian, HJ28 composition was designed by varying the SiO<sub>2</sub>/BaO ratio respect to the previous systems and adding Y<sub>2</sub>O<sub>3</sub>. On the other hand, cristobalite (SiO<sub>2</sub>) was detected after the aging at 850°C. This phase can be detrimental as well due to its phase transition at low temperatures with a strong volume change. This can lead to the formation of crack surrounding SiO<sub>2</sub> crystals during thermal cycling.

All the investigated composition demonstrated good performance if joined with both 3YSZ and Crofer22APU under the morphological point of view. SEM and EDS images confirm the absence of cracks or delamination phenomena at the interface. Furthermore, a low level of closed porosity was found, confirming the proper choice of the joining thermal treatments. All the investigated sealants were found to be thermo-chemical compatible with the joined materials, indeed no signs of detrimental reaction between the sealants and the metallic counterparts were detected. The same can be said for long term aging periods in relevant conditions. No signs of detrimental electrochemical reactions were found despite the application of 1.6V for long periods at 850°C. In addition, also their exposition to a dual atmosphere did not produce detrimental reactions/interactions. The resistivity values recorded for all the compositions were always higher than the value of 10<sup>4</sup> Ω cm, considered as the minimum to avoid current shunting. Furthermore, the electric behaviour of the sealant did not suggest any electrochemical interaction between the glass-ceramics and the steel.

However, many of the composition reported here still need to be improved under the thermochemical point of view. In some of them the aging led to the formation of detrimental phases with low CTE thus lowering the overall CTE of the sealant below the minimum required for SOCs applications.

## 5. Mechanical tests on glass-ceramic sealants

The structural integrity of the sealant material is critical for the reliability of solid oxide fuel/electrolysis stacks. In SOC working conditions, sealants can be exposed to a combination of tensile and shear loads that could lead to failure.

A promising technique to evaluate the mechanical strength of glass-ceramic sealants is the torsion test on joined metal/sealant/metal hourglass shaped samples. With this technique it is possible to evaluate the pure shear strength of joining materials. The shear strength of brittle joining materials is derived from the maximum torque applied during the test (at which fracture occurs) and it is calculated as follow [25]:

$$\tau = \frac{T \cdot R}{J} \quad \text{Eq. 5.1}$$

where  $T$  is the maximum torque applied on the sample,  $R$  is radius of the circular joined area (*Figure 5.1*) and  $J$  is the polar moment of inertia of the sample joined area, calculated with the formula:

$$J = \frac{1}{2} \pi R^4 \quad \text{Eq. 5.2}$$

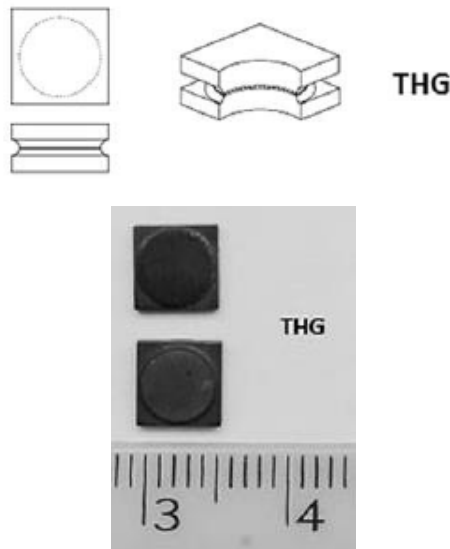


Figure 5.1: Hourglass shaped sample (THG5) for torsional test; substrates are made of Crofer22APU steel and the 5mm diameter circular area is joined by the glass-ceramic system [26].

Some studies [25, 26] demonstrated that the pure shear strength of a glass-ceramic sealant can be properly enhanced by the addition of fibers or particles in the glass powder before the joining thermal process. Several torsion tests were performed on a BaO-CaO-SiO<sub>2</sub> based glass (like the HJ11) enriched with YSZ powders, YSZ fibers, Ag powders, Ni particles, Ni-Cr particles or gadolinium doped ceria (CGO) powders [25], aiming to identify which is the best solution for improving the mechanical shear strength. The main results are reported in *Table 5.1*.

Table 5.1 Thermal characterization of a BaO-CaO-SiO<sub>2</sub> glass, labelled as H, after the addition of different fibers or particles for the mechanical enhancement. The synthesis process was performed at 850 °C at 2 °C/min, while the ageing process was performed at 850 °C for 500h [25].

Composite	Softening point (°C) (as sintered)	CTE [ $10^{-6} \text{ K}^{-1}$ ] (200-600°C)	
		Sintered	Aged
Glass H	605	9.6	8.1
Glass H + 10 wt.-% Ni	600	10.6	8.9
Glass H + 20 wt.-% Ni	610	10.8	9.8
Glass H + 10 wt.-% Ni-Cr	615	10.6	9.2
Glass H + 20 wt.-% Ni-Cr	635	10.6	not measured
Glass H + 20 wt.-% Ag	570	11.5	8.8
Glass H + 13 wt.-% YSZ fibers	630	9.3	9.3
Glass H + 10 wt.-% CGO10	600	10.2	8.8
Glass H + 20 wt.-% CGO10	605	10.2	9.3
Glass H + 10 wt.-% CGO20	600	10.2	8.7
Glass H + 20 wt.-% CGO20	605	10.2	9.5

The torsion tests described in *Table 5.1* were performed at room temperature on hourglass shaped joined samples (THG5), both as-joined and aged at 850 °C for 500h.

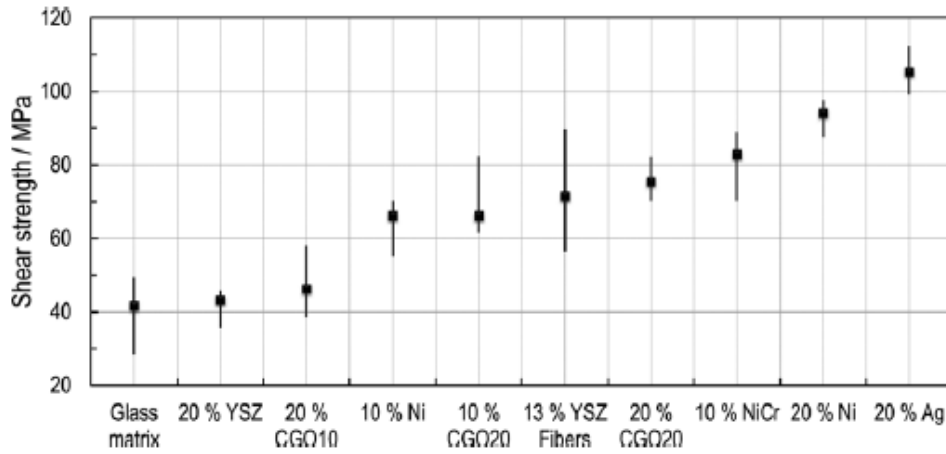


Figure 5.2: shear strength results for as-joined samples [25].

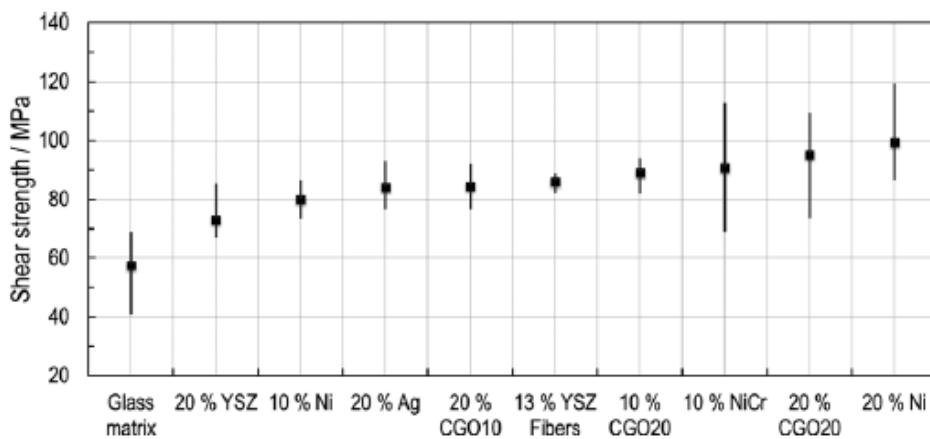


Figure 5.3: shear strength results for aged samples [25].

Figure 5.2 shows that the as-joined samples obtained with the selected glass matrix have shear strength values with relatively high scattered data, with an average of 40 MPa. The same joined samples after ageing seems to have a slight improvement of the maximum shear strength (around 58 MPa), as shown in Figure 5.3. Both Figure 5.2 and Figure 5.3 suggest that the as-joined and aged samples processed with filler addition have a better shear strength, which means that the addition of fibers or particles is a suitable solution to improve the mechanical properties. The results clearly show that the most promising solutions are obtained with the addition of Ni, Ni-Cr or CGO in different quantities in the glass matrix.

The literature [26] provides alternative mechanical tests in terms of samples shape adopted, temperatures and strength evaluated. The THG 5 is often compared with the THG 25, which is 5 times higher in all dimensions, or with the TDHG, which has a ring shaped joined area (Figure 5.4, 5mm of external diameter and 3mm of internal diameter) or with a cross-bonded sample (Figure 5.5).

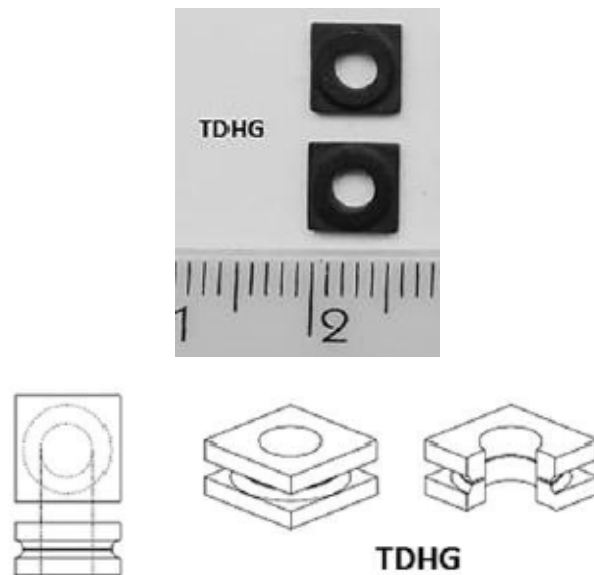


Figure 5.4: Hourglass Crofer 22 APU shaped sample (TDHG) for torsion test; the ring area (5mm of external diameter and 3mm of internal diameter) is joined by the glass-ceramic system [26].

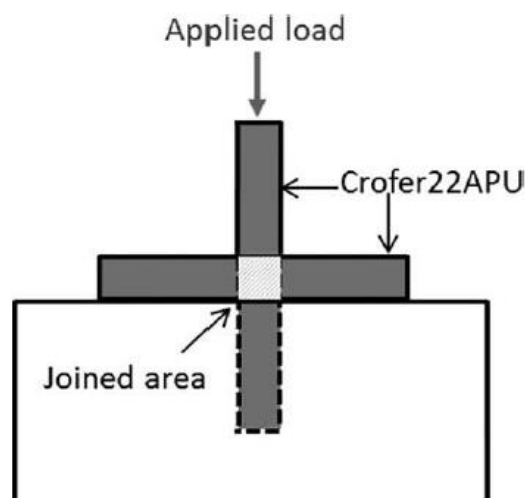


Figure 5.5: Cross-bonded sample 4x4mm for ISO 13124 standard tests [26].

The mechanical tests performed on THG25 and TDHG are exactly the same already described for the THG5; for TDHG the difference is the definition of the polar moment of inertia for the evaluation of the pure shear strength:

$$J = \frac{1}{2}\pi(R_e^4 - R_i^4) \quad \text{Eq. 5.3}$$

The cross-bonded samples are adopted in the ISO 13124 standard test, where both the tensile and shear strength at the glass-ceramic-metal interface are evaluated.

In this MSc thesis, Crofer22APU steel hourglass shaped samples were joined using the glass-ceramic sealant labelled HJ11 and then tested in torsion. The samples for torsion tests were prepared by depositing a slurry, made of HJ11 glass powders dispersed in ethanol, on the circular area of each THG5 hourglass (*Figure 5.1*); after the slurry deposition, the samples were submitted to the joining thermal treatment already described in section 3.

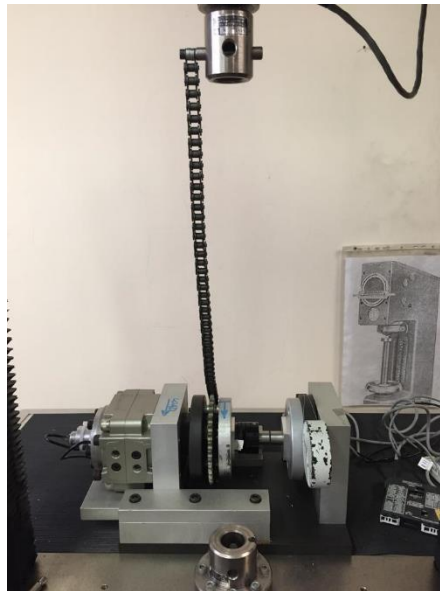


Figure 5.6: Torsion machine used to test the THG5 samples.

The torsion tests have been performed with the experimental apparatus shown in *Figure 5.26*; joined samples are inserted between two grips, one is fixed (right) and one is able to rotate (left) when dragged by a chain, which is linked to a tensile machine moving at a constant speed of 5 mm/min. The device detects the angular variation of the rotating grip and the resistant force applied on the fixed grip, computing the torque applied on the sample until its breakage. At the end of the test, a graph with torque as a function of angular variation is obtained (*Figure 5.7*). The point of interest is the maximum torque applied, from which it's possible to evaluate the maximum shear strength with *Eq. 5.3*. The glass-ceramic system at room temperature has a brittle behaviour, so the fracture always occurs in the elastic region, as suggested by curves in the *Figure 5.7*.

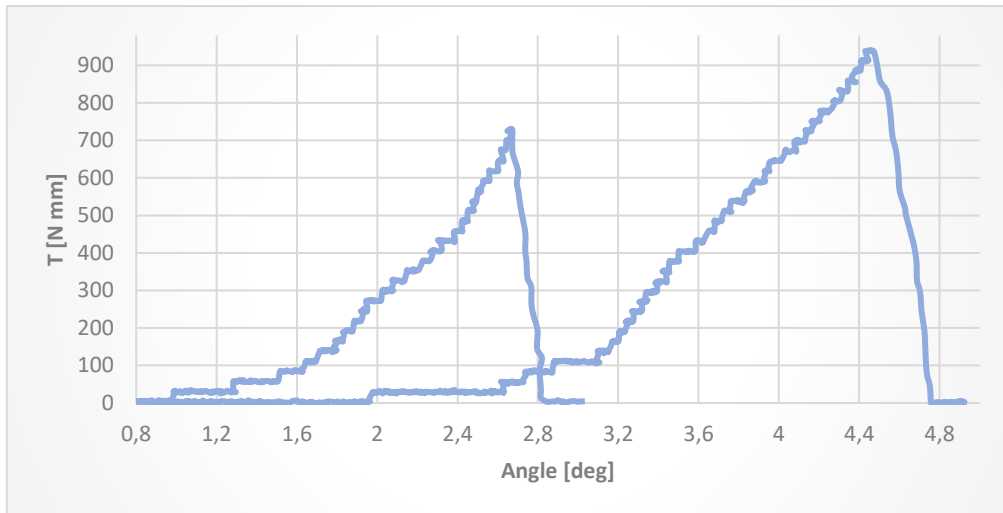


Figure 5.7: example of torque-angle curves obtained at the end of torsion test at room temperature.

Generally, two types/modes of fracture after a torsion test are possible, i. e. the adhesive fracture, occurring at the interface between the glass-ceramic sealant and the Crofer oxide layer, and the cohesive fracture, occurring inside the glass-ceramic sealant. For all tested samples it was impossible to identify a single type of fracture behaviour, because the hourglass surfaces after the tests showed the presence of different fracture modes.

Four batches labelled as A, B, E and F were produced and tested. The thickness of samples was measured before and after the joining process, and the glass-ceramic joining material thickness were measured by difference for a further analysis, aiming to identify possible links between the joint thickness and the detected shear strength.

A1, A2 and A3, which have shear strength values smaller than 40 MPa (*Table 5.2*), seem to have a “cone shaped” type of fracture, as suggested by the *Figure 5.8*; the fracture has started to propagate from the external surface at the glass-ceramic sealant/oxide layer interface, then it continued through the glass layer to reach the top of the cone, where the oxide layer was detached from the steel. B3 and B4 have higher shear strength values (*Table 5.3*), and they show a mixed adhesive/cohesive type of fracture, with glass-ceramic sealant present on both sides and also adhesive failure at the interface between Crofer steel and his oxide scale (*Figure 5.9*). This behaviour suggests that the failure has occurred at the interface between the Crofer and the oxide layer as well as inside the glass-ceramic material, thus leading to a mixed adhesive/cohesive failure (even if it is not possible to determine the exact origin of the fracture). *Figure 5.10* and *Figure 5.11* suggest that in 7 out of 10 samples belonging to batches E and F the fracture is still mixed, with the glass-ceramic present on both samples surfaces and with corresponding shear strength values higher than 40 MPa (*Table 5.4* and *Table 5.5*). While E2, F2 and F5 are the exceptions, with cone-shaped fracture surfaces similar to those of batch A and lower shear strength values.

The fracture surfaces of samples after torsion test are shown in *Figure 5.8* to *5.11* and the shear strength results are reported in *Table 5.2* to *5.5*.

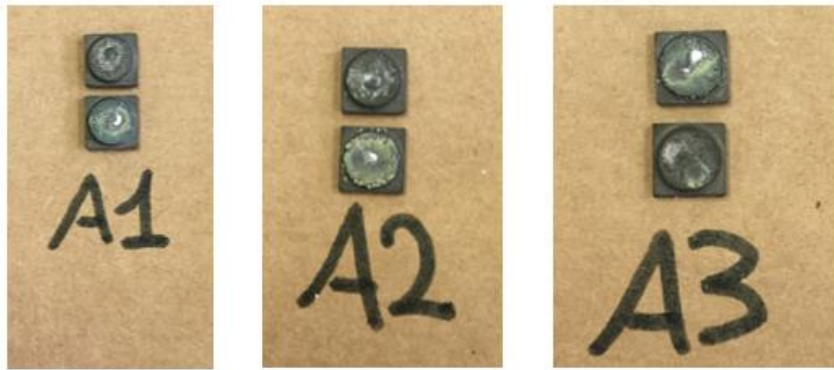


Figure 5.8: Fracture surfaces of samples belonging to batch A.

Sample	Type	Joint thickness [ $\mu\text{m}$ ]	$\tau$ [MPa]
A1	THG 5	/	29,8
A2	THG 5	/	39,4
A3	THG 5	/	28,7

Table 5.2: Results for samples belonging to batch A.



Figure 5.9: Fracture surfaces of samples belonging to batch B.

Sample	Type	Joint thickness [ $\mu\text{m}$ ]	$\tau$ [MPa]
B3	THG 5	160	40,6
B4	THG 5	50	60,2

Table 5.3: Results for samples belonging to batch B.



Figure 5.10: Fracture surfaces of samples belonging to batch E.

Sample	Type	Joint thickness [ $\mu\text{m}$ ]	$\tau$ [MPa]
E1	THG 5	190	46,0
E2	THG 5	60	23,2
E3	THG 5	120	55,7
E4	THG 5	230	51,4
E5	THG 5	210	67,4

Table 5.4: Results for samples belonging to batch E.



Figure 5.11: Fracture surfaces of samples belonging to batch F.

Sample	Type	Joint thickness [ $\mu\text{m}$ ]	$\tau$ [MPa]
F1	THG 5	90	34,1
F2	THG 5	200	29,7
F3	THG 5	220	38,3
F4	THG 5	130	48,2
F5	THG 5	230	24,3

Table 5.5: Results for samples belonging to batch F.

The torsion tests showed high scattered results in terms of shear strength values. The values range from a maximum of 67 MPa to a minimum of 23 MPa, with an average of  $41 \pm 13$  MPa on a total of 15 tests.

C1, D1 and D2 were tested in Germany at FZJ Julich, at room temperature, and the results are in line with those obtained at the Politecnico of Turin, as shown in *Table 5.6*. C4 has failed during the test preparation, while C1 shows a completely adhesive failure that occurred at the glass-ceramic sealant/oxide layer interface, this type of failure is a result of wrong sample preparation and the value should be discarded (*Figure 5.12*). On the contrary, D1 and D2 have mixed fracture surfaces with the glass-ceramic present on both sides (*Figure 5.12*), to whom correspond higher shear strength values.

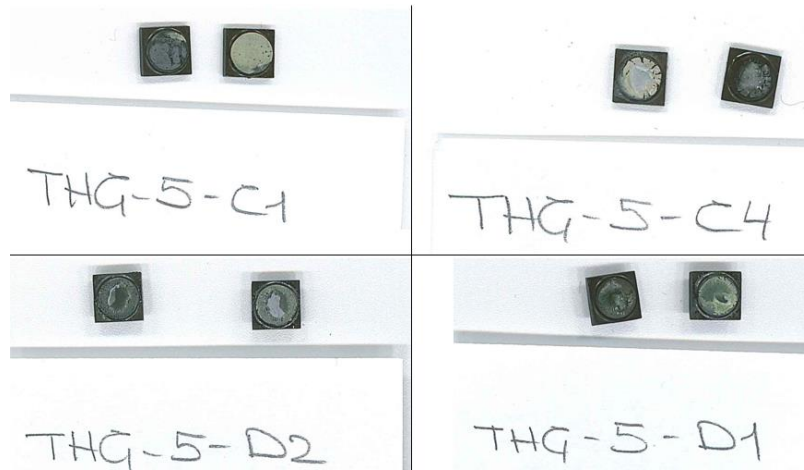


Figure 5.12: Fracture surfaces of THG5 samples tested in Germany, belonging to batch C and D.

Sample	Type	Joint thickness [ $\mu\text{m}$ ]	$\tau$ [MPa]
C1	THG 5	150	15,6
C4	THG 5	270	Failed
D1	THG 5	70	53,7
D2	THG 5	90	38,9

Table 5.6: Results for THG5 samples tested in Germany, belonging to batch F.

THG 25 are hourglass shaped samples having a joint circular area of 25 mm. C1 and C2 (THG 25) were also tested in Germany at room temperature and showed mixed adhesive/cohesive fracture surfaces (*Figure 5.13*). The corresponding shear strength values shown in *Table 5.7* are in line with those obtained for the THG 5 with the same fracture behaviour. As expected, these results demonstrate that the mechanical properties of the glass-ceramic joined samples do not depend on their dimensions. These results are in line with those of previous studies [26].

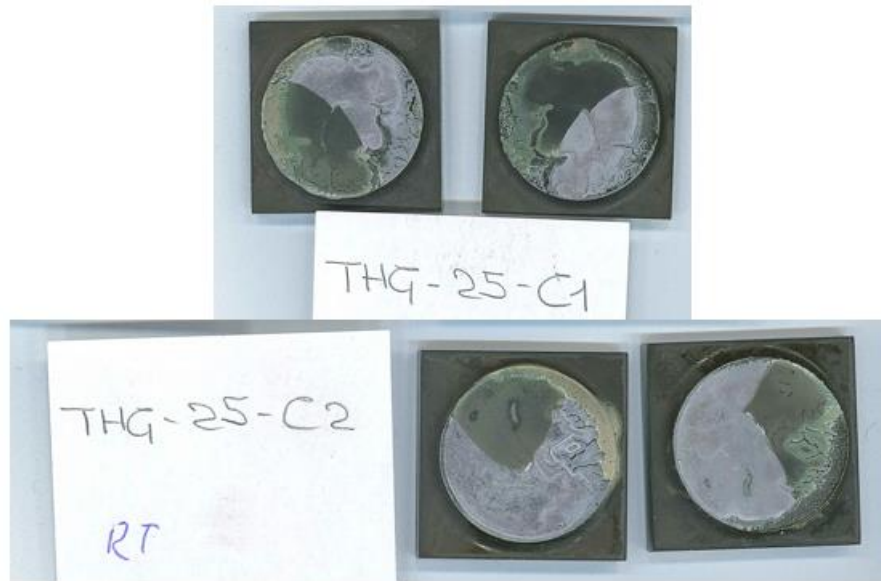


Figure 5.13: Fracture surfaces of THG 25 samples belonging to batch C.

Sample	Type	Joint thickness [ $\mu\text{m}$ ]	$\tau$ [MPa]
C1	THG 25	Not available	55,4
C2	THG 25	Not available	55

Table 5.7: Results for THG 25 samples belonging to batch C.

Further torsion tests were performed in Germany on THG25 joined samples at 800 °C, to evaluate the mechanical strength of the glass-ceramic sealant close to the operating temperature of the cell (for the shear strength calculation reported in *Table 5.8* only the maximum value of the time-torque curve was considered, not taking into account the difference between the elastic and plastic deformation). An average shear strength of  $10 \pm 5$  MPa was obtained on 3 samples tested at 800 °C. This temperature is close to the softening temperature of the glass matrix and well above the glass transition temperature (690 °C); for this reason, the sealant exhibited the viscous flow of the residual glassy phase. D1 and E2 showed an adhesive type of failure (*Figure 5.14*), with related lower shear strength values, while E1 had a mixed adhesive/cohesive failure, with glass-ceramic sealant present on both sides and partial detachment of the steel oxide scale (*Figure 5.14*). The time-torque curve for sample E1 is shown in *Figure 5.15*; with respect to the graph reported in *Figure 5.7*, this curve suggests that the sealant had no more a completely brittle behaviour, because also an area of plastic deformation is clearly visible in the graph.

The viscoelastic behaviour of residual glass at high temperatures leads to a reduced brittleness of the partially crystallized HJ11 glass-ceramic



Figure 5.14: Fracture surfaces of THG 25 samples belonging to batches D and E.

Sample	Type	Test temperature [° C]	Joint thickness [ $\mu\text{m}$ ]	$\tau$ [MPa]
D1	THG 25	800	250	7.2
E1	THG 25	800	220	15.4
E2	THG 25	800	250	7.2

Table 5.8: Results for THG 25 samples belonging to batches D and E.

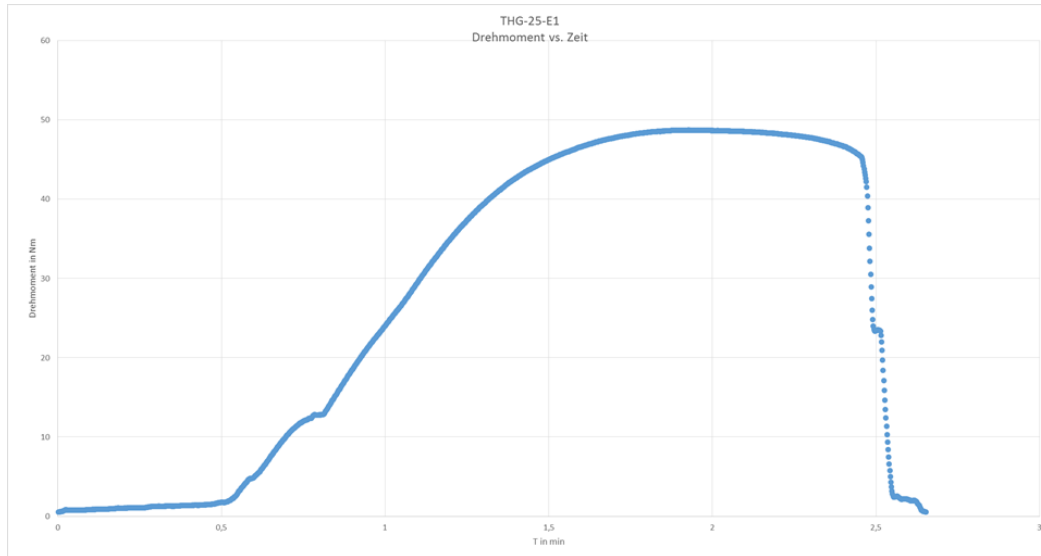


Figure 5.15: Time-torque curve for sample E1 tested at 800 °C.

It's statistically proved that a cone-shaped fracture type was detected for samples with shear strength smaller than 30 MPa. This type of failure is related to some defects, likely due to the slurry deposition method, so these values were discarded. For shear strength values higher than 40 MPa, a mixed fracture mode was observed, with the glass-ceramic sealant present on both joined surfaces and with areas of oxide layer detachment. The average shear strength values for THG 5 and THG 25 tested both at room and high temperature are presented in *Table 5.9*. For the evaluation of the average shear strength of THG 5 and THG 25 samples tested at room temperature, only samples with mixed adhesive/cohesive failure were considered.

Table 5.9: Average shear strength and standard deviation for samples with adhesive/cohesive fracture.

Sample	Test temperature [°C]	Average shear strength [MPa]
THG 5	R. T.	49 ± 10
THG 25	R. T.	55 ± 1
THG 25	800	10 ± 5

Torsion tests on Crofer22APU/HJ11 glass-ceramic /Crofer22APU were performed on both THG5 and THG25 hourglass samples. The average value for the THG5 configuration was found to be 49 ± 10 MPa, while for the THG25 configuration a value of 55 ± 1 MPa was obtained (*Table 5.9*). These tests demonstrated that the shear strength is independent from the joined area dimension. The proposed torsion test configuration can be considered a promising method to measure the pure shear strength of glass ceramic joined steel samples to be used in SOCs.

The partially cohesive fracture surface after torsion tests confirmed the very good adhesion and interface strength between the HJ11 glass-ceramic sealant and the Crofer22APU, as expected and likely due the high wettability of this glass ceramic sealant on the Crofer22APU substrate discussed in Section 3 and Section 4.

In THG 25 samples tested at 800 °C the residual amorphous phase had a viscoelastic nature which reduced the brittleness of the glass-ceramic sealants, as shown in *Figure 5.15*. As a consequence, the mechanical properties decreased and an average shear strength values of  $10 \pm 5$  MPa was obtained for these samples.

Further investigations on THG 25 samples joined at the Politecnico of Turin will be carried out at FZJ in Germany with torsion tests both at room and high temperature to improve the statistical data of the average shear strength. At the same time, high temperature torsion tests (i. e. 800°C) will be performed on THG 5 samples to check the joined area-shear strength correlation at temperature where sealant exhibits a viscoelastic behaviour.

## Conclusions and future perspectives

The obtained results can be summarised as follows:

- Among the SrO containing glasses, the HJ14 glass-ceramic, coupled with Crofer22APU) showed an optimal electrical resistivity during 1000h of test in dual atmosphere and under the application of 1.6 V. Despite a slight decrease during the test, the electrical resistivity values were always in the range  $10^5$ - $10^6$   $\Omega$  cm, which are acceptable in a SOC stack and considerably higher than the limit to avoid current shunting. HJ14 glass-ceramic showed a very good glass-ceramic stability and an excellent compatibility with the Crofer22APU, both at the cathodically and anodically polarised interface. No Cr diffusion phenomena occurred, and no strontium chromate formation was detected neither at the three-phase boundary nor at the interface.

Further research should be undertaken to investigate the possibility of increasing the amount of residual glassy phase in the HJ14 composition.

- Considering BaO containing compositions, two compositions, labelled as HJ11 and HJ28 demonstrated very interesting properties in terms of electrical resistivity and capability to avoid the formation of barium chromate. In particular, the HJ11 glass-ceramic joined samples did not show any critical porosity or cracks induced by the aging test and no evidence of Ba-chromate formation was found; slight amounts of celsian ( $\text{BaAl}_2\text{Si}_2\text{O}_8$ ) in addition to the sanbornite ( $\text{BaSi}_2\text{O}_5$ ) were detected, determining a slight decrease of the overall CTE. HJ28 system demonstrated an excellent stability concerning the electrical resistivity values over time ( $10^6$   $\Omega$  cm), but cristobalite was also detected after 1000 hours of test at 850°C.

Concerning Bao containing systems, further studies, which take these variables into account, will need to be undertaken, in order to minimize the presence of celsian and cristobalite while maintaining proper balance between the silica and barium oxide content.

Crofer22APU/HJ11/Crofer22APU hour glass samples were tested in torsion in order to determine the shear strength of the glass-ceramic joining, both at RT and 800°C. Average shear strength values of  $44 \pm 10$  MPa were obtained for THG 5 joined samples tested at room temperature (comparable to other Ba –silicate systems in the literature), while  $55 \pm 1$  MPa and  $10 \pm 5$  MPa were obtained respectively for THG 25 samples tested at room and high temperature. The proposed torsion test configuration can be considered a promising method to measure the pure shear strength of glass ceramic joined steel samples to be used in SOCs. Further investigation and modelling activity are ongoing. The partially cohesive fracture surface after torsion tests confirmed the very good adhesion and interface strength between the HJ11 glass ceramic sealant and the Crofer22APU, as expected and it was likely due the high wettability of this glass ceramic sealant on the Crofer22APU substrate.

The shear strength was found to decrease with increasing temperature, due to the viscous flow of the residual glassy phase.

The results reported in this MSc thesis are significant considering the following issues and perspectives: in spite of an extensive amount of research, it is still not possible to define the universal or optimal sealing solution, since it depends on the SOC working temperature and stack design. Furthermore, specific investigations are necessary to understand the possible poisoning effect from silica-based sealants on fuel electrode-electrolyte interface, for example. These research findings provide important insights for future sealing development, their characterization and validation in relevant conditions. In particular, different mechanical characterization (such as torsion tests) approaches will be very useful in the view of improving the mechanical strength of glass-ceramic sealants as well to properly balance the crystalline/amorphous phase ratio, in order to limit possible sealant's failure at high temperatures, due to viscous flow of residual glassy phase.

## Bibliography and references

- [1] International Energy Agency - World Energy Outlook, special report: Energy and Air Pollution. 2016.
- [2] British Petroleum - Statistical review of world energy. June 2017.
- [3] British Petroleum - Energy Outlook. 2017 Edition.
- [4] International Energy Agency - CO<sub>2</sub> emissions from fuel combustion. 2017..
- [5] Omar Z. Sharaf, Mehmet F. Orhan - An overview on fuel cell technology: Fundamentals and applications. Renewable and Sustainable Energy Reviews, Volume 32, April 2014, Pages 810-85.
- [6] James Larminie, Andrew Dicks - Fuel cell systems explained, Second edition. January 2003.
- [7] A. Díaz de Arcaya, Asier González González, J A Alzola, Valentin Sanchez - Cooperative Simulation Tool with the Energy Management System for the Storage of Electricity Surplus through Hydrogen. July 2015.
- [8] Pannipha Dokmaingam - Configuration Development of Autothermal Solid Oxide. Engineering Journal, Volume 19 Issue 2, April 2015
- [9] Bora Timurkutluk, Cigdem Timurkutluk, Mahmut D.Mat, Yuksel Kaplan - A review on cell/stack designs for high performance solid oxide fuel cells. Renewable and Sustainable Energy Reviews, Volume 56, April 2016, Pages 1101-1121.
- [10] J. Molenda, K.Swierczek, W. Zajac - Functional materials for the IT-SOFC. Journal of Power Sources, Volume 173, Issue 2, 15 November 2007, Pages 657-670.
- [11] Sossina M. Haile - Fuel cell materials and components. Acta Materialia, Volume 51, Issue 19, 25 November 2003, Pages 5981-6000.
- [12] Neelima Mahato, Amitava Banerjee, Alka Gupta, Shobit Omar, Kantesh Balani - Progress in material selection for solid oxide fuel cell technology. Progress in Materials Science, Volume 72, July 2015, Pages 141-337.
- [13] Belma Talic, Sebastian Molin, Peter Vang Hendriksen, Hilde Lea Lein - Effect of pre-oxidation on the oxidation resistance of Crofer 22 APU. Corrosion Science, Volume 138, 1 July 2018, Pages 189-199.
- [14] Jeffrey W. Fergus - Sealants for solid oxide fuel cells. Journal of Power Sources, Volume 147, Issues 1–2, 9 September 2005, Pages 46-57.
- [15] Steven P. Simner, Jeffrey W. Stevenson - Compressive mica seals for SOFC applications. Journal of Power Sources, Volume 102, Issues 1–2, 1 December 2001, Pages 310-316.
- [16] Yeong-shyung Chou, Jeffrey W. Stevenson and Lawrence A. Chick - Novel Compressive Mica Seals with Metallic Interlayers for Solid Oxide Fuel Cell Applications. Journal of Power Sources, Volume 161, Issue 2, 27 October 2006, Pages 901-906.

- [17] Fellipe Sartori da Silva, Teófilo Miguel de Souza - Novel materials for solid oxide fuel cell technologies: A literature overview. *International Journal of Hydrogen Energy*, Volume 42, Issue 41, 12 October 2017, Pages 26020-26036.
- [18] M.K. Mahapatra, K. Lu - Glass-based seals for solid oxide fuel and electrolyzer cells. *Materials Science and Engineering: R: Reports*, Volume 67, Issues 5–6, 26 February 2010, Pages 65-85.
- [19] M.K. Mahapatra, K. Lu - Seal glass for solid oxide fuel cells. *Journal of Power Sources*, Volume 195, Issue 21, 1 November 2010, Pages 7129-7139.
- [20] Eugen Axinte - Glasses as engineering materials: A review. *Materials & Design*, Volume 32, Issue 4, April 2011, Pages 1717-1732.
- [21] Arun K. Varshneya - *Fundamentals of inorganic glasses*. 2013.
- [22] Sergio Yesid Gómez, Dachamir Hotza - Current developments in reversible solid oxide fuel cells. *Renewable and Sustainable Energy Reviews*, Volume 61, August 2016, Pages 155-174.
- [23] A.G.Sabato, M.Salvo, A.DeMiranda, F.Smeacetto - Crystallization behaviour of glass-ceramic sealant for solid oxide fuel cells. *Materials Letters*, Volume 141, 15 February 2015, Pages 284-287.
- [24] F. Smeacetto, M. Salvo, M. Ferraris, J. Chob, A.R. Boccaccini - Glass–ceramic seal to join Crofer 22 APU alloy to YSZ ceramic in planar SOFCs. *Journal of the European Ceramic Society*, Volume 28, Issue 1, 2008, Pages 61-68.
- [25] Beatriz Cela Greven, Sonja Gross-Barsnick, Thomas Koppitz, Reinhard Conradt, Federico Smeacetto, Andrea Ventrella, Monica Ferraris - Torsional shear strength of novel glass-ceramic composite sealants for solid oxide fuel cell stacks. *International Journal of Applied Ceramic*, 2018.
- [26] F. Smeacetto, A. De Miranda, A. Ventrella, M. Salvo, M. Ferraris - Shear strength tests of glass ceramic sealant for solid oxide fuel cells applications. *Advances in Applied Ceramics*, Volume 114, 2015.
- [27] S. Rodríguez-López, J. Weib, K.C. Laurentic, I. Mathias, V.M. Justoc, F.C. Serbenac, C. Baudina, J. Malzbender, M.J. Pascuala - Mechanical properties of solid oxide fuel cell glass-ceramic sealants in the system BaO/SrO-MgO-B<sub>2</sub>O<sub>3</sub>-SiO<sub>2</sub>. *Journal of the European Ceramic Society*, Volume 37, Issue 11, September 2017, Pages 3579-3594.
- [28] S.T. Mixture, M.O. Naylor, T. Jin, J.E. Shelby - Galliosilicate glasses for viscous sealants in solid oxide fuel cell stacks - Part I: Compositional design. *International Journal of Hydrogen Energy*, Volume 38, Issue 36, 13 December 2013, Pages 16300-16307.
- [29] S.T. Mixture, M.O. Naylor, T. Jin, J.E. Shelby - Galliosilicate glasses for viscous sealants in solid oxide fuel cell stacks - Part II: Interactions with yttria stabilized zirconia and stainless steel coated with alumina. *International Journal of Hydrogen Energy*, Volume 38, Issue 36, 13 December 2013, Pages 16328-16337.
- [30] S.T. Mixture, M.O. Naylor, T. Jin, J.E. Shelby - Galliosilicate glasses for viscous sealants in solid oxide fuel cell stacks - Part III: Behaviour in air and humidified hydrogen. *International Journal of Hydrogen Energy*, Volume 38, Issue 36, 13 December 2013, Pages 16308-16319.